Earth-Abundant Materials for Solar Hydrogen Generation

Thesis by

James Robert McKone

In Partial Fulfillment of the Requirements

for the Degree of

Doctor of Philosophy

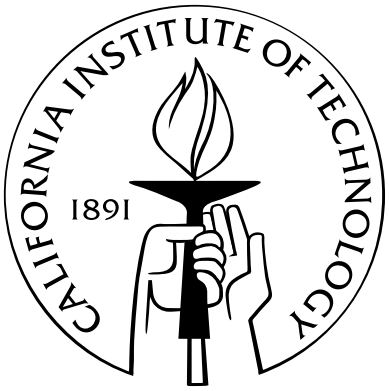

California Institute of Technology

Pasadena, California

2013

(Defended May 23, 2013)

To the many young scientists I had the pleasure of working with these last five years.

Acknowledgments

There are so many people who contributed to my personal and professional experience as a graduate student; anything I write here couldn't possibly do them justice.

Thanks to my advisors, Harry Gray and Nate Lewis. Harry was instrumental in drawing me to Caltech, and I have benefitted from every interaction with him. He is undoubtedly one of the greatest scientists of his age, and he is a consummate research advisor. I expect to strive for the rest of my life to be more like Harry. Nate is the most brilliant mind I have ever encountered, and his passion and tanacity for great science are infectious. Nate has taught me more than anyone how to think like a scientist, and for that I am grateful.

I would also like to thank Bruce Brunschwig, Jay Winkler, Siddharth Dasgupta, and my thesis committee members Jonas Peters, Mitchio Okumura, and Tom Miller. It has been a pleasure to interact with all of these fantastic scientists at various times during my years at Caltech. Each of them freely extended their advice and feedback regarding research, outreach, and career. I aspire to live up to their examples as scientists and members of a research community.

None of the work contained in this dissertation could have been completed without extensive contributions from my close collaborators. Emily Warren and Shannon Boettcher welcomed me into their efforts on hydrogen evolving photocathodes and provided their help, advice, and feedback every step of the way. Matt Shaner, Chris Roske, and Shane Ardo have recently worked with me on semiconductors and catalysts, and they have been wonderful colleagues. Greg Kimball, Jeff Bosco, and Adam Pieterick were all extremely important in the successes we achieved in synthesis and characterization of layered chalcogenides. My thanks also go to our collaborators

at Penn State, Ray Schaak, Eric Popczun, and Matthew Buck. Their partnership allowed me the opportunity to practice teaching about my own research methods as well to as learn from them a range of techniques that were otherwise opaque to me.

It was such a pleasure to work with a number of talented high school and undergraduate students during my time Caltech. I extend my gratitude in particular to Miguel Reyes, Mateo Martinez, Caroline Werlang, and Paul Nuñez, all of whom contributed directly to the primary efforts of my thesis work. Thanks also to all of the undergraduate students in the Lewis and Gray groups as well as the high school students whom I worked with as part of Harry's Solar Army. Their curiosity and excitement about chemistry and science have been tremendously inspiring and motivating to me over the years.

Jim Maiolo, Jillian Dempsey, and Bryan Stubbert were instrumental in getting me started in the Lewis and Gray labs at Caltech and in teaching me some of the most important tools of my graduate work. Additionally, as part of the Lewis and Gray groups I was lucky to interact with a string of amazing postdoctoral researchers, including (in no particular order!) Mike Walter, Nick Strandwitz, Matt Bierman, Bryce Sadtler, Ron Grimm, CX Xiang, Mike Rose, Rob Coridan, Qixi Mi, Wes and Aaron Sattler, James Blakemore, and Jeff Warren. These postdocs were instrumental to my research successes; they challenged me and taught me intellectual maturity in everything from planning experiments to planning a career.

Finally I extend my gratitude to my friends and family. Ethan Van Arnam, Alex Goldberg, Judy Lattimer, Maggie Thompson, Rob Usiskin, Brett Babin, Eric Olmon, and many others have helped me maintain balance in my life in spite of the narrow focus of graduate research. My parents, Marian and Tim McKone, brothers Mark and Mike, sister-in-law Linda, and now my niece Emma, provided support, respite, and much-needed perspective many times. Thanks at last to Kirsten Peterson for her love, patience, and good humor through many high and low points these last few years. I look forward now to where the future will take us.

Abstract

A critical challenge for the 21st century is shifting from the predominant use of fossil fuels to renewables for energy. Among many options, sunlight is the only single renewable resource with sufficient abundance to replace most or all of our current fossil energy use. However, existing photovoltaic and solar thermal technologies cannot be scaled infinitely due to the temporal and geographic intermittency of sunlight. Therefore efficient and inexpensive methods for storage of solar energy in a dense medium are needed in order to greatly increase utilization of the sun as a primary resource. For this purpose we have proposed an artificial photosynthetic system consisting of semiconductors, electrocatalysts, and polymer membranes to carry out photoelectrochemical water splitting as a method for solar fuel generation.

This dissertation describes efforts over the last five years to develop critical semiconductor and catalyst components for efficient and scalable photoelectrochemical hydrogen evolution, one of the half reactions for water splitting. We identified and developed Ni–Mo alloy and Ni_2P nanoparticles as promising earth-abundant electrocatalysts for hydrogen evolution. We thoroughly characterized Ni–Mo alloys alongside Ni and Pt catalysts deposited onto planar and structured Si light absorbers for solar hydrogen generation. We sought to address several key challenges that emerged in the use of non-noble catalysts for solar fuels generation, resulting in the synthesis and characterization of Ni–Mo nanopowder for use in a new photocathode device architecture. To address the mismatch in stability between non-noble metal alloys and Si absorbers, we also synthesized and characterized p-type WSe_2 as a candidate light absorber alternative to Si that is stable under acidic and alkaline conditions.

Contents

Acknowledgments **iv**

Abstract **vi**

List of Figures **ix**

List of Tables **xiv**

1 Introduction **1**

1.1 Purpose and Scope 1

1.2 Background 2

1.2.1 Current Energy Use 2

1.2.2 Why Renewables? 4

1.2.3 Why Solar? 7

1.2.4 Solar Limitations 8

1.2.5 Solar Energy Storage 9

1.2.6 Artificial Photosynthesis 13

1.3 Narrative Summary 15

1.3.1 CCI Solar 15

1.3.2 Chronological Research History 17

2 Earth-Abundant Electrocatalysts **23**

2.1 Introduction and Background 23

2.2 Electrodeposited Ni-based Catalysts 27

2.3 Si-Compatible Ni and Ni–Mo 29

2.4 Catalyst Comparison on Si Substrates 39
2.5 Ni–Mo Nanopowder 43
2.6 Ni_2P Nanoparticles 57

3 Silicon Hydrogen-Evolving Photocathodes 64
3.1 Introduction and Background 64
3.2 Deposition and Characterization 65
3.3 Si Homojunctions 74
3.4 Alternative Design 76

4 Tungsten Diselenide Photocathodes 85
4.1 Introduction and Background 85
4.2 Synthesis 90
4.3 Initial HER Studies 93
4.4 Optimized HER Studies 96
4.5 Further Characterization 101
4.6 Complete Picture of p-WSe_2 108

5 Summary and Conclusions 116

A List of Symbols, Abbreviations, and Their Meanings. 119

B Tutorial on Characterization of HER Electrocatalysts and Photoelectrodes 123
B.1 Hydrogen Evolution Electrocatalysts 123
B.1.1 Theoretical Considerations 123
B.1.2 Experimental Considerations 128
B.2 Hydrogen Evolution Photocathodes 137
B.2.1 Theoretical Considerations 138
B.2.2 Experimental Considerations 141

Bibliography 145

List of Figures

1.1 U.S. energy consumption by source, 1775–2011 3
1.2 Flow diagram for U.S. energy consumption in 2011 5
1.3 Climate change data and models compiled by the Berkeley Earth Surface Temperature program 6
1.4 Global energy demand in 2050 and feasible supply from renewables . . 7
1.5 Data from residental rooftop Si PV array in Northfield, MN 10
1.6 Heat map of insolation intensity in the U.S. 11
1.7 Solar water splitting device schematic 16

2.1 Schematics of key processes involved in PEC hydrogen evolution using Si microwire arrays and heteregeneous catalysts 25
2.2 Volcano plots for HER electrocatalysts under acidic and alkaline conditions 26
2.3 Tafel data for Ni–Mo films electrodeposited from alkaline solutions on glassy carbon and Si surfaces 30
2.4 Cyclic voltammetry for Ni–Mo electrodeposition from sulfamate solution as a function of [Mo] 32
2.5 Electrochemical deposition and stripping data for Ni–Mo films using FTO substrates 34
2.6 Electrochemical HER behavior and photographs of Ni–Mo films electrodeposited with various loadings on FTO substrates 35
2.7 TEM data for electrodeposited sulfamate Ni–Mo films 36
2.8 Time-lapse photographs giving qualitative indication of the stability of electrodeposited sulfamate Ni–Mo films 38

2.9 SEM images for sulfamate Ni and Ni–Mo films electrodeposited onto planar Si substrates 40
2.10 SEM images for sulfamate Ni and Ni–Mo films electrodeposited onto microwire Si substrates 41
2.11 Electrochemical j–E data showing HER catalytic behavior of various catalysts deposited onto planar and microwire Si substrates 42
2.12 Ni–Mo nanopowder synthetic scheme 45
2.13 SEM and TEM data for Ni–Mo nanopowder before and after thermal reduction. 46
2.14 Electrochemical j–E data showing HER catalytic activity of Ni–Mo nanopowders compared to Ni and Ti controls 47
2.15 Stability data for Ni–Mo nanopowders carrying out the HER under acidic and alkaline conditions 48
2.16 Plot illustrating the relationship between composition and activity for Ni–Mo nanopowders 50
2.17 Tafel data for the HER from Ni–Mo nanopowder films as a function of mass loading 51
2.18 CV data for Ni and Ni–Mo nanopowders under alkaline conditions . . 52
2.19 Plot depicting the power law relationship between Ni–Mo nanowder mass loading and cathodic current density at two different overpotentials 53
2.20 Electrochemical HER j–E data and SEM of metallurgical Ni–Mo alloys 56
2.21 Tafel plot for the HER on various chalcogenide nanoparticle films under alkaline conditions 58
2.22 Compiled synthetic data for Ni_2P nanoparticles 59
2.23 Electrochemical j–E data for the HER on Ni_2P particles under acidic and alkaline conditions, compared to Ti and glassy carbon controls . . 60
2.24 Compiled data from Ni_2P annealing and spectroscopy studies 61
2.25 HER stability data for Ni_2P nanoparticle films under acidic conditions 63

3.1 HER j–E data and electron micrographs of planar and microwire Si n^+p-junction photoelectrodes coated with thin Pt films 66
3.2 Electrodeposition j–E data for sulfamate Ni–Mo films on planar p^+ and n^+p-junction Si photoelectrodes 67
3.3 PEC hydrogen evolution j–E data for planar and microwire p-Si photoelectrodes deposited with optimized Ni, Ni–Mo, and Pt films 70
3.4 Compiled j–E data for hydrogen evolution from Pt films deposited on various types of Si electrodes 72
3.5 X-ray photoelectron spectra of p^+-Si samples deposited with Pt by evaporation and electroless deposition, compared to a Pt-free control 73
3.6 PEC hydrogen evolution j–E data for p-Si and n^+p-Si microwire arrays deposited with Pt and Ni–Mo under optimized conditions 75
3.7 PEC hydrogen evolution j–E data for two illuminated p-Si electrodes illustrating of the tradeoff between catalyst activity and photocurrent . 76
3.8 Schematic illustrations of two different modes of catalyst deposition onto Si microwires 77
3.9 Schematic representation of a hydrogen evolving photocathode with the "MEA" device architecture 78
3.10 Scanning electron micrographs of a microwire array deposited with layers of Ni–Mo and TiO_2 nanoparticles at the base using a centrifugation method 79
3.11 HER j–E data for metallized Si microwire and planar Ti substrates deposited with Ni–Mo and/or TiO_2 using centrifuge flocculation under identical conditions 80
3.12 PEC hydrogen evolution j–E data for a planar Si n^+p-junction photoelectrode deposited with layers of Ni–Mo and TiO_2 81
3.13 Scanning electron micrograph and PEC hydrogen evolution j–E data and for a Si microwire n^+p junction photoelectrode deposited with the Ni–Mo and TiO_2 in the MEA architecture 82
3.14 PEC hydrogen evolution j–E data for improved MEA-type Si microwire photocathodes deposited with Pt and Ni–Mo catalysts 83

4.1 Crystal structure and MO diagram for the Mo and W layered chalcogenides 87
4.2 Scanning electron micrograph of an as-grown WS_2 crystal 88
4.3 Reaction scheme for MX_2 crystal growth by CVT 91
4.4 Photograph of a large WSe_2 crystallite grown by CVT 93
4.5 Electrochemical j–E data illustrating the low catalytic activity of pristine p-WSe_2 toward the HER in the dark and under illumination . . . 95
4.6 Initial PEC hydrogen evolution j–E behavior of p-WSe_2/Pt photoelectrodes in mildly acidic and strongly alkaline solutions 96
4.7 PEC j–E data for deposition of Pt and Ru catalysts onto the surfaces of p$-WSe_2$ photoelectrodes 98
4.8 Scanning electron micrograph of a p-WSe_2 electrode after Pt deposition and PEC HER testing 99
4.9 PEC hydrogen evolution j–E data for illuminated p-WSe_2 photoelectrodes deposited with the noted catalysts using optimized methods . . 99
4.10 Comparison of PEC HER results for a single p-WSe_2/Pt photoelectrode in two different electrolytes 100
4.11 Potentiostatic i–t data for a p-WSe_2 photoelectrode in MV^{2+} solution at two different pH values 102
4.12 Optical micrographs of p-WSe_2 photoelectrodes before, between, and after stability tests 103
4.13 Spectral response data for a representative p-WSe_2 photoelectrode in aqueous MV^{2+} solution 104
4.14 Detail of the spectral response data for p-WSe_2 at the photocurrent onset overlaid with data predicted from the Gärtner carrier diffusion model 106
4.15 PEC hydrogen evolution j–E data for a representative p-WSe_2 crystal under illumination in $Ru(NH_3)_6^{3+/2+}$ solution 107
4.16 Mott-Schottky data and optical micrographs for p-WSe_2 photoelectrodes with pristine and highly stepped surfaces 109

4.17 Flatband potentials calculated for a set of 9 p-WSe_2 photoelectrodes from Mott-Schottky measurements in $Fe(CN)_6^{3-/4-}$ solution 110
4.18 Schematic depiction of the pH-dependence of the band edge positions for a hypothetical, canonical semiconductor and for WSe_2 electrodes with pristine surfaces 111
4.19 Comparison of the expected photocurrents for p-WSe_2 using the ELH-type tungsten-halogen bulb spectrum compared to the standard AM1.5G spectrum 114
4.20 Scanning electron micrograph of the powder that results from heating together tungsten metal, Na_2S, and pure S under inert gas 115

5.1 World record energy conversion efficiency vs. time for the various commercial and several heavily researched solar photovoltaic technologies. . 118

B.1 Cyclic voltammograms of glassy carbon electrodes deposited with polytungstate using Pt and carbon counter electrodes 130
B.2 Electrochemical j–E data for clean Pt electrodes near E_{RHE} in 0.5 M H_2SO_4 solutions that have and have not been saturated with H_2(g) . . 135
B.3 Model of a high performing Si/Pt hydrogen evolving photocathode under 100 mW cm^{-2} solar illumination 139

List of Tables

1.1 Materials and energy storage efficiencies of selected artificial photosynthetic devices 14

2.1 Compositions of two alkaline Ni–Mo deposition solutions from prior literature reports of high HER activity 29

2.2 Compositions of two new Ni–Mo deposition solutions with mildly acidic pH values. 33

4.1 Optoelectronic properties for MX_2 compounds 86

4.2 Compiled figures of merit from previous examples of efficient MX_2 photoelectrodes in contact with aqueous redox couples 89

4.3 Compiled figures of merit for PEC hydrogen evolution on p-WSe_2 photoelectrodes 101

Chapter 1

Introduction

1.1 Purpose and Scope

This dissertation describes in detail the whole of my research efforts from the Fall of 2008 through the present date (May of 2013). It has been written in part to satisfy the requirements for a doctoral degree in chemistry from Caltech. I also hope that it will be useful as a resource for scientists who are interested in solar hydrogen generation, or for researchers that would like to replicate or expand on my work. With these audiences in mind, I have divided the content into chapters addressing various topics.

The remainder of Chapter 1 is a general overview and introductoin to the field of artificial photosythesis as I have come to understand it through my involvement with the Gray and Lewis groups. Following this overview, I have included a brief narrative summary of how I came to work on the topic of photoelectrochemical (PEC) hydrogen evolution and a brief chronology of my research efforts.

Chapters 2–4 are the main body of the dissertation, covering experimental work and major results. Chapter 2 describes development of earth-abundant Ni–Mo and Ni_2P electrocatalysts for the hydrogen evolution reaction (HER). Chapter 3 details efforts on coupling various catalysts to silicon light absorbers. Chapter 4 covers work on synthesizing and characterizing p-WSe_2 as a photocathode light absorber.

Chapters 2–4 eschew explicit description of experimental protocols in favor of emphasis on data and interpretation. However, the text and figure captions include sufficient experimental details so that someone "familiar in the art" should be able to

reproduce the results. The reader is encouraged to consult the associated publications for more detailed experimental information.

This dissertation concludes with a brief summary as well as some conclusions and general recommendations for future efforts toward solar hydrogen generation and artificial photosynthesis. I have also included two appendices. Appendix A1 contains a list of symbols and abbreviations used herein with their associated definitions. Appendix A2 is a brief tutorial on best practices for carrying out electrochemistry and photoelectrochemistry measurements in characterizing hydrogen evolving cathodes and photocathodes, respectively. This tutorial discusses several subtle features and pitfalls of these measurements that I found were not immediately obvious from the published literature. I have also included references to what I believe to be the best current resources for detailed treatments of the relevant theory for electrochemistry and solid-state physics.

I hope that this dissertation will serve some useful purpose other than facilitating receipt of a doctoral degree. The main text, along with the Appendix B and the associated references, should be sufficient to allow anyone with a strong background in chemistry to repeat and expand on my work. If nothing else, perhaps some decades down the road a young researcher will come across this document and marvel at how quaint was our understanding of photoelectrochemistry and electrocatalysis back then. In any case, please enjoy!

1.2 Background

1.2.1 Current Energy Use

The global economy uses massive quantities of energy to support every aspect of human life and productivity. Energy sources worldwide range from direct combustion of fuels to harnessing various alternative sources of energy for heat or electricity. Some sources of energy, such wind and certain biofuels, are renewable in the sense that the available stores are functionally inexhaustible, or they can be replenished at the same

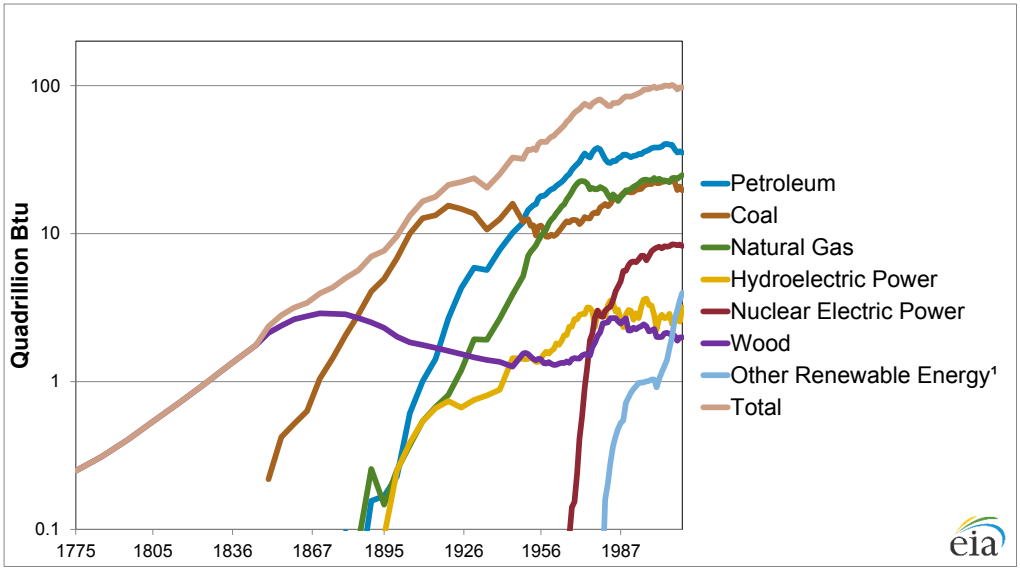

Figure 1.1. Plot of U.S. total energy consumption by source from 1775 to 2011. Data from the U.S. Energy Information Administration's 2012 Annual Energy Review.[1]

rate as they are consumed. Other energy sources, such as fissile material and fossil fuels, are not renewable since they are not replenished on a timescale comparable to their utilization.

During the last century, human use of energy has grown at an exponential rate. Over the same time period, the mixture of primary sources of energy that humans use has changed significantly, as shown in Figure 1.1. As little at 150 years ago humans relied almost exclusively on burning plant-based carbon sources. Beginning around the turn of the 20th century, however, extraction and combustion of fossil fuels have made up the bulk of human energy use. This rapid expansion in fossil fuel use has had significant ramifications for geopolitics, economics, and the environment, to name a few.

The United States used on the order of 103×10^{18} J of energy in 2011.[1] Researchers at Lawrence Livermore National Lab have generated a series of detailed energy flow diagrams intended to express the sources and destinations of all the energy used in the U.S.; one such diagram is depicted in Figure 1.2.[2] These data illustrate clearly that the vast majority of U.S. energy consumption comes from non-renewable fossil

sources, and also that over half of all the energy currently recovered is "rejected" (i.e., wasted).

1.2.2 Why Renewables?

Today there exists a broad and strong consensus in the global scientific and political communities that humans must transition away from intensive utilization of carbon-based fossil fuels and toward renewable sources of energy. Nate Lewis has collected a large body of data to highlight the imperatives and material requirements for such a shift to renewables. The remainder of this introduction is based in large part on his writings and presentations on the subject.[3,4]

One concern over continued use of fossil fuels is their inherently finite nature. Academic and industry representatives have anticipated the arrival of "peak oil," wherein the supply of fossil fuels reaches a maximum and then gradually transitions from a functionally infinite to a highly precious resource, for some time.[5] This transition is predicted to result in a consistent increase in the price of fossil fuels into the foreseeable future. Nevertheless, allowing for an eventual peak in world fossil fuel recovery and consumption, conservative estimates suggest that reserves sufficient for hundreds of years at current usage rates are already accessible.[3]

Another concern for the continued use of fossil fuels involves human health and welfare. Burning fossil fuels produces large quantities of pollutants, including nitrogen and sulfur oxides, particulates, and volatilized heavy metals. These compounds are inevitable byproducts because the fuels themselves consist of fossilized animal and plant matter that have been massively concentrated over geological timescales. Burning fossil fuels therefore releases these concentrated deposits over a comparatively short time period, resulting in local atmospheric concentrations of, e.g., volatile mercury species, for which living species like humans are not adapted.

Climate change is another significant concern for the continued use of fossil fuels. The release of carbon dioxide as well as light hydrocarbon gases (methane, ethane, etc.) is understood to contribute significantly to the increase in global average tem-

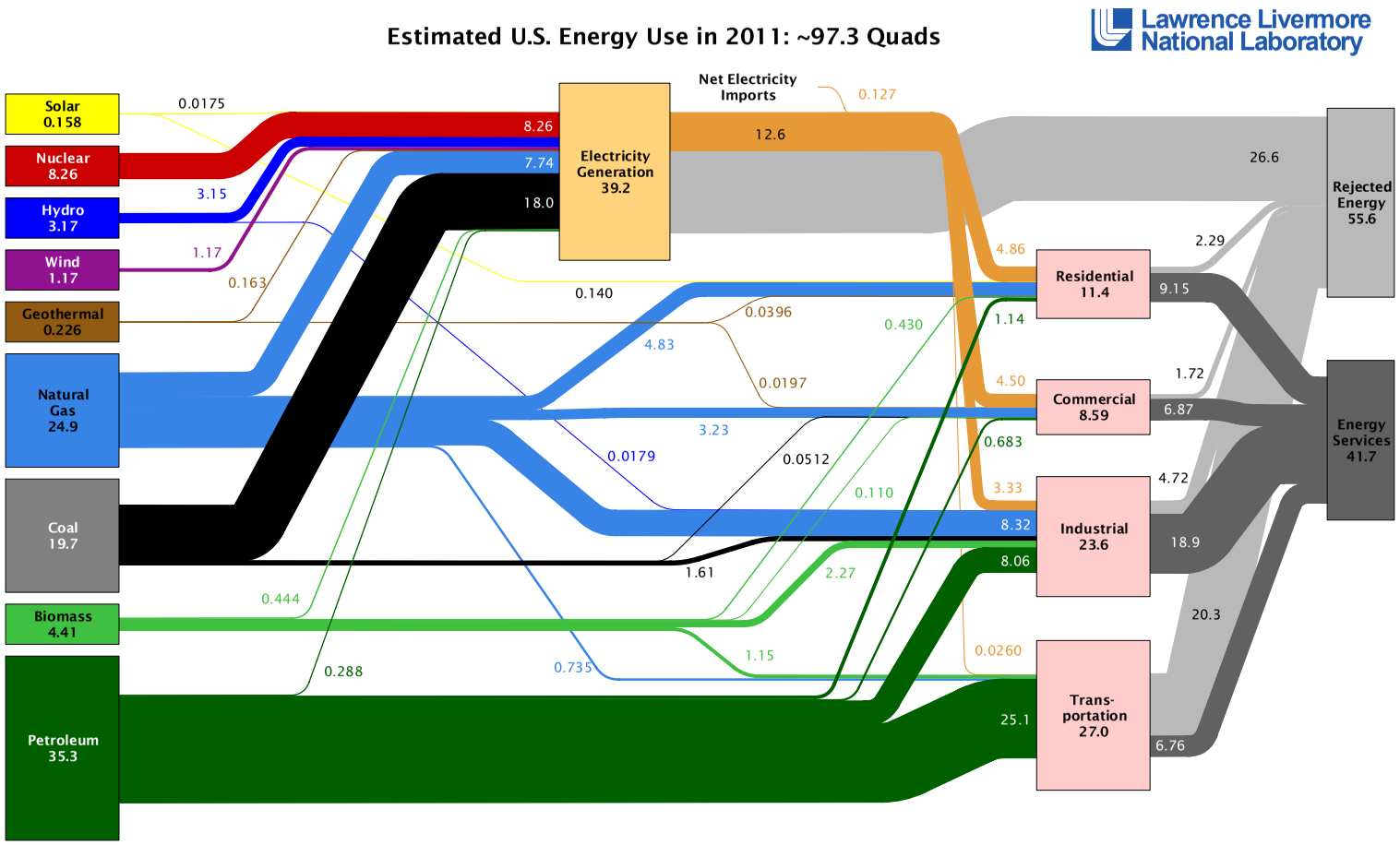

Figure 1.2. Energy flow diagram depicting the source and fate of all energy used in the U.S. in 2011. Publically available from Lawrence Livermore National Lab.[2]

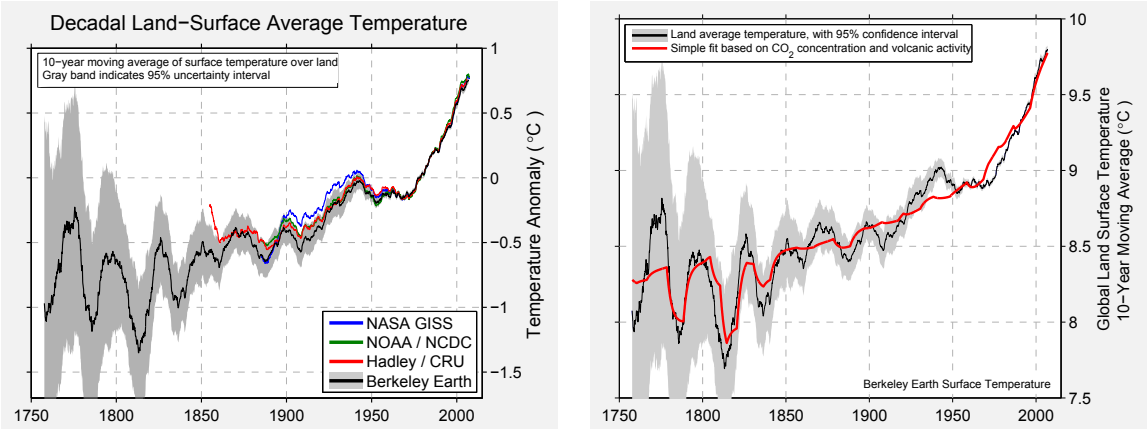

Figure 1.3. Left: data depicting the clear recent upward trend in global average temperatue from several independent studies. Right: Temperature data from the Berkeley Earth Surface Temperature (BEST) study overlaid with a simple model based on CO_2 concentration and volcanic activity. Publically available from the BEST report.[6]

perature through the greenhouse effect. An illustration of the correlation of increased atmospheric CO_2 content with global average temperatures is shown in Figure 1.3. Although this topic is culturally controversial in the United States, the global scientific community (and to a large extent the broader cultural community) has reached a strong consensus that the threat of climate change and the connection between fossil fuel use and the greenhouse effect are significant enough to justify massive efforts to move away from such energy resources in the coming years.

A final concern for continued use of fossil fuels involves energy security. Major oil, coal, and gas deposits are located in relatively small geographic regions. Many of these regions are also politically unstable, or hostile toward countries making up the majority of the developed economies (i.e., the major fossil energy consumers). Major figures in the United States and elsewhere have thus expressed the desirability of achieving "energy independence," wherein the large majority of energy resources are produced or recovered locally. For North America, a significant amount of energy independence could perhaps be obtained in the near term by continued development of shale gas and tar sands deposits in the Northern U.S. and Canada. However, the finite and unproven nature of these new fossil resources suggests that their availability may be slow to develop and/or short-lived.

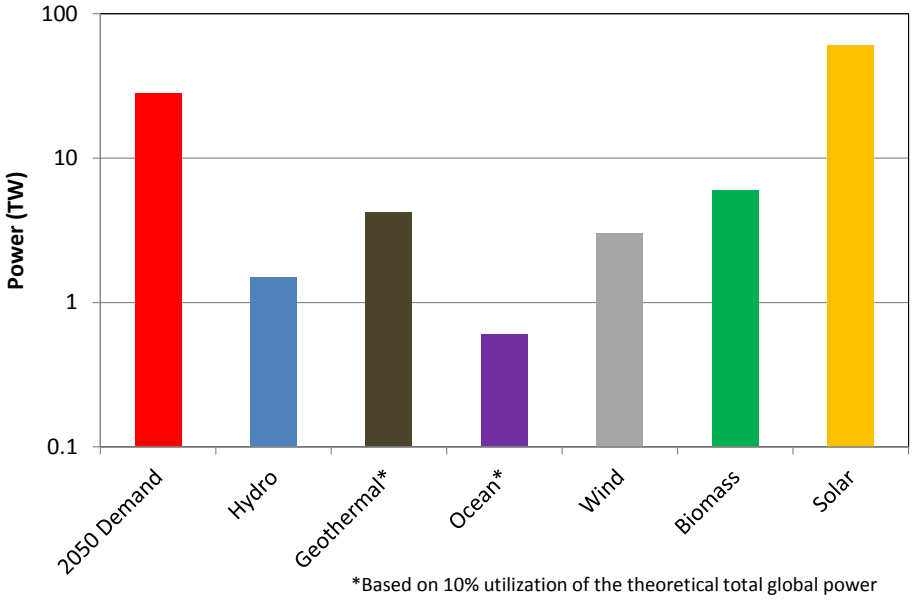

Figure 1.4. Chart of the expected global power demand in 2050 along with estimates of the feasible supply from various non-fossil resources. Data collected from calculations by Nate Lewis.[3]

1.2.3 Why Solar?

Figure 1.4 depicts (on a log scale) the anticipated global energy demand in 2050 along with estimates of the energy that could be feasibly extracted from various major renewable energy sources.[3] Although each renewable resource could be used to offset a significant proportion of the energy demand, solar energy is the only one where the recoverable fraction is larger than the total demand. This is perhaps unsurprising, as all renewable energy sources rely fundamentally on the sun through electromagnetic radiation or gravitational effects. Solar energy is also arguably the most underutilized renewable resource, especially relative to its enormous potential. This underutilization is largely due to the high cost of manufacturing photovoltaic (PV) and solar thermal technologies exacerbated by the relatively low energy density in sunlight striking a given area ($\sim$1 kW m^{-2} around noon on a sunny day in North America).

Due to the significant promise of increased use of solar energy, huge efforts have been recently undertaken to develop solar energy conversion technologies that are

inexpensive to produce and to install. The average installed cost for PV arrays continues to decline at a rate that, if continued, will lead to direct cost-competitiveness with conventional fossil fuels within the next 1–2 decades in the United States.[7] The U.S. Department of Energy has recently funded a broad effort called the SunShot program intended to facilitate technological innovations that will enable photovoltaic arrays to reach installed costs of <$1 per watt.[8]

Continued PV research and industrial innovations leading to decreases in cost in the coming years are highly likely. Simply increasing the scale of production for crystalline Si and thin-film technologies will eventually result in manufacturing efficiencies, diminishing hardware and installation costs significantly. Also, continued basic technological innovations on the design and construction of photovoltaic cells and modules will result in decreased costs per watt for manufactured systems. Some of these innovations can be quite significant, such as the recent (as of this writing) record efficiencies for CdTe solar cells.[9]

Other unforseen "step-change" innovations in developing cost-competitive solar are also quite likely, as unconventional photovoltaic technologies are constantly being improved in laboratories and pilot-scale manufacturing facilities. For example, Alta Devices recently demonstrated ultrathin crystalline GaAs solar cells that approach the efficiency limit of ∼30% obtainable for this material.[9,10] Modules are currently being manufactured and marketed to the consumer electronics and military markets, as the high obtainable efficiencies and good low-light performance makes these cells useful for charging personal electronics and powering remote military installations.

1.2.4 Solar Limitations

The outlook for a massive, market-driven transition from fossil fuels to photovoltaic technologies for electricity generation in the coming decades is highly favorable. However, conventional PV technologies suffer from significant drawbacks that limit their maximum feasible utilization. The first major drawback of photovoltaic technologies is that they can only generate electricity. As shown previously in Figure 1.2,

only ∼40% of total energy usage in the U.S. is in the form of electricity. The remainder comes largely from direct combustion of carbon-based fuels in the industrial and transportation sectors. Some proportion of this current fuels use could likely be transitioned to electricity, especially in transportation with the continued adoption of battery and hybrid technologies, but a complete transition to solar-driven electrical energy usage is impractical.

A more important barrier to ubiquitous adoption of photovoltaics is the fact that the solar resource is intermittent. The energy flux of sunlight striking any part of the Earth varies significantly on the timescale of minutes (e.g., due to clouds), hours (due to solar angle), days (due to weather patterns), and months (due to seasons). This variability is illustrated in Figure 1.5, which depicts the daily, weekly, and yearly output of a residential rooftop solar array located in Northfield, MN. Furthermore, as with fossil energy some geographic locations receive significantly more solar energy than others, which is illustrated in the map in Figure 1.6.[11]

Due to the temporal and spatial intermittency of sunlight, photovoltaics simply cannot be relied upon to provide a significant offset to fossil fuel resources in the absence of massive changes to the electrical grid. One solution to this problem involves only developing such technologies to the limit at which their usage does not disrupt the otherwise continuous supply of energy from conventional, continuous sources. Researchers have estimated that this limit lies around 20%,[12–14] which already represents a 40-fold increase compared to current solar PV supply.[1] Thus the current markets for photovoltaics and solar-thermal electriciy will continue expanding at a significant rate in the coming years as production prices decrease. However, current solar capture methods cannot replace conventional power supplies to the extent required to ameliorate problems such as pollution, climate change, and energy security.

1.2.5 Solar Energy Storage

A promising method for mitigating the problem of solar intermittency involves the use of large-scale energy storage technologies.[3,15] The ideal solar energy storage method

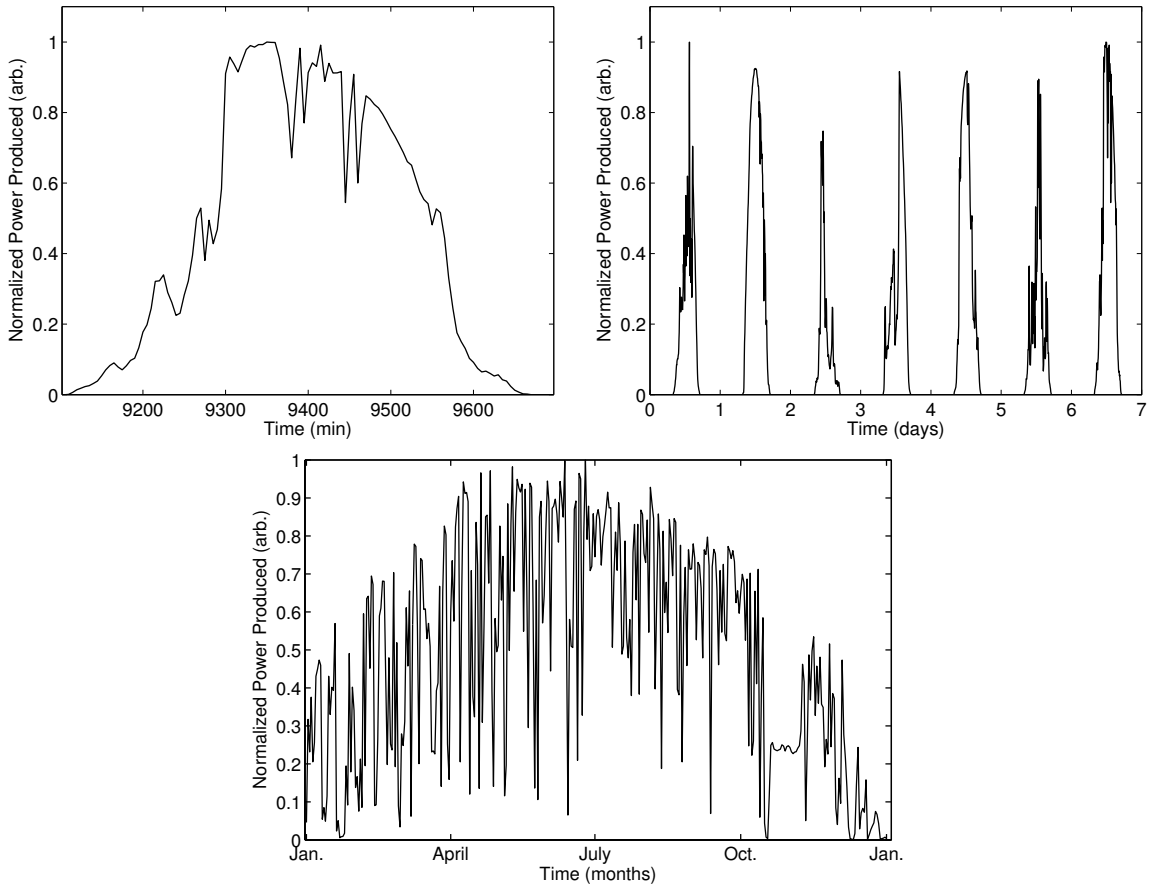

Figure 1.5. Normalized power vs. time plots showing the power produced by a residental rooftop crystalline Si solar array in Northfield, MN over the course of one day (upper left), one week (upper right), and one year (below). The power output exhibits systematic variability on each timescale due to day/night cycles, weather patterns, and seasonal variability. Data courtesy Timothy and Marian McKone; used with permission.

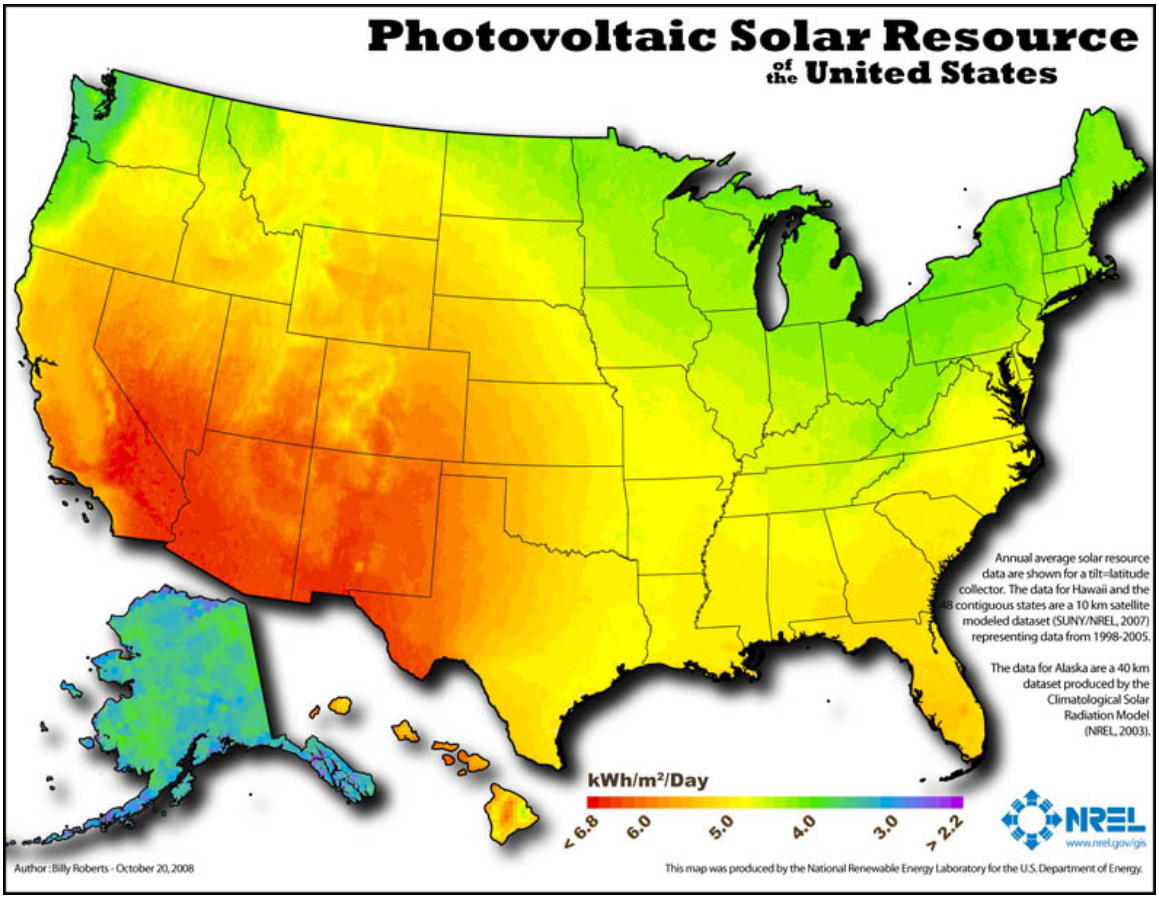

Figure 1.6. Heat map depicting the daily average energy content of the solar flux striking the U.S. Produced by the U.S. National Renewable Energy Laboratory using data collected from 1998 to 2005.[?]

would allow for efficiently capturing photons and then converting their energy into an inexpensive, dense medium that can be transported and the stored energy recovered on demand. The ultimate realization of fully scaled solar energy storage would, in principle, allow solar energy to approach 100% of global electricity usage.[14,16] Also the ideal solar storage scheme could offset a large proportion of current direct fossil energy usage, as the stored energy could be transported and used in a very similar fashion to hydrocarbons.

Already some solar storage methods are developed and demonstrated.[15] For example, one solar-thermal storage method involves using an array of mirrors to heat a large quantity of a dense material with high heat capacity such as molten salts. These molten salts remain at elevated temperature for hours, and can thus be used to drive turbines at night. However, like all solar thermal technologies, this approach suffers from restrictive land requirements and involves extensive and highly technical planning and engineering.

Another straightforward method of solar energy storage involves using photovoltaic arrays to drive the charging cycle of existing or next-generation battery technologies. Such "solar battery" schemes could be developed to fit any scale. As previously noted, small photovoltaic modules are available that can be used to directly charge portable electronics devices. Larger arrays of batteries for transportation or residential usage could be installed in homes and businesses and charged using rooftop photovoltaic arrays. Still larger battery banks could be permanently installed adjacent to industrial or business parks and charged from grid-connected photovoltaic arrays as needed in order to provide electrical energy on demand for these sectors. Indeed, large battery banks could be connected into the existing electricity grid and used to buffer and smooth the supply of all intermittent power sources. Unfortunately, battery technologies are not yet inexpensive, safe, or energy-dense enough to allow for development of very large scale storage.[17] Current research efforts to develop novel battery technologies, such as redox flow and Li– or Na–air batteries, may allow such large-scale storage methods to become a reality.

1.2.6 Artificial Photosynthesis

Yet a third method of solar energy storage is called "artificial photosynthesis," and it is the subject of this dissertation. Artificial photosynthesis lies intermediate between photovoltaic technologies and natural photosynthetic processes. In artificial photosynthesis, as in photovoltaics, solar photons are incident on human-made light absorbers, resulting in electronic excited states. Then, as in photosynthesis, those excited states are immediately used to drive thermodynamically uphill chemical reactions, thereby converting electrical energy to stored chemical energy. Ideally these chemical reactions would produce fuel compounds that closely resemble the refined hydrocarbons currently used in the transportation and industrial sectors.

Artificial photosynthesis is quite similar to solar battery storage, except that the fuel species are generally lighter and more reactive, and therefore more energy dense, than those currently used for electricity storage in batteries. Also, the use of artificial photosynthesis to generate fuels could allow for continued usage of the existing fossil fuel infrastructure, which would decrease the capital costs of incorporating solar technologies across all energy sectors. Hydrogen has a particularly high gravimmetric energy density, and can be obtained directly by electrolysis of water. But hydrogen suffers from a relatively low volumetric density due to its extremely low boiling point, making storage and transportation difficult. Nevertheless, water electrolysis to yield hydrogen (and oxygen as a byproduct) has been thoroughly studied and serves as a useful approach for demonstrating the possibility of artificial photosynthesis.

The critical challenge of artificial photosynthesis is that it simply has not yet been demonstrated in an efficient, robust, and commercially viable form. Several functioning fuel-forming systems based on photoelectrochemical (PEC) water splitting to hydrogen and oxygen, summarized in Table 1.1, have been demonstrated in the laboratory, but none of these exhibited all of the required qualities for commercial success. Thus the best current route to solar energy storage in fuels would involve coupling commercial photovoltaic arrays with commercial water electrolyzers to generate hydrogen fuel for combustion or fuel cells. Even this coupled approach is

Table 1.1. Materials and energy storage efficiencies of selected artificial photosynthetic devices

light absorber(s)	catalyst(s)	redox products	reported η (%)	reference
InP/GaAs	Pt, MnO_2	H_2/O_2	8.2	Kainthla [18]
$GaInP_2$/GaAs	Pt	H_2/O_2	12.4	Khaselev [19]
AlGaAs/Si	Pt/RuO_2	H_2/O_2	18	Licht [20]
GaInP/GaAs	Pt	H_2/O_2	16.5	Khaselev [21]
Si	Co–Mo/$NiFeO_x$	H_2/O_2	7.8	Rocheleau [22]
Si	Ni–Mo–Zn/CoO_x	H_2/O_2	4.7	Reece [23]
WSe_2/InP	Pt	H_2/Br_2	7.8	Levy-Clement [24]
Si	Pt	H_2/Br_2	8.6	Luttmer [25]

not commercially viable, as neither photovoltaic nor electrolysis technologies are the cost-leaders in terms of supply of electricity or hydrogen, respectively.

Artificial photosynthesis is a nascent technology that still requires significant fundamental scientific discoveries and innovations. As a result, current research on artificial photosynthesis is carried out in academic laboratories. More specfically, much of the recent academic work on solar water splitting has focused around developing new light absorber and catalyst materials that will be cheaper to produce than current-generation PV and electrolysis apparatus. In pursuit of these low cost, scalable, options, researchers have restricted themselves to using only so-called "earth-abundant" elements, such as the first row transition metals, oxygen, carbon, sulfur, etc.

This dissertation discusses in detail our work over the last 5 years to develop several enabling innovations for artificial photosynthesis via solar water splitting. Herein I discuss efforts to generate non-noble catalysts for the hydrogen evolution reaction that can be combined with silicon light absorbers to generate hydrogen under solar illumination. I also discuss in some detail our attempts to mitigate two problematic behaviors arising from incorporation of these non-noble catalysts with Si light absorbers: deleterious light absorption by the catalyst layer and the stability mismatch between Si and earth-abundant transition metal composites.

1.3 Narrative Summary

1.3.1 CCI Solar

Most of the work contained in this dissertation on photoelectrochemical hydrogen evolution was carried out with support from the NSF-funded Center for Chemical Innovation (CCI Solar) subtitled "Powering the Planet."[26] The second phase of the CCI was funded from 2008 to 2013 at an unprecedented level for the field, and our research efforts have involved a large network of scientists working together to realize fundamental innovations required for demonstrating unassisted solar water splitting.

The CCI Solar project coalesced around a proposed composition and architecture for a device that could split water into hydrogen and oxygen using energy input only from sunlight. The design was originally conceived by Nate Lewis and his research group at an annual research retreat. It was adapted into a visual schematic, shown in Figure 1.7, by Elizabeth Santori, a Lewis Group graduate student. It subsequently became the de facto logo for the CCI Solar program.

The CCI Solar device architecture consisted of a set of two semiconductor materials with high aspect-ratio (e.g., rod or wire) geometries, each bound into opposite sides of a membrane. The device would be oriented with the long axis of the wires parallel to the solar illumination vector, such that sunlight would first strike the top layer, then traverse the membrane, and finally strike the bottom layer. The top layer would be constructed of a stable, robust metal oxide material capable of absorbing blue photons and generating oxygen from neutral or acidic water. The bottom layer would be constructed of another stable, robust semiconductor capable of generating hydrogen from protons (or a protonated Brønsted base). The initial material targets for the photoanode and photocathode were WO_3 and Si, respectively. These materials were chosen for their earth-abundant composition, acid stability, and well-precedented use in photoelectrochemistry.

The central membrane layer of the CCI device was to serve three functions: first as an electrical connection between the anode and cathode; second as a physical support for both absorber layers; and third to allow for neutralization of the pH gradient

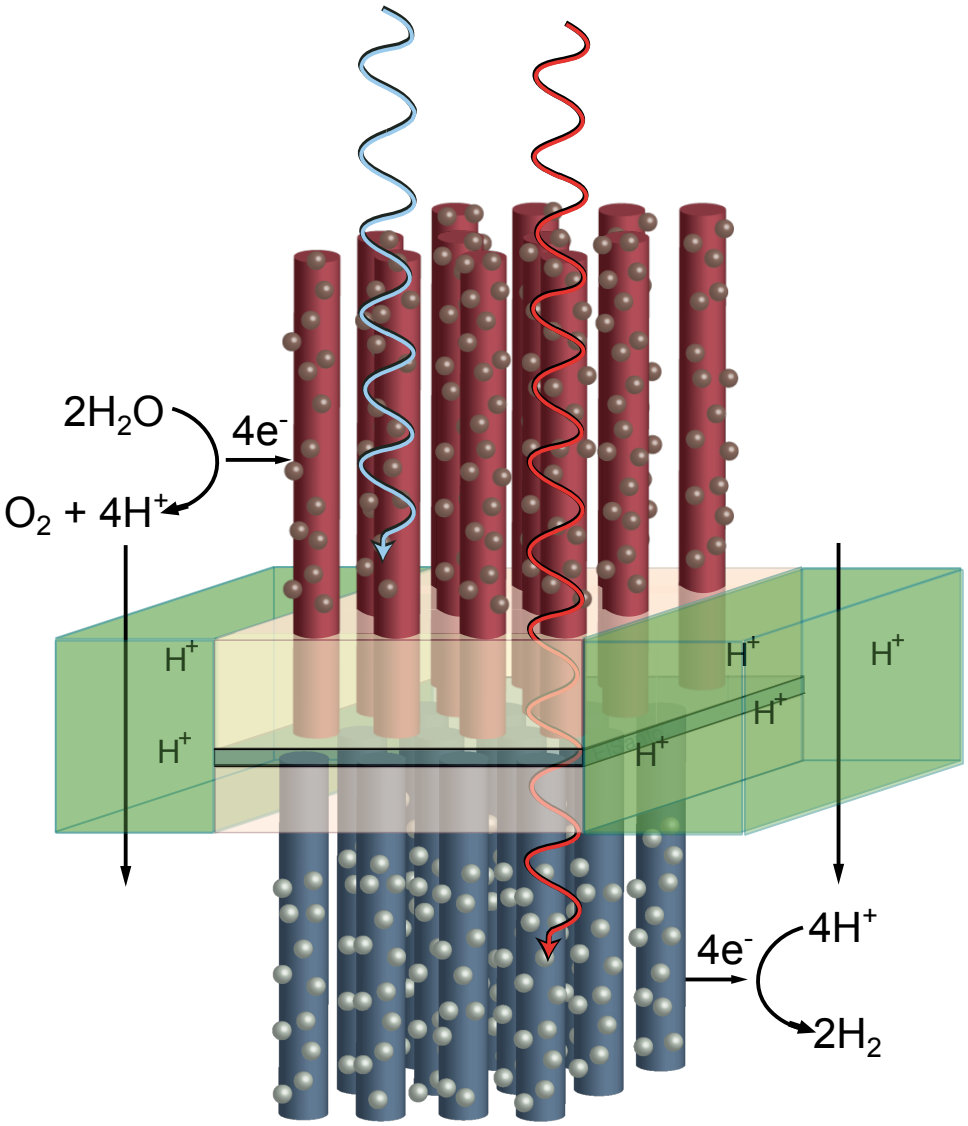

Figure 1.7. Schematic depiction of a solar water splitting device based on two parallel arrays of light absorbers with associated catalysts, linked together by a central membrane. Copyright 2013, Elizabeth A. Santori;[27] used with permission.

that would develop between the anode and cathode. We proposed to use for the membrane layer mixtures of various polymeric materials that could be combined to give the desired properties. For example, we expected that composites Nafion® with a conductive polymer would endow the membrane with mixed ionic and electrical conductivity.

The final relevant components for the CCI device were electrocatalysts for the oxygen evolution reaction (OER) and hydrogen evolution reaction (HER), respectively. These catalysts were to be either molecules or materials physically attached to the semiconductor surfaces in order to enable efficient generation of oxygen and hydrogen. It was not clear (and indeed is still not clear) whether or not an oxygen evolution catalyst would be required for the photoanode, as most metal oxides exhibit reasonable catalytic activity toward the OER. However, we expected that a hydrogen evolution catalyst would be required for the photocathode, as essentially all small-bandgap semiconductors exhibit low activity toward the HER. Although noble metals such as Pt, Ir, and Ru are known to be efficient electrocatalysts for the HER and OER, we targeted development of catalysts incorporating more abundant elements such as Ni, Co, or Fe.

1.3.2 Chronological Research History

I arrived at Caltech during the summer of 2008, which was an active period for work on solar fuels at Caltech and elsewhere. The Nocera group had just published the first of what would be an extensive series of papers on an electrodeposited cobalt oxide water oxidation catalyst that operated in neutral water.[28] This result implied the possibility of net water splitting using earth-abundant catalyst materials and mild conditions.

At the same time, Gray group graduate student Jillian Dempsey and postdoc Bryan Stubbert were leading an effort to synthesize and characterize the activities and operative mechanisms of a set of molecular, cobalt-based hydrogen evolution catalysts.[29,30] The cobalt glyoxime systems, first studied by Espenson and later re-

visited by Xile Hu at Caltech,[31,32] were particularly promising candidates as they exhibit high electrocatalytic rate constants at rather low overpotentials. These catalysts were proposed to be attached directly to the surface of Si photoelectrodes using functionalization strategies under development by the Lewis group.[33] Additionally, mechanistic studies of these molecular systems were anticipated to lead to rational design of newer and better molecular catalysts.[34]

Meanwhile the Lewis group was developing Si and WO_3 light absorber materials to serve as watter splitting photocathodes and photoanodes, respectively. Graduate students Jim Maiolo, Josh Spurgeon, Emily Warren, and postdoc Shannon Boettcher were making a concerted effort with collaborators in the Atwater research group to demonstrate the viability of high aspect-ratio Si microwire arrays for solar energy conversion.[35–45] Additionally, graduate student Craig Wiggenhorn and postdoc Karla Reyes-Gil were generating nanostructured WO_3 to show that increased structure would result in improved light absorption and excited charge carrier collection for the OER.

After committing to work as a collaborative student between the Gray and Lewis groups, I spoke at some length with Harry and Nate about research directions. We decided that although molecular catalysts were promising candidates for understanding mechanistic details of hydrogen evolution, it would also be valuable to discover and develop earth-abundant (generously defined as higher in elemental abundance than the Pt-group metals), heterogeneous hydrogen evolution catalysts that might be able to complement the recent work on cobalt oxide and other systems for water oxidation. Additionally, the details and limitations of directly attaching non-noble heterogeneous catalysts to Si surfaces had not been previously explored. Thus I took on the task of identifying and developing non-noble hydrogen evolution catalysts in combination with p-type Si photocathodes, which led to the work discussed in this dissertation.

My initial efforts were carried out in close collaboration with a graduate student, Emily Warren, and a postdoctoral researcher, Shannon Boettcher. We worked to characterize the hydrogen evolution behavior of various types of Si photoelectrodes

with noble metal HER catalysts. We constructed and tested Si devices using commercial planar substrates as well as Si microwire arrays synthesized in house. Results from characterization of planar and microwire arrays of p-Si as well as n^+p-Si homojunctions with Pt HER catalysts were published in the *Journal of the American Chemical Society* in 2011.[46] This work primarily served to benchmark the expected performance of commercial Si photovoltaic materials for photoelectrochemical hydrogen evolution, as well as to prove the quality of Si microwire arrays. Since the details of Si microwire array growth and characterization were not the main emphasis of my research, this dissertation only discusses microwire properties to the extent required to understand observed catalyst and Si-catalyst interactions.

Alongside our collaborative effort to characterize Si hydrogen evolving photoelectrodes, I sought initially to develop a polytungstate HER catalyst that had been previously reported to exhibit very high activity toward hydrogen evolution in acidic solution.[47] Unfortunately, after some effort and consultation with Nate and postdoc Qixi Mi I concluded that the observed high catalytic activity of the deposited materials was due to deposition of contaminants from the Pt counter electrode. The possibility of Pt contamination from the nearly ubiquitous Pt counter electrode is indeed a common pitfall in HER materials study; thus it is treated briefly in Appendix B.

In the midst of efforts to understand the behavior of tungstates for the HER, I worked with a number of Lewis Group colleagues to compile a detailed review on solar water splitting for *Chemistry Reviews*.[48] I was broadly responsible for the component of that review on hydrogen evolution electrocatalysis. In the course of surveying the previous literature, it became clear that catalyst materials based on mixtures of Ni and Mo, often with other components, were already heavily studied and had exhibited the highest HER activity of any non-noble system to date. We undertook efforts to reproduce previous work on Ni–Mo alloys in hopes of combining them with p-Si light absorbers for efficient photoelectrochemical hydrogen evolution. Several months were spent developing methods for electrodeposition of Ni–Mo alloys that were compatible with Si photoelectrodes. The electrodeposition and characterization

of Ni–Mo alloys on Si and other substrates is covered in detail in Chapter 2. Notably, the observed activities under both acidic and alkaline conditions were quite high, but electrodeposited Ni–Mo exhibited poor stability under the strongly acidic conditions where Si photoelectrodes are stable.

Although they were unstable in strong acid, electrodeposited Ni–Mo alloys on Si microwire arrays showed promising activity and reasonable stability under mildly acidic conditions. As a result, we undertook a systematic effort to characterize the activity of Ni–Mo, as well as the better understood Ni and Pt single-component HER catalysts, on Si photoelectrodes. These results were published alongside basic deposition and characterization procedures in *Energy & Environmental Science*,[49] and are detailed in Chapter 3.

Subsequent work in collaboration with Emily Warren yielded Si n^+p-junction microwire arrays with energy conversion efficiencies approaching that of control samples deposited with Pt; these results were detailed in a later publication in *Energy and Environmental Science*.[50] A key result from this work, however, was that the observed energy conversion efficiencies of $<5\%$ were likely the highest that could be obtained for Si microwire arrays coupled to Ni–Mo catalysts. This limitation arises from the fact that electrodeposition yields catalyst coatings that are conformal over the entire microwire surface, resulting in a significant amount of deleterious light absorption by the catalyst layer. As a result, there is an inherent trade-off between catalyst activity and parasitic light absorption, both of which are proportional to the deposited mass. We concluded that the maximum attainable energy conversion efficiency for the photoelectrochemical HER on Si microwire arrays electrodeposited with Ni–Mo is around 5%, which is far too low for viable water splitting technologies.

The remainder of my thesis research efforts focused on mitigating the two key limitations we identified for the use of non-noble catalyst coatings: deleterious light absorption by the catalyst layer and the stability mismatch between Ni–Mo and Si. Regarding the problem of light absorption, I sought to develop a new photocathode design based on the use of Si microwire n^+p-junctions with non-noble HER catalysts. The design, which I call the "MEA" approach, was inspired both from commercial

electrolysis systems and a photovoltaic device design advocated by our collaborators in the Atwater group at Caltech. It involves selective placement of catalyst materials and a light-scattering layer at the bases of the microwire arrays. Along with Caltech undergraduate Carolyn Werlang, I developed a synthesis for Ni–Mo nanopowders that can be deposited selectively at the bases of the Si microwire arrays. This nanopowder synthesis and extensive characterization are included in Chapter 2; the details were published in *ACS Catalysis* in 2013.[51] Ni–Mo nanopowders also function as a crucial component of the MEA design, as described in Chapter 3. Much of the work on the Si/Ni–Mo MEA device approach is ongoing.

The end of Chapter 2 details work with Eric Popczun and Ray Schaak at the Penn State University on synthesis and characterization of a new, non-noble hydrogen evolution catalyst: Ni_2P nanoparticles. This work represents a fruitful collaborative effort wherein a clear hypothesis regarding the general viability of hydrodesulfurization catalysts for hydrogen evolution was developed through conversations between Nate and Ray in early 2012. Eric and I executed experiments drawing on the expertise of both research groups to test the hypothesis. The results were promising, and the work was submitted for publication in the Spring of 2013.[52]

In an attempt to address the stability mismatch between Ni–Mo and Si, I worked closely with Lewis Group graduate student Adam Pieterick to synthesize and characterize p-type WSe_2 photoelectrodes for the HER. We grew single crystals of p-WSe_2, deposited them with Pt HER catalyst, and observed impressive hydrogen evolution activity under strongly acidic, mildly acidic, and alkaline conditions. We also observed good stability for p-WSe_2 photocathodes under reducing conditions in aqueous solutions at pH 2 and 10, demonstrating high stability for this material under both acidic and alkaline conditions. We also characterized the semiconductor properties of as-synthesized p-WSe_2 crystals using spectral response measurements and electrochemical impedance spectroscopy, which together helped provide a full rationale for the observed photoelectrochemical HER activity. These results are described in detail in Chapter 4, and were published in the *Journal of the American Chemical Society* in 2013.[53]

The final components of this dissertation are a short conclusion in Chapter 5 and a set of appendices. Appendix A is list a symbols used throughout this dissertation. Appendix B is a detailed tutorial on execution of the electrochemistry experimentation that comprises the bulk of the work described herein. It covers theoretical and practical considerations in characterization of electrocatalysts and photoelectrodes, along with citations to publications with more extensive discussion. The main text of the dissertation was therefore written with the expectation that the reader has a working knowledge of the material contained in the appendices.

Chapter 2

Earth-Abundant Electrocatalysts

2.1 Introduction and Background

This chapter describes work on synthesis and characterization of earth-abundant electrocatalysts for the HER. In these efforts I collaborated closely with Emily Warren as well as two undergraduates, Mateo Martinez and Caroline Werlang. We focused primarily on Ni-based catalysts, especially mixtures of Ni and Mo (broadly referred to hereafter as Ni–Mo). Initial studies centered on reproducing previous results on electrodeposited Ni–Mo alloys. Subsequently we developed Ni–Mo electrodeposition methods that could be carried out under mildly acidic conditions, allowing for the generation of stable and active coatings on Si electrodes. We also developed a chemical synthesis for Ni–Mo nanopowders involving pyrolysis and reduction of homogeneous mixtures of Ni and Mo salts. These nanopowders were significantly more amenable to fundamental study than electrodeposited films, and exhibited high activity and stability toward the HER, especially under alkaline conditions. Finally, I collaborated with Eric Popczun and Raymond Schaak at The Pennsylvania State University to characterize the catalytic activity of Ni_2P nanoparticles toward the HER under acidic and alkaline conditions. These materials also showed promising activity and stability, especially under acidic conditions.

Silicon is a very poor catalyst for the HER. Therefore, in order to generate a Si photocathode that can efficiently produce hydrogen from aqueous solution, a catalyst (sometimes called a cocatalyst) must be used. The purpose of the catalyst is to accept

excited mobile electrons from the Si and efficiently transfer them to H^+ equivalents in solution for the net generation of H_2 gas. The processes of light absorption along with catalyzed and uncatalyzed charge transfer from Si to the hydrogen couple are shown schematically in Figure 2.1. The active catalyst species may be a soluble molecule or a heterogeneous solid material and may be either freely diffusing in solution or attached to the Si surface. Due to the relatively slow time constants associated with diffusion it likely is better to attach the catalytic species to the Si surface. Additionally, the best noble and non-noble hetereogeneous HER catalysts have demonsrated considerably higher activity than the best molecular systems. We focused our efforts on heterogeneous electrocatalysts in hopes of demonstrating proof-of-concept hydrogen evolving photocathodes incorporating exclusively non-noble components.

The activity of a heterogeneous electrocatalyst toward the HER depends on the strength of the interaction between the surface and bound hydride intermediates. As shown in Figure 2.2, the catalytic activities (approximated by j_0 values) of the transition metals can be plotted against the metal–hydrogen bond strength to give a peaked curve known as a "volcano plot."[48,54,55] At the peak of the plot lie the noble metals Pt, Re, Rh, and Ir, which have intermediate M–H bond strengths. This relationship is an example of the more general Sabatier principle,[56] which indicates that interaction between catalysts and substrates should be intermediate in energy to faciliate rapid binding of reactants and rapid release of the products.

The volcano relationship between bond strength and activity was rationalized specifically for the HER by Parsons and Gerischer independently in 1958.[57,58] Parsons' treatment, for example, showed that the activity of a hydrogen evolution electrocatalyst should increase to a maximum when the free energy of hydrogen adsorption (ΔG_{H}) is zero, regardless of the dominant reaction mechanism. Recent computational efforts, led by Nørskov and coworkers, have lent further support to this theory.[59–61] In fact, Nørskov et al. carried out DFT calculations to identify promising new HER catalysts on the basis of minimizing ΔG_{H}.[62,63] According to their computational results, the edge sites of MoS_2, a known hydrodesulfurization catalyst, exhibit adsorption energies comparable to that of platinum. Subsequent experimental work by Jaramillo

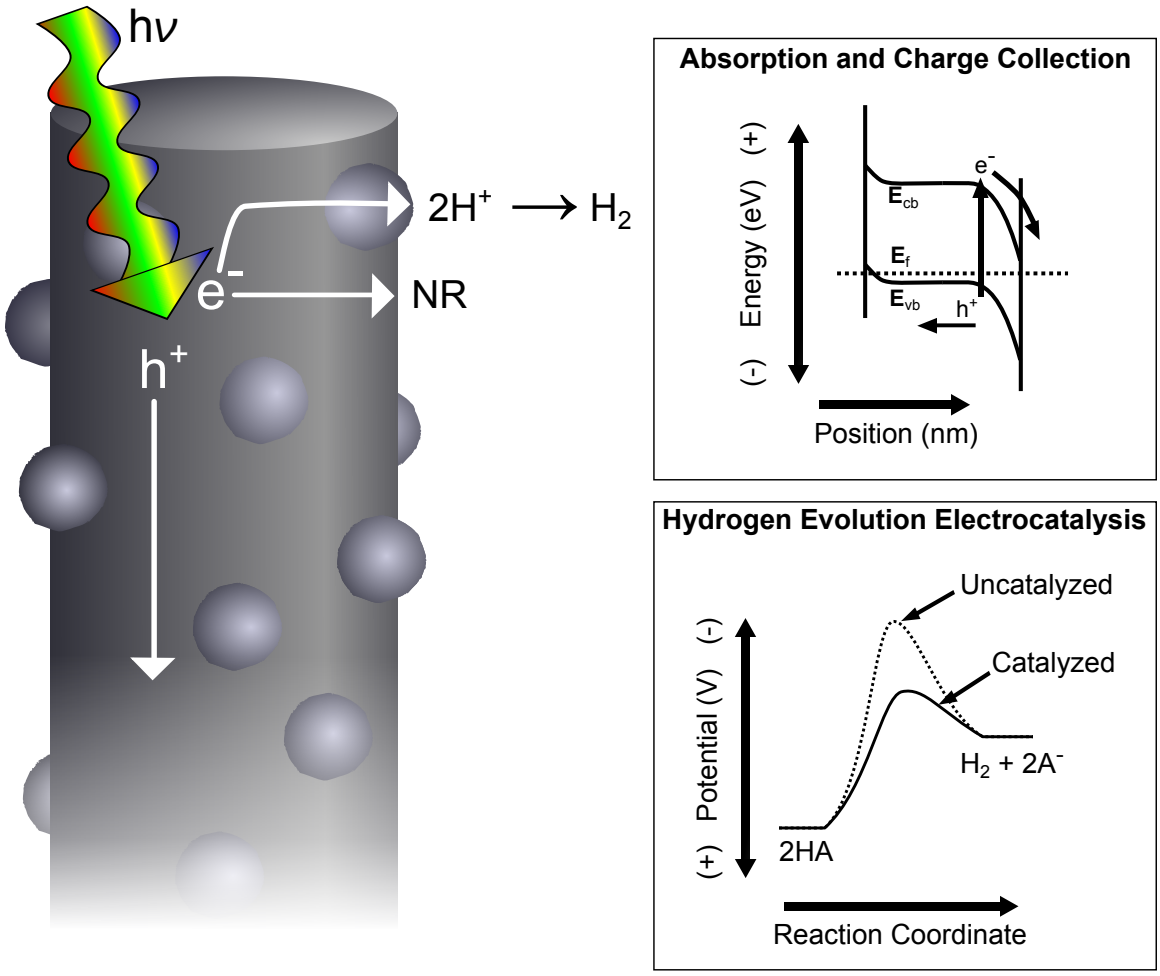

Figure 2.1. Schematic representation of the key processes in photoelectrochemical hydrogen evolution: light absorption, charge collection, and catalysis. The left image illustrates the intended path of photoexcited electrons and holes in a single Si microwire, as well as the need for a catalyst in order to successfully generate H_2. The boxes on the right depict a band diagram (top) and reaction coordinate diagram (bottom) of the respective energy and potential relationships operating during photoelectrochemical hydrogen evolution.

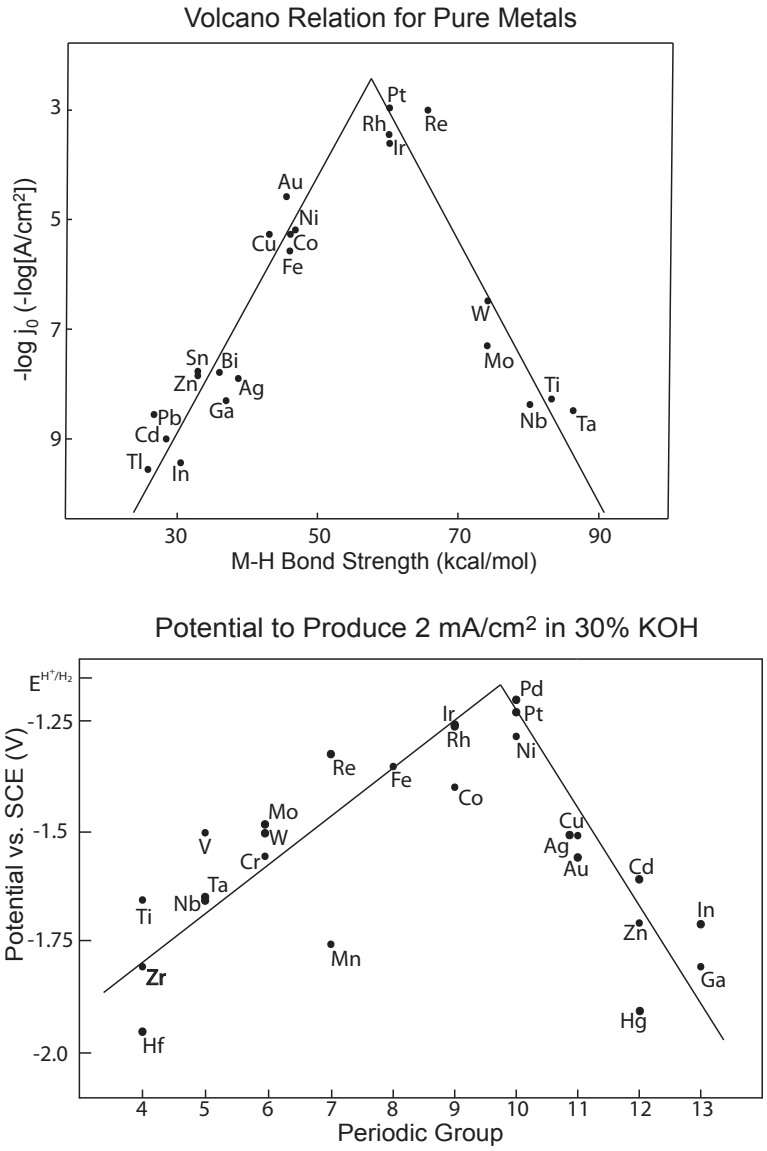

Figure 2.2. Volcano plots for the HER in acid and base solutions, from Walter et al.[48] Activities in acid are correlated to experimentally determined M–H bond strengths, whereas activities in base are correlated to periodic group, which is a rough proxy for M–H bond strength. Copyright 2010 the American Chemical Society; used with permission.

et al. showed that indeed MoS_2 edge sites were catalytically active toward the HER, although the per-atom activity was apparently closer to that of Ni than Pt.[64]

Nickel-based electrocatalysts are well precedented in electrochemistry literature as non-noble alternatives to Pt for the HER, especially under alkaline conditions.[65] Although pure Ni metal is the most active single component, non-noble HER catalyst, it is still approximately three orders of magnitude lower in activity than Pt metal. However, many researchers have reported that mixing Ni with another transition metal results in increased HER activity relative to pure Ni metal. A large number of researchers have reported particularly high activity for composites including Ni and Mo.[66–87] These Ni–Mo or Ni–Mo–X (where X is a third element such as Fe or Cd) materials, synthesized by a variety of methods, exhibited one or even several orders of magnitude higher j_0 values and lower Tafel slopes than pure Ni electrodes.

2.2 Electrodeposited Ni-based Catalysts

Heterogeneous catalyst coatings can be deposited easily onto electrode substrates by the electrodeposition technique, which involves electrochemical oxidation or reduction of solution species so as to generate the active catlayst (or catalyst precursor) as an insoluble film directly on the electrode surface. Many of the most active Ni–Mo HER catalysts were generated by electrodeposition.[69,73–78,87] Therefore we sought to use electrodeposition to generate Ni–Mo composites on Si substrates.

Electrodepositions of metallic alloys containing Mo proceed by complex reaction mechanisms.[88–90] Molybdate salts, which are generally used as the Mo precursor, cannot generate pure Mo metal by cathodic electrodeposition under aqueous conditions. Instead the molybdate is only partially reduced to a solid molybdenum sub-oxide, MoO_2^{n-}. When transition metals such as Ni, Co, or Fe are added to molybdate solution, however, cathodic deposition results in formation of a metallic alloy of the two components.

For Ni–Mo in particular, Chassaing et al. proposed a series of elementary steps as in Equations 2.1–2.3, involving initial formation of a mixed Ni–Mo oxide followed by

chemical reduction by coevolved H_2.[90]

$$Ni^{2+} + MoO_4^{2-} \xrightarrow{+e^-} NiMoO_x \tag{2.1}$$

$$2\,H_2O \xrightarrow{+e^-} H_2 + 2\,OH^- \tag{2.2}$$

$$xH_2 + NiMoO_x \longrightarrow NiMo + xH_2O \tag{2.3}$$

It is also possible that the Mo reduction is due to adsorbed hydrogen species that are intermediates for the HER and not dissolved or gaseous H_2. In either case, successful deposition of metallic Ni–Mo only proceeds under electrochemical conditions where H_2 evolution also proceeds.

We first attempted to reproduce several literature results regarding electrodeposition of Ni–Mo films onto conventional substrates such as glassy carbon. Then we attempted to adapt these deposition procedures for use on Si substrates. Silicon is a particularly convenient substrate for studying electrodeposited catalysts for PEC hydrogen evolution, as it can be lightly doped (e.g., p-Si or n-Si) to give photoactivity and also degenerately doped (e.g., p^+-Si or n^+-Si) to exhibit metallic conductivity. For these initial studies of catalyst deposition and activity, we used degenerately doped Si to provide a direct comparison to glassy carbon and avoid any convoluting effects due to the semiconducting behavior of Si.

The compositions of two previously reported solutions that we used for Ni–Mo deposition are shown in Table 2.1. We were able to successfully generate active Ni–Mo coatings on glassy carbon substrates using these plating baths. However, depositions on p^+-Si under identical conditions did not yield high HER catalytic activity. A comparison of the Tafel behavior of Ni–Mo depositions from an alkaline citrate solution under identical conditions on n^+-Si and glassy carbon are shown in Figure 2.3. Interestingly, the activity of n^+-Si electrodes toward the HER were enhanced after the deposition, but not to the same extent as were the glassy carbon electrodes. Based on subsequent experience with characterization of various HER electrocatalysts, the activity of the n^+-Si electrodes deposited from the alkaline citrate Ni–Mo solution was, in fact, reminiscent of a nanostructured pure Ni coating, implying

Table 2.1. Compositions of two alkaline Ni–Mo deposition solutions from prior literature reports of high HER activity

solution	pyrophosphate (with Cd)	alkaline citrate
reference	Stachurski, et al.[69]	Raj and Venkatesan[73]
Ni source	73 mM $NiCl_2$	0.3 M $NiSO_4 \cdot 6\,H_2O$
Mo source	33 mM Na_2MoO_4	80 mM $Na_2MoO_4 \cdot 2\,H_2O$
pH (buffer)	8 (0.9 M bicarbonate)	10.5 (excess carbonate)
other components	145 mM $Na_4P_2O_7$	150 mM $K_3C_6H_8O_7 \cdot H_2O$
	25 mM $N_2H_4 \cdot H_2SO_4$	
	4 mM $Cd(NO_3)_2$	
	0.2 mM NaSCN	
	1.3 M NaCl	
deposition parameters	galvanostatic at -10 mA cm^{-2}	galvanostatic at -10 mA cm^{-2}
	tens of minutes	>1 hour

selective deposition of Ni from the solution containing both Ni(II) and molybdate.

Clearly there was a problem with the use of Si substrates along with literature Ni–Mo depositions. We believe that the high pH of the solutions was likely to blame, as the Si surface is prone to rapid oxidation in solutions with high concentrations of OH^-. This oxidation might decrease adhesion of the coating to the surface. Alternatively a surface Si oxide that forms rapidly in alkaline solution might greatly inhibit hydrogen evolution activity, even compared to pure Si, which would then prevent Ni–Mo codeposition and perhaps favor formation of pure Ni and reduced Mo oxides on the surface instead. This would explain the observed catalytic behavior resembling that of pure Ni coatings. We proceeded with attempts to develop acidic deposition solutions for Ni–Mo, in hopes that they would be compatible with conventional substrates and with Si.

2.3 Si-Compatible Ni and Ni–Mo

Although a few nearly neutral Ni–Mo deposition solutions have been reported in the literature,[86,87] acidic depositions were not precedented, presumably due to the tendency for molybdates to form insoluble "molybdenum blue" species in acidic solution.[91] In attempts to develop a Si-compatible deposition method, we took the

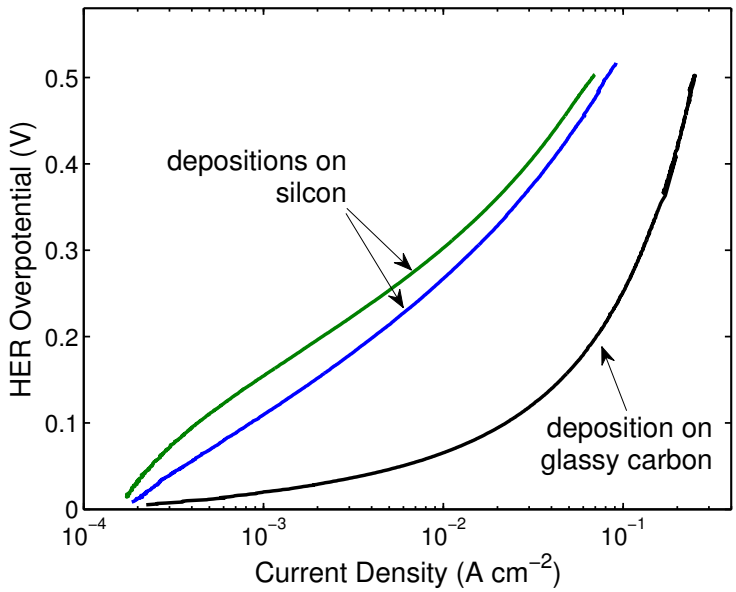

Figure 2.3. Comparison between Tafel data collected for Ni–Mo films deposited by identical methods onto glassy carbon and silicon. Depositions were from the alkaline citrate solution detailed in Table 2.1 under galvanostatic conditions at -10 mA cm^{-2} for 90 minutes each. Tafel data were collected in a H_2-saturated 0.5 M H_2SO_4 solution under pseudo-steady state conditions, without iR compensation, using a two chamber cell with a Pt counter electrode contained in a separate fritted compartment.

approach of first depositing pure Ni, and then adding Mo to the deposition solution in order to understand how the dynamics and products of deposition on Si are perturbed by Mo. We began with a mildly acidic nickel sulfamate deposition solution,[92] which had been used previously in the Lewis group for electrodeposition of Ni on Si and other semiconductor substrates.[93]

Figure 2.4 shows the j–E behavior for a n^+-Si electrode undergoing cyclic voltammetry in solutions containing ∼1 M Ni sulfamate and varying concentrations of Na_2MoO_4. The pure Ni solution gave a rapid onset of cathodic current with no hysteresis, indicative of a kinetically facile process. With increasing [Mo], however, the cathodic current was progressively supressed such that at [Mo] = 0.5 M, the current was negligible over the same potential range that produced $|j| > 100$ mA cm^{-2} from the pure Ni bath. Some hysteresis was also observed with added Mo, indicating mass transport limitations or a decrease in the kinetic facility of the electrode surface over the course of the measurement.

Interestingly, cycling the potential of the pure Ni solution several times over the potential range shown in Figure 2.4 resulted in a thick, dense, slightly yellowish metal coating on the Si electrode surface, with no evidence of bubble formation. This coating, upon reaching a sufficient thickness, often began to peel away from the electrode surface. All of these observations indicate that essentially all the observed cathodic current density was due to metal deposition. Upon addition of Mo, however, continuous films did not form and we observed copious bubble formation on the electrode surface at large negative potentials.

We concluded from these Mo concentration studies that addition of molybdate severely inhibits the deposition of Ni metal on the electrode surface, allowing for some hydrogen evolution. However, additional Mo also generally decreased cathodic current, implying that molybdate also inhibits hydrogen evolution. Based on these results, we attempted to codeposit Ni and Mo from a bath containing a high concentration of Ni and a comparatively low concentration of Mo. The final deposition bath composition, as well as that of a subsequently developed acidic citrate bath, are shown in Table 2.2. Both of these mildly acidic deposition solutions were found to

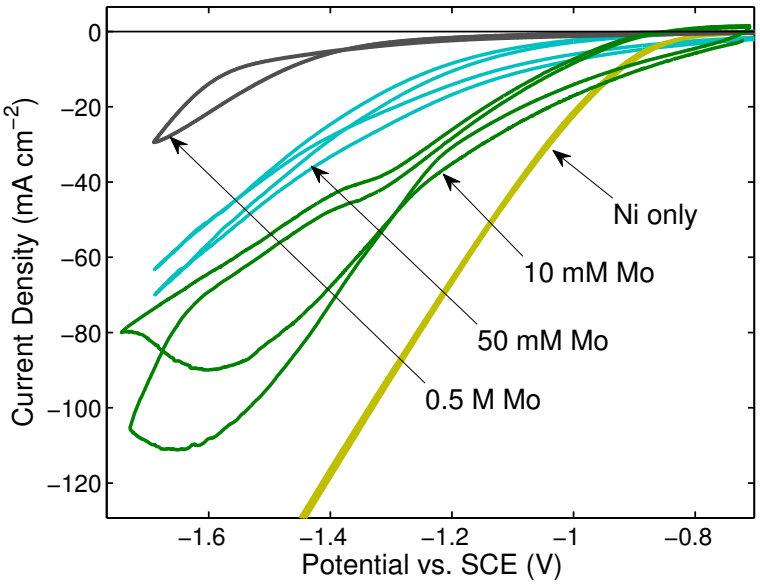

Figure 2.4. Cyclic voltammetry data for n^+-Si electrodes. The electrolyte consisted of ∼1 M nickel sulfamate and 0.5 M boric acid, and the counter electrode was a large area Ni foil contained in the same chamber as the working electrode. Mo was added in the form of $Na_2MoO_4{\cdot}2\,H_2O$ in the noted concentrations. Increased [Mo] clearly supressed cathodic current density from Ni deposition and/or hydrogen evolution.

give active Ni–Mo composite coatings on Si electrodes as well as conventional conductive substrates. Both solutions were also stable over months of storage, with no evidence of changes in pH or precipitation of molybdate species.

We spent considerable time optimizing parameters for the Ni–Mo sulfamate deposition solution, resulting in consistent nanostructured coatings of Ni–Mo on various substrates. We found the best deposition conditions for planar substrates involved holding at constant cathodic current densities of 10–50 mA cm^{-2}. Potentiostatic deposition could also be used at potentials ranging from −1.1 to −1.3 V vs. Ag/AgCl, which also produced average cathodic current densities of a few tens of mA cm^{-2}. Deposition at smaller potentials or currents generally resulted in an inactive blue or purple coating, which we believe to be pure Mo oxide. Deposition at larger potentials or currents often resulted in copious hydrogen evolution but little or no coating.

The deposition dynamics of Ni–Mo from sulfamate solution were similar to those described in previous reports, in that the active coating was only obtained upon

Table 2.2. Compositions of two new Ni–Mo deposition solutions with mildly acidic pH values.

solution	sulfamate	acidic citrate
Ni source	1 M $Ni(SO_3N_2)_2$	10 mM $NiSO_4$
Mo source	20 mM Na_2MoO_4	5 mM Na_2MoO_4
pH (buffer)	4 (0.5 M borate)	4.8 (0.4 M citrate)
other components	(none)	0.2 M NaCl
		0.5 M NH_4Cl
deposition parameters	galvanostatic at -20 mA cm^{-2}	potentiostatic at -1.6 V vs. SCE
	seconds to minutes	minutes

coevolution of hydrogen. Figure 2.5 shows *i*–*t* and *i*–*E* traces for potentiostatic deposition and linear sweep stripping of a Ni–Mo film on a fluorine-doped tin oxide (FTO) electrode. Based on integration of the total charge passed during deposition and stripping, we determined that the deposition current efficiency (DCE), or the proportion of the total current corresponding to deposition, for Ni–Mo sulfamate was ∼3%, and relatively insensitive to the total deposition time interval. Comparatively, pure Ni deposition from an identical solution without addition of sodium molybdate gave DCE values of ∼100%.

Ni–Mo films of various mass loadings could be deposited onto Si or other substrates by controlling the total charge passed during deposition, and the resulting catalytic activities increased with increasing loading. Figure 2.6 shows the HER activities and optical images of Ni–Mo coatings deposited over a range of integrated deposition charge densities onto transparent FTO substrates.

Relatively thick coatings could be scraped off of the surface of the substrate and analyzed with respect to composition and crystallinity. Figure 2.7 shows transmission electron micrographs, EDS compositional analysis, and an electron diffraction image for a scraped Ni–Mo film. The coatings exhibited nanocrystalline morphologies and the electron diffraction suggested a single phase matching the cubic crystal structure of nickel. from which we concluded that the electrodeposited material consisted largely of a substitutionally dissolved alloy of Mo in Ni. Compositional analysis suggested a bulk composition of 85% Ni and 15% Mo, which was largely independent of deposition time or potential.

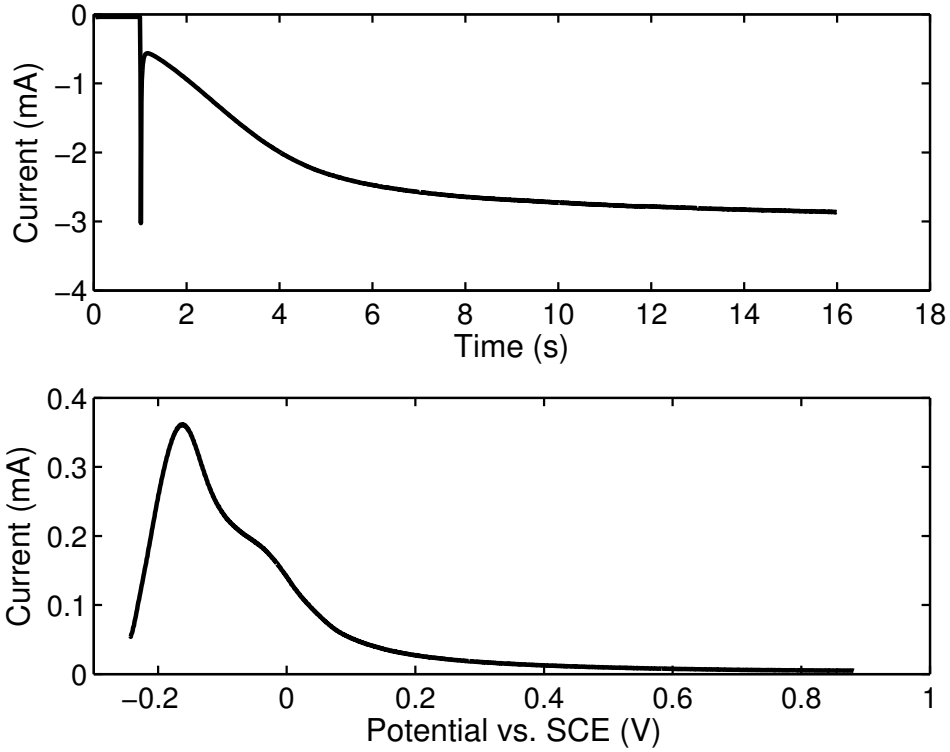

Figure 2.5. Electrochemistry data illustrating the low DCE for Ni–Mo films derived from sulfamate solution. Top: Current vs. time trace of the potentiostatic deposition of a Ni–Mo film at −1.25 V vs. Ag/AgCl on a FTO electrode, using a Ni foil counter electrode in the same compartment as the working electrode. Bottom: Current vs. potential trace of a stripping wave in 1 M sulfuric acid solution of the same film at a sweep rate of 50 mV s^{-1}, using a Pt counter electrode in a seperate fritted compartment. Data from McKone et al.[49]

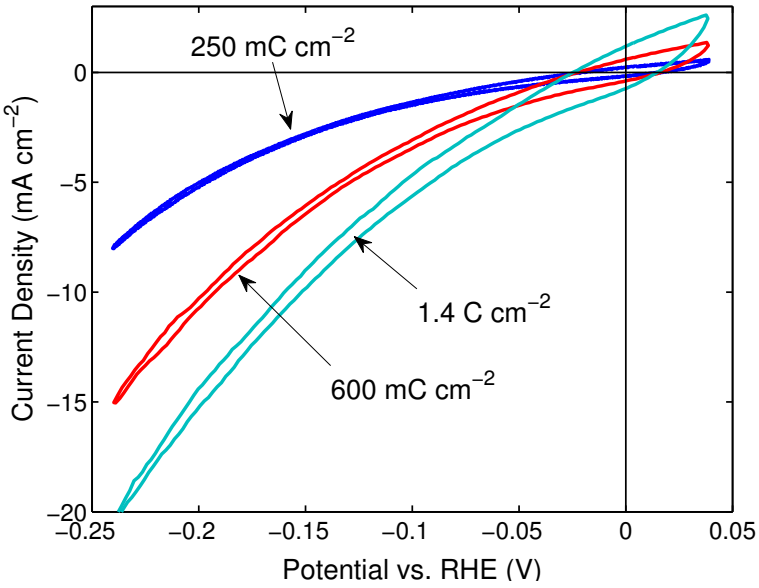

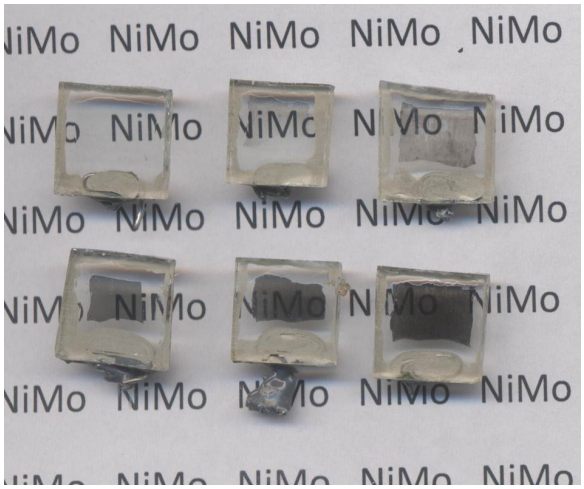

Figure 2.6. Top: j–E data for hydrogen evolution from Ni–Mo films deposited onto FTO substrates from sulfamate solution with the noted total charge density passed during deposition. Data were collected without iR compensation, in a H_2-saturated potassium phosphate solution at pH $\approx$ 6, in a two-chamber cell using a Pt counter electrode in a separate fritted compartment and a SCE reference electrode in the working compartment. Bottom: photograph of Ni–Mo/sulfamate films on FTO substrates deposited with increasing charge densities ranging from zero (upper left) to $\sim$1.5 C cm^{-2} (lower right). The Ni–Mo films are the dark gray-black deposits in the centers of the samples, whereas the light gray outlines are Ag paint used for electrical contact.

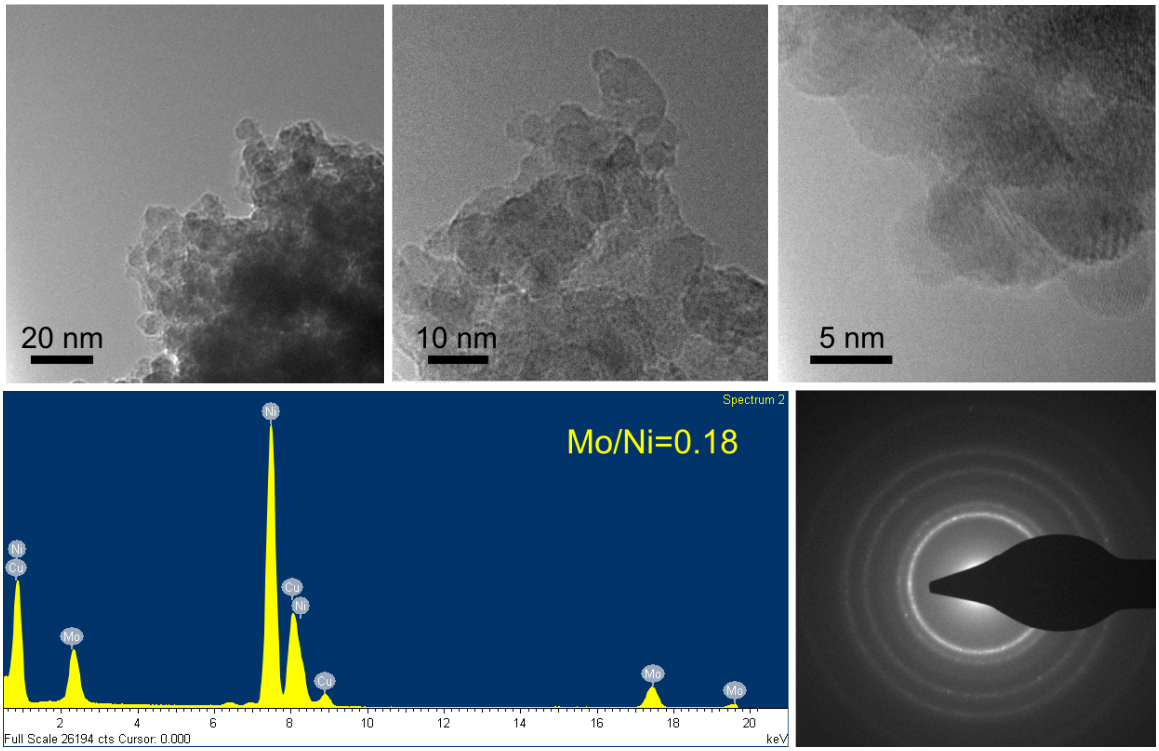

Figure 2.7. Compiled TEM, composition, and diffraction data for Ni–Mo catalyst deposited from sulfamate solution onto a Si substrate. The film was scraped from the Si surface using a razor blade, suspended in isopropanol with sonication, and deposited onto a copper TEM grid. Data from McKone et al.[49] Copyright 2011 the Royal Society of Chemistry; used with permission.

Initial studies of sulfamate Ni–Mo HER activity were carried out under a variety of conditions, including strongly acidic and nearly neutral aqueous solutions. These experiments gave inconsistent results, especially for electrodes that remained submersed in solution between experiments. Initial potentiostatic and galvanostatic experiments implied low stability for the Ni–Mo films under both neutral (potassium phosphate, KP_i) and acidic (H_2SO_4) solutions. Therefore we carried out a simple stability assay, wherein catalyst coatings were deposited onto FTO substrates and then placed in sealed vials containing hydrogen-purged aqueous solutions with various electrolytes. These films were then imaged using a digital camera over a period of several days at consistent intervals to directly observe the relative rates of catalyst corrosion. Results for this experiment are shown in Figure 2.8, which depicts the catalyst films at the beginning of the experiment and approximately 2 days, 16 hours later.

Corrosion of the Ni–Mo coating in contact with 0.5 M H_2SO_4 began immediately, and the majority of the coating had dissolved even before the vials could be arranged and the first photograph collected. Over the entire time course of the experiment, the catalyst films corroded completely in H_2SO_4, potassium hydrogen phthalate (KHP), and KP_i solutions. Partial corrosion was observed in K_2SO_4 solution and in deionized water. In sodium hydroxide solution and KHP + K_2SO_4 solution, the Ni–Mo coating was apparently protected from corrosion. Such protection in NaOH solution is consistent with previous precedent for Ni–Mo electrocatalysts being stable under alkaline conditions.[68] However, the apparent protection afforded by phthalate/sulfate solution, but not from either of the components alone, is as yet unexplained. Based on this result, we carried out subsequent studies in mildly acidic solutions buffered with KHP and containing K_2SO_4 supporting electrolyte, which did result in improved consistency in HER data for Ni and Ni–Mo catalysts. Even in KHP solution, though, we found that stability was limited to a few hours of electrochemical testing before observing noticable degradation in electrocatalytic activity for Ni and Ni–Mo catalysts.

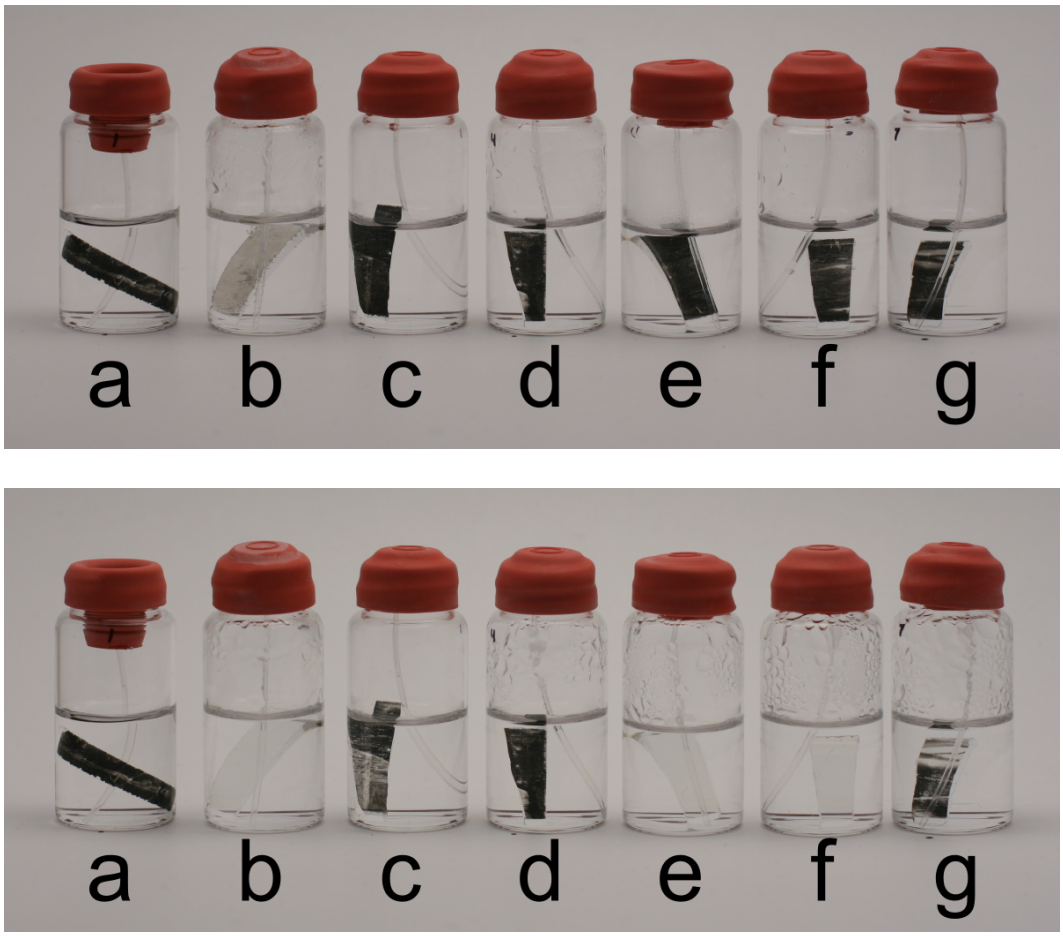

Figure 2.8. Photographs of a set of FTO substrates coated with Ni–Mo films deposited from sulfamate solution in a variety of electrolytes, from a time-lapse series. Top: initial photograph taken within a few minutes of submersing films into the solution. Bottom: end point photograph taken approximately 64 hours later, showing qualitatively the extent of dissolution of the films in each electrolyte. All the solutions were sparged with H_2 gas and sealed before submersing the Ni–Mo/FTO. Electrolytes were as follows: (a) 0.5 M NaOH; (b) 0.5 M H_2SO_4; (c) 0.5 M K_2SO_4; (d) 0.5 M K_2SO_4 + 0.1 M KHP; (e) 0.1 M KHP; (f) 0.5 M KP_i at pH 6.3 + 0.3 M K_2SO_4; (g) deionized water.

2.4 Catalyst Comparison on Si Substrates

In order to elucidate the viability of electrodeposited Ni–Mo for use in Si-based hydrogen evolving photocathodes, we carried out a comparative study of its activity alongside pure Ni and Pt films on p^+-Si electrodes in both planar and microwire geometries. Pure Ni films could also be deposited from sulfamate solution without any additional Mo, but signficantly shorter deposition times were required in order to generate coatings with a comparable amount of deposited material due to the high DCE for pure Ni. Highly active Pt films were deposited by electron-beam (e-beam) evaporation, the same method we used previously to generate active Pt coatings on Si n^+p junctions.[46]

Figures 2.9 and 2.10 show scanning electron micrographs of Ni and Ni–Mo coatings on planar and microwire Si substrates, respectively. Evaporated Pt films were so thin that they could not be clearly imaged in the electron microscope. The morphologies of the Ni and Ni–Mo coatings were quite similar, consisting of agglomerates of particles several hundreds of nm in diameter. However, as the deposition thickness was increased, the Ni–Mo coatings remained porous and generated multiple catalyst layers, whereas the pure Ni coatings coalesced into continuous films. On microwires the films were similarly structured, but in some cases the deposits were thicker toward the tops of the microwires compared to the bases.

In spite of the similar morphologies, the HER activities of the various catalyst coatings were quite different. Figure 2.11 shows j–E data representative of the best HER performance obtained for the various catalysts, as well as for bare Si surfaces, under mildly acidic conditions. Ni films exhibited significantly enhanced HER activity compared to bare Si. Ni–Mo films, in turn, exhibited higher activity than Ni, and Pt was higher in activity than Ni–Mo. Additionally, all the electrocatalysts exhibited higher HER activities on microwire arrays compared to planar substrates. In particular, the current density at a given overpotential for Ni and Ni–Mo films was consistently larger by approximately 4 times for microwires compared to planar substrates. We attributed this enhancment to the ∼5-fold increase in geometric surface

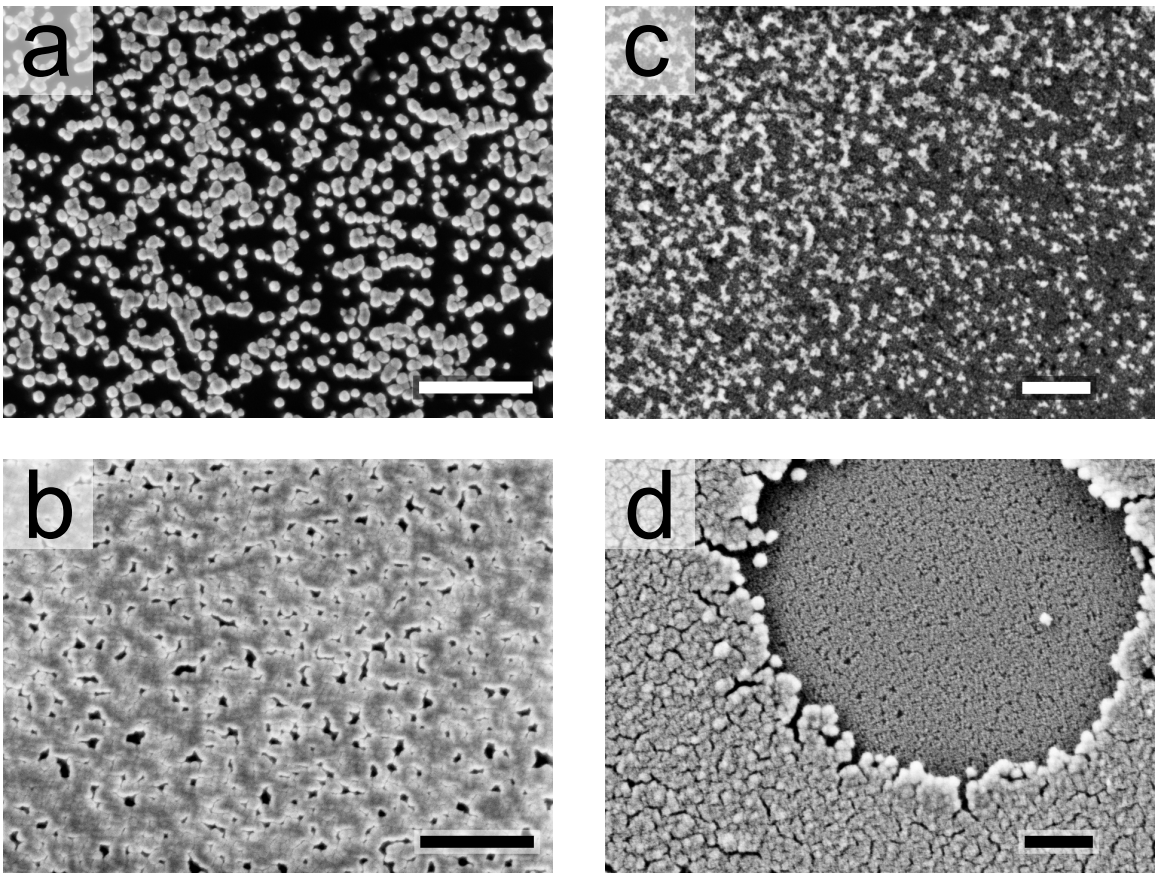

Figure 2.9. Scanning electron micrographs of Ni and Ni–Mo films deposited from sulfamate solutions onto planar Si substrates: (a) Ni deposited for 0.5 s; (b) Ni deposited for 1.0 s; (c) Ni–Mo deposited for 30 s; (d) Ni–Mo deposited for 90 s. Scale bar in each panel is 1 μm. Adapted from McKone et al.[49] Copyright 2011 the Royal Society of Chemistry; used with permission.

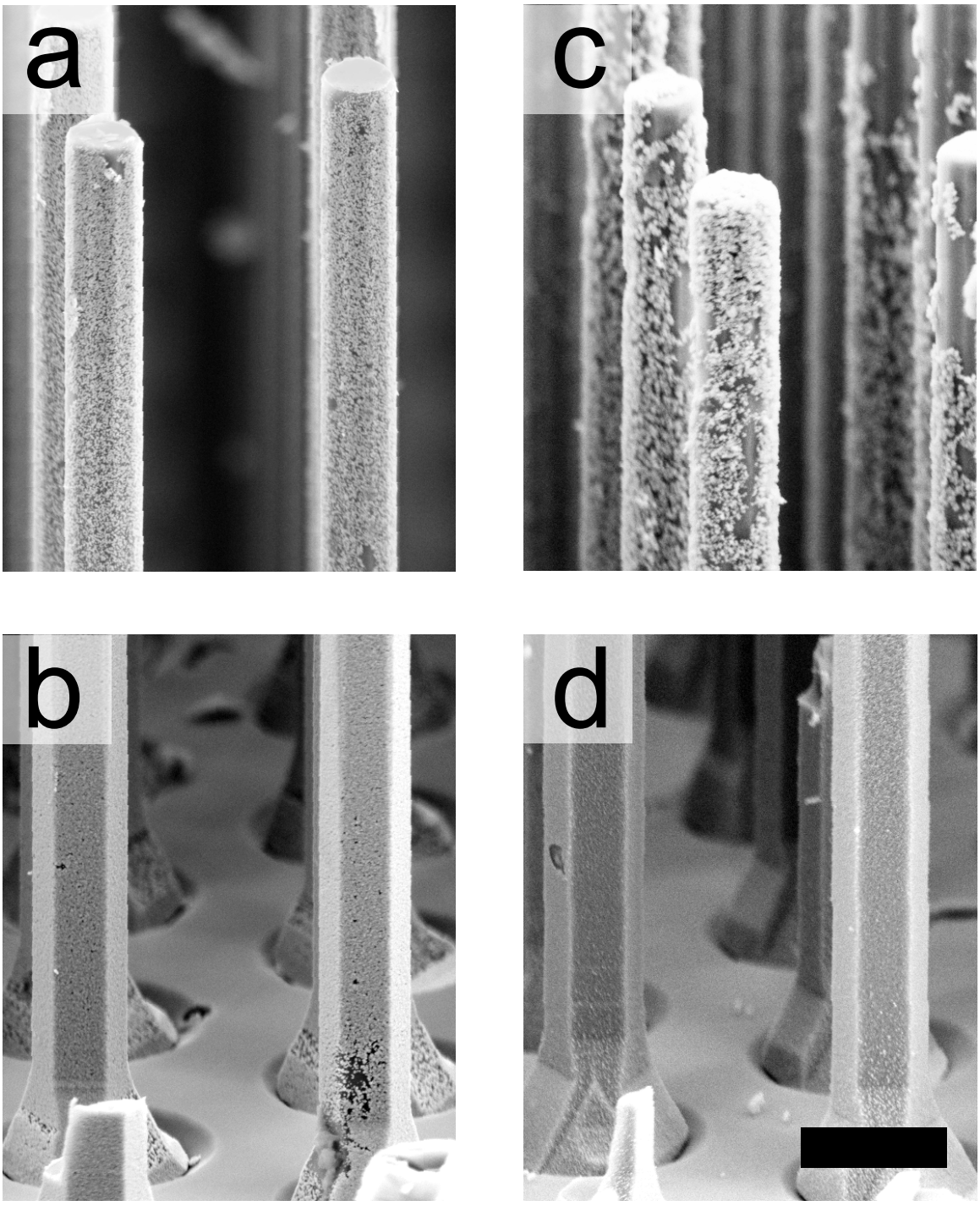

Figure 2.10. Scanning electron micrographs of Ni and Ni–Mo films deposited from sulfamate solution onto p^+-Si microwire substrates: (a–b) Ni deposited for 5 s; (c–d) Ni–Mo deposited for 90 s. Scale bar in panel (d) is 3 μm and applies to all panels. Adapted from McKone et al.[49] Copyright 2011 the Royal Society of Chemistry; used with permission.

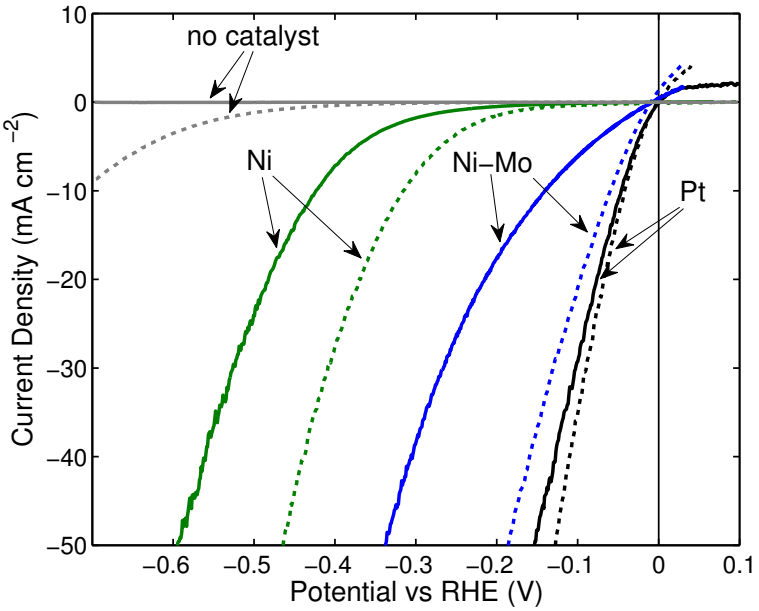

Figure 2.11. Hydrogen evolution j–E characteristics of various catalyst films deposited on planar (solid lines) and microwire (dashed lines) substrates. Ni and Ni–Mo were deposited from sulfamate solution, and Pt was deposited using e-beam evaporation. Data were collected without iR compensation under pseudo-steady state conditions in a two-chamber cell using a Pt counter electrode in a separate fritted compartment and a SCE reference in the working compartment. Electrolyte was 0.5 M K_2SO_4 with 0.2 M KHP buffer at pH 4.5, saturated with H_2.

area per project area afforded by the high aspect-ratio wire structure compared to a planar substrate. Since the incoming solar flux for a photoelectrochemical device is proportional to the electrode projected area rather than the geometric area, this surface-area enhancement would contribute directly to increased photocathode energy conversion performance.

Interestingly, the increase in catalytic activity we observed upon transitioning from planar to microwire substrates was much smaller for Pt catalyst than for Ni or Ni–Mo. We attribute the lack of enhancement for Pt to the already high activity of evaporated Pt films toward the HER on planar substrates. Sluggish kinetics are only one source of overpotential in hydrogen evolving cathodes, where other sources include bulk and interfacial resistances, solution resistance, and concentration overpotentials. We believe that the HER electrocatalytic activity of Pt on planar Si substrates, as shown in Figure 2.11, already approaches the highest activity that can be obtained

under the noted conditions. Therefore the surface-area enhancement afforded by the wire structure did not significantly enhance Pt HER electrocatalytic activity.

Due to the signficant enhancement in catalytic activity for Ni–Mo in transitioning to the microwires, and the small enhancement for Pt, the activities of these two materials on microwires were actually quite similar. We conclude that Ni–Mo films deposited onto high aspect ratio substrates can attain "Pt-like" catalytic activity relative to the projected area of the electrode. Therefore, Ni–Mo is indeed a viable non-noble catalyst for use in a hydrogen evolving photocathode alongside Si light absorbers. In light of these results, we undertook efforts to develop improved syntheses of Ni–Mo materials, as described in the following section, and we also characterized the behavior of Ni–Mo on photoactive Si substrates, as described in Chapter 3.

2.5 Ni–Mo Nanopowder

After extensive efforts using Si substrates, we determined that electrodeposition of non-noble catalysts such as Ni–Mo alloys is not the optimum method for generating composite Si photocathodes. In particular, the Ni sulfamate deposition bath is not amenable to tuning the resulting Ni–Mo composition. Additionally, mass loading of the catalyst is difficult to control and to measure using electrodeposition. Also, only one sample can be prepared at a time, making statistical analysis of the resulting catalytic properties challenging. Finally, we concluded that spatial control over the location of deposited material would be useful, as discussed in Chapter 3. Achieving such control demanded a synthetic method for Ni–Mo that was independent of the substrate on which it was to be deposited.

There is significant precedent for generating active Ni–Mo materials by chemical rather than electrochemical means. For example, the method of Brown and Mahmood, researchers at BP labs, involved pyrolysis of an ammonia solution of $Ni(NO_3)_2$ and ammonium molybdate onto a Ni or steel substrate.[66–68] The pyrolyzed coating, presumably a mixed oxide, was then reduced under a hydrogen atmosphere to generate a highly active Ni–Mo electrode. In fact, the Brown-Mahmood pyrolysis/reduction

method was used to generate the most active reported Ni–Mo catalysts, when operated under industrial alkaline electrolysis conditions. According to a patent awarded in 1982, the BP researchers achieved HER current densities of 1 A cm^{-2} at $\eta = 135$ mV using Ni–Mo catalyst coatings with a mass loading of 7.4 mg cm^{-2}.[67] They later reported that coatings generated by this method were stable under operating conditions in 30 wt% KOH soluton at 70 °C for over 10,000 hours (>1 year) of continuous operation.[68]

The Brown-Mahmood synthetic method suffers from the fact that it requires direct pyrolysis or deposition of oxidized Ni–Mo precursors onto the desired electrode substrate. Given the sensitivity of Si and other absorber materials to high temperatures as well as oxidizing or reducing conditions, this is not a reasonable approach to generating active coatings for HER photocathodes. Alternatively, there is precedent for generating mixed Ni–Mo oxide nanoparticles using solution phase methods. In particular, Levin et al. reported in 1996 the formation of a mixed ammonium nickel molybdate powder on heating an ammoniacal mixture of Ni(II) and ammonium molybdate under aqueous conditions.[94] Additionally, Schmitt et al. reported a series of transition metal molybdate and tungstate nanoparticle syntheses accomplished by simply mixing the desired transition metal salt with ammonium molybdate or tungstate in polyol media.[95] These researchers believed that the resulting nanoparticulate oxides were stabilized by coordination of the polyol to the particle surfaces, resulting in small and relatively monodisperse mixed oxides that were stable in colloidal solution.

We developed a chemical method for the synthesis of Ni–Mo nanopowders by a two-step process involving initial precipitation of a mixed Ni–Mo oxide from polyol solution, adapted from to the approaches of Levin and Schmitt. The resulting oxide powder was purified and reduced under a hydrogen atmosphere, according to the method of Brown and Mahmood. A synthetic scheme, illustrating the appearance and composition of the starting solution, intermediate oxide, and final catalyst material, is shown in Figure 2.12.

The first reaction step gave Ni–Mo oxide precipitates when carried out in gly-

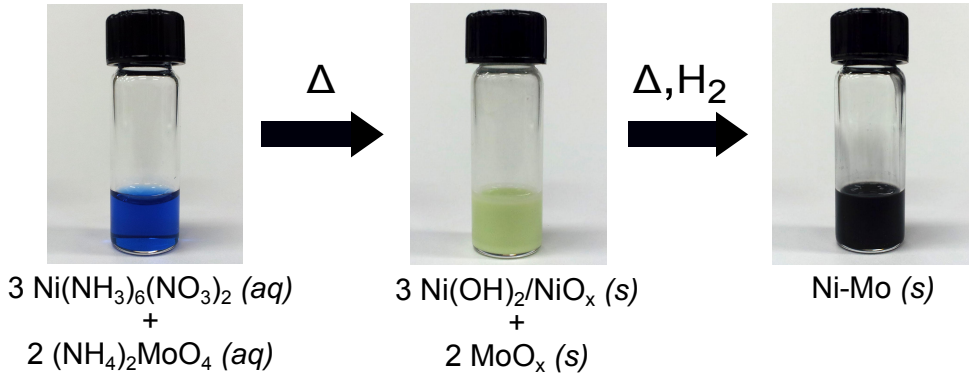

Figure 2.12. Synthetic scheme for Ni–Mo nanopowders consisting of precipitation of a mixed Ni–Mo oxide from ammonia solution followed by thermal reduction under a hydrogen atmosphere. From McKone et al.[51] Copyright 2013 the American Chemical Society; used with permission.

col solutions and in water, but diethylene glycol consistently gave the most uniform, submicron particles. Figure 2.13 shows scanning and transmission electron micrographs of the intermediate mixed Ni–Mo oxide and the final Ni–Mo nanopowder. The mixed oxide exhibited primary particle sizes of several hundred nm by SEM, each of which appeared as agglomerates of smaller amorphous particles by TEM. The reduced catalyst powder retained a similar primary particle size by SEM, but the TEM analysis indicated markedly increased crystallinity and porosity. The reduction process likely removed a significant quantity of oxygen as water vapor, thus bringing about a large volume contraction in the solid. The annealing temperatures (400–500 °C) were sufficiently low not to allow for migration of the solid Ni–Mo component, and so the volume contraction resulted in formation of void spaces. We believe these voids greatly enhanced the electrochemically active surface area for HER catalysis.

The Ni–Mo nanopowders could be readily processed into electrodes by suspending the solid in a suitable solvent medium, such as isopropanol, and deposited onto a desired substrate by dropcasting, painting, spincoating, etc. The resulting coating, however, needed to be "activated" by heating again to 400–500 °C briefly under a reducing atmosphere, as in the initial synthesis. We believe this activation step sinters the particles and reduces a surface oxide that forms upon air exposure, increasing the electrical conductivity of the catalyst coating. The as-synthesized powder was mildly

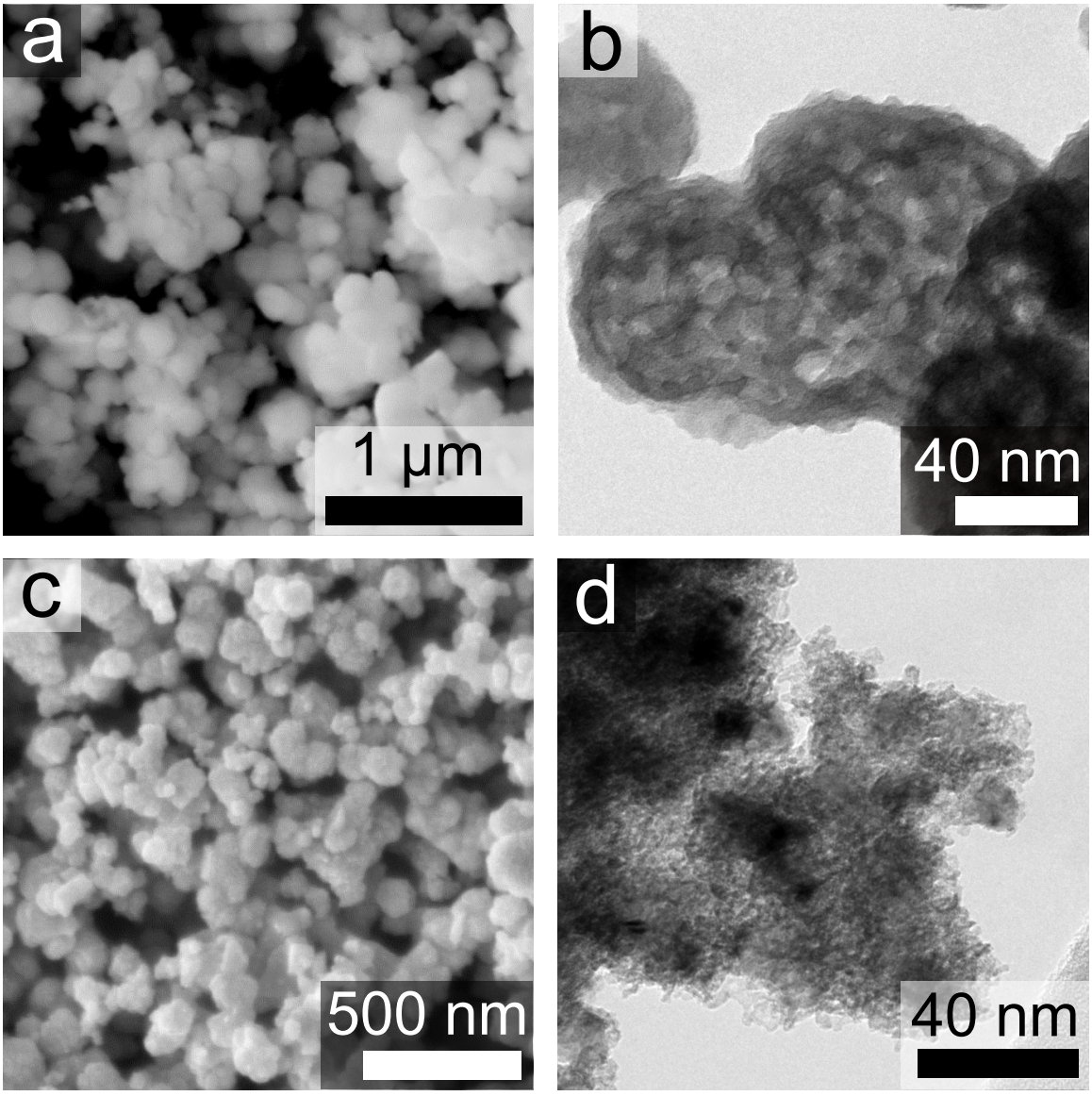

Figure 2.13. Electron micrographs of Ni–Mo oxide and Ni–Mo nanopowders: (a) SEM of Ni–Mo oxide; (b) TEM of Ni–Mo oxide; (c) SEM of Ni–Mo; (d) TEM of Ni–Mo. From McKone et al.[51] Copyright 2013 the American Chemical Society; used with permission.

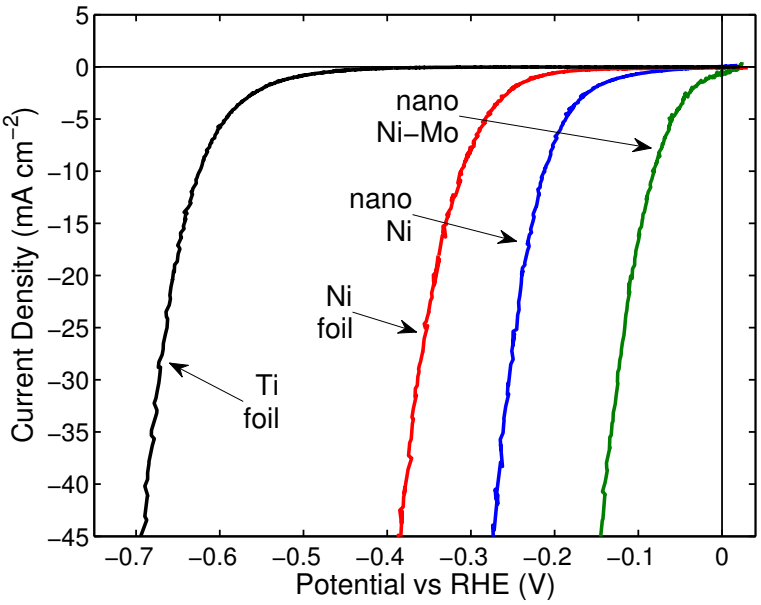

Figure 2.14. Pseudo-steady state HER j–E characteristics of the noted catalyst materials in H_2-saturated 1 M NaOH aqueous solution. "Nano Ni" and "nano Ni–Mo" refer to nanopowders of Ni and Ni–Mo synthesized by the precipitation-reduction method, with mass loadings of ∼1 mg cm^{-2} on Ti substrates. Data were collected using a single-chamber cell using a Ni mesh counter electrode and a Hg/HgO reference. Contact and solution resistances were compensated using the current-interrupt method. From McKone et al.[51] Copyright 2013 the American Chemical Society; used with permission.

pyrophoric upon removal from the initial reduction step, suggesting that the finely divided metal mixture is strongly prone to oxidation in air.

Upon activation, the Ni–Mo electrocatalyst films exhibited high catalytic activity toward the HER, even better than that observed for electrodeposited Ni–Mo coatings. Representative alkaline HER j–E data for Ni–Mo nanopowder, as well as Ni and Ti foils and Ni nanopowder synthesized by essentially the same route, are shown in Figure 2.14. Clearly introducing nanoscale features to pure Ni increased the catalytic activity of pure Ni by a significant margin; but incorporation of Mo to generate nanostructured Ni–Mo further increased the catalytic activity such that relatively low mass loadings achieved current densities comparable to those desired for an operating Si photocathode (tens of mA cm^{-2}) at $\eta \approx 100$ mV.

The ability to synthesize Ni–Mo nanopowders independently of a substrate al-

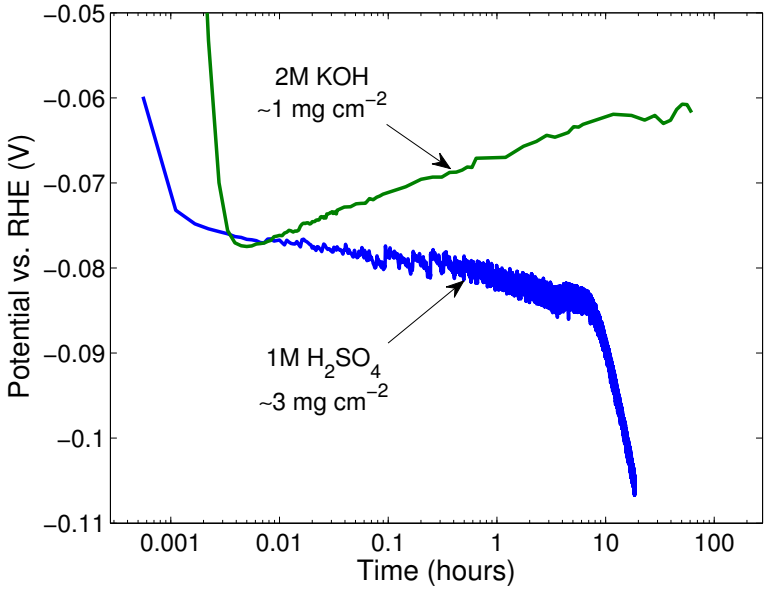

Figure 2.15. Galvanostatic E–t data for Ni–Mo nanopowder films on Ti substrates poised at -20 mA cm^{-2}. Electrolytes and mass loadings were as noted. Alkaline measurements were carried out in a single chamber cell using a Ni counter electrode and a Hg/HgO reference. Acid measurements were carried out in a two-chamber cell using a thin-film Ru/Ir oxide counter electrode separated from the working compartment by a Nafion membrane and an acidic $Hg/HgSO_4$ reference electrode. From McKone et al.[51] Copyright 2013 the American Chemical Society; used with permission.

lowed for much more rigorous analysis of activity and stability than was possible for electrodeposited coatings. Figure 2.15 shows the long-term HER stability of two Ni–Mo coatings from the same synthetic batch under alkaline and acidic conditions, respectively. Clearly the stability of the Ni–Mo catalyst film was quite good under alkaline conditions, actually giving a slight decrease in required η to maintain a constant j over the course of $\sim$100 hours. The sample tested under acidic conditions, however, showed a slow, continuous decrease in activity over approximately 10 hours followed by a precipitous decrease. We ascribe this behavior to continuous corrosion of the Ni–Mo particles, which resulted initially in a slow decrease in activity as the active surface area diminished. After a sufficient interval, the particles dissolved (or changed in composition) to the extent that they could no longer sustain catalysis, giving rapid loss in activity.

The Ni–Mo nanopowder synthesis also allowed us to control the composition of

catalyst materials over a wide range. Figure 2.16 shows the relationship between the initial composition of the ammoniacal Ni/Mo solutions compared with the resulting bulk elemental compositions of the catalyst powders (as determined by EDS) along with their relative catalytic activities under alkaline conditions. Interestingly, solutions with Mo content <40 mol% gave powders similar in bulk composition to the starting solutions, but solutions with initial Mo content >40 mol% gave powders enriched in Ni relative to the starting solution.

The maximum observed Mo content for powders obtained from any mixed starting material (i.e., other than a pure Mo sample) was ∼57%, which agrees remarkably well with the composition reported by Levin et al. for their most Mo-rich ammonium nickel molybdate.[94] Therefore, we believe that all of the Mo content in the intermediate Ni–Mo oxide formed by our synthetic approach precipitates as the compound reported by Levin et al. Additional Ni apparently can be incorporated compared to the stable mixed compound by coprecipitaton of Ni oxide/hydroxide, but additional Mo does not precipitate.

Another interesting feature of the observed catalytic activities for Ni–Mo nanopowders is the large bulk composition range, approximately 15–45 mol% Mo, that gave near the maximum observed catalytic activity. This weak dependence was observed also by Brown and Mahmood[67] and might indicate that formation of the operative catalytic species does not depend strongly on the bulk composition, but merely requires any finely divided mixture containing sufficient quantities of Ni and Mo. Due to this relatively weak relationship between composition and activity, we used Ni–Mo nanopowders from precursor solutions containing 40 mol% Mo for all HER experiments, unless otherwise noted.

The flexibility in deposition of Ni–Mo nanopowder allowed us to carefully assess the relationship between mass loading and catalytic activity. The alkaline HER Tafel behaviors of a series of Ni–Mo coatings deposited with varying mass loadings onto Ti foils are shown in Figure 2.17. Increased mass loading resulted, unsurprisingly, in a monotonic increase in catalytic activity. However, the increase in activity was not consistent with a simple increase in j_0, as would be expected for merely increasing the

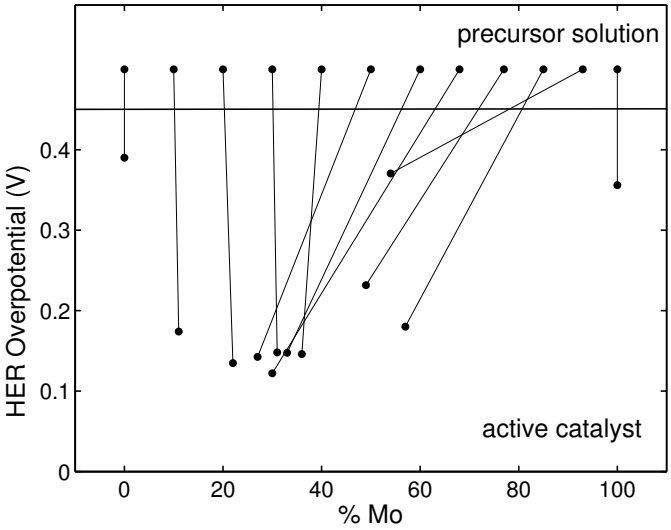

Figure 2.16. Plot illustrating the relationship between the composition of Ni–Mo precursor solutions compared to the resulting bulk composotions and activities of the associted nanopowders. Points above the horizontal line refer to the Mo content (in mol%) in the precursor solutions. Points below the vertical line correspond to the Mo content (in mol%) in the final Ni–Mo nanopowders, as measured by EDS analysis, and the overpotential required to reach $j = -10$ mA cm^{-2} in 1 M NaOH solution. Lines connect the respective precursor solutions to their respective nanopowder results. All films were deposited on Ti substrates with a mass loading of $\sim$0.4 mg cm^{-2} and HER behavior was measured as noted in Figure 2.14. From McKone et al.[51] Copyright 2013 the American Chemical Society; used with permission.

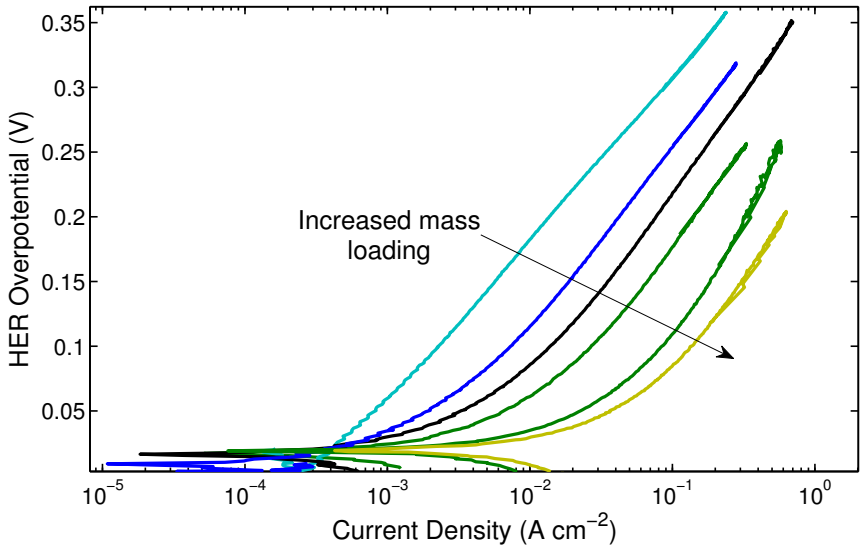

Figure 2.17. Tafel data for Ni–Mo nanopowders deposited onto Ti substrates with various mass loadings. Data were collected in alkaline solution under the conditions noted in Figure 2.14, Mass loadings ranged from <0.1 to ∼13 mg cm^{-2} for the leftmost and rightmost curves, respectively.

total catalyst surface area. Rather, Ni–Mo nanopowders with higher mass loadings also increasingly diverged from linear Tafel behavior at low overpotentials.

The non-linear regions in the Ni–Mo nanopowder Tafel data indicate that the kinetics of the HER at high mass loadings and low overpotentials are not adequately described by the Tafel law, which assumes a single operative mechanism and a negligibly small rate for the electrochemical back reaction.[96] Instead, the behavior is qualitatively consistent with Butler-Volmer kinetics, wherein an oxidation reaction proceeds at a significant rate compared to the observed net reduction reaction, resulting in non-linear $\log(j)$–E behavior.

It is possible that the oxidation contributing to the non-linear Tafel behavior is not the microscopic reverse of the HER (i.e., hydrogen oxidation) but rather a metal-centered oxidation. Figure 2.18, for example, shows cyclic voltammograms for Ni and Ni–Mo nanopowder films around the RHE potential in H_2-saturated alkaline solution. The hysteresis loop that appears in the case of Ni–Mo, but not for Ni, is remeniscient of a capacitive feature. This sort of capacitance is known to occur for Mo oxides,[97,98] and involves changes in redox state at the metal center. Conway

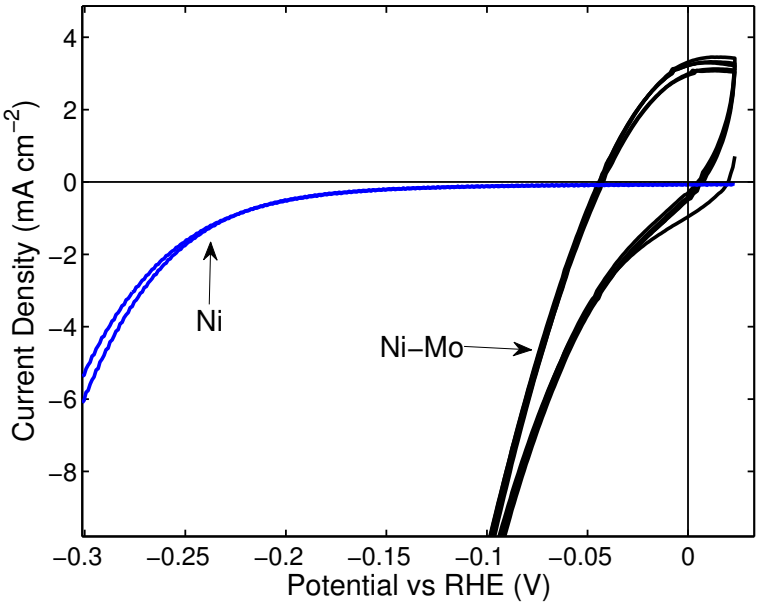

Figure 2.18. Cyclic voltammograms of Ni and Ni–Mo nanopowders in a H_2-saturated 1 M NaOH solution. Catalysts were synthesized by the precipitation-reduction method and deposited onto Ti substrates. Data were collected at a sweep rate of 20 mV sec^{-1} in a single chamber electrochemical cell using a Ni counter electrode and Hg/HgO reference electrode.

also reported that the enhanced activity of Ni–Mo materials over pure Ni might be due to surface hydrides or pseudo-capacitive effects.[70–72,99] Given these possibilities, the operative catalytic mechanism for Ni–Mo materials at low overpotentials likely is more complex than the canonical mechanisms generally ascribed to heterogeneous HER catalysts (see Appendix B). We did not pursue mechanistic aspects of Ni–Mo HER catalysis further, but more work toward elucidating the operative catalytic mechanism would be interesting and useful.

Compiled results for mass-specific alkaline HER activity for Ni–Mo nanopowder at two different overpotentials are shown in Figure 2.19. In particular the mass loading required to obtain $|j| = 10$–20 mA cm^{-2}, the approximate operating j for an efficient solar photocathode, was appoximately 1–2 mg cm^{-2} at $\eta = 100$ mV. Assuming that Ni–Mo nanopowder is metallic and exhibits a lattice constant comparable to pure Ni metal, and estimating a volumetric void fraction of $\sim$70%, this mass loading would result in a catalyst thickness of $\sim$4–8 μm on a planar substrate.

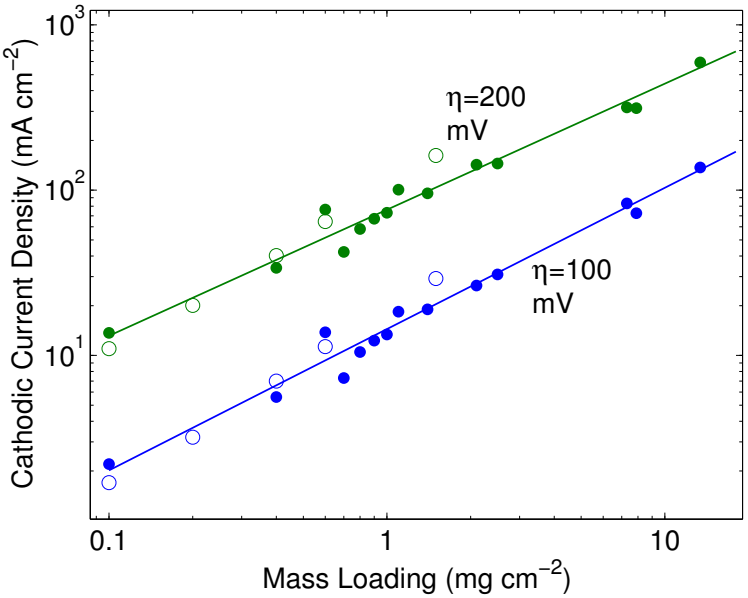

Figure 2.19. Log-log plot showing the relationship between mass loading and current density at the noted overpotentials for Ni–Mo nanopowders on Ti substrates under alkaline conditions. Data were collected from Tafel measurements, as in Figure 2.17. Open and closed circles correspond to two different synthetic batches. Lines correspond to power law least-squares fits for the $\eta = 100$ and 200 mV datasets. From McKone et al.[51] Copyright 2013 the American Chemical Society; used with permission.

The observed dependence of j on Ni–Mo mass loading follows a power law of the form $j \propto m^D$ where j and m are the current density and mass loading, respectively, and D is the power law constant. For $\eta = 100$ and 200 mV, respectively, we found D to be 0.85 and 0.76. We consider this power law dependence to be indicative of "diminished returns" experienced when increasing the mass loading of catalyst, brought about by attenuated mass transport to lower layers of catalyst when additional layers are added. According to this interpretation, we would expect the D factor to increase toward unity (i.e., linearly increasing current density with mass loading) for very low mass loadings and current densities, and to decrease toward zero (i.e., no increased current density with mass loading) for very high current densities and mass loadings.

A detailed understanding of mass-specific catalyst activity as well as catalyst morphology allowed us to make a simple estimation of the per-atom turnover frequency (TOF) of Ni–Mo nanopowder at various overpotentials. This estimate, however, required a series of approximations. First we used the lowest measured mass loading of 0.1 mg cm^{-2}, and assumed that this mass loading was sufficiently low that it could be extrapolated linearly to a single active site. Next, using the TEM results we approximated the particles as an ensemble of spheres 5 nm in diameter, with a bulk density equal to the weighted average density of Ni and Mo in a 3/2 ratio (9.5 g cm^{-3}). Based on these parameters, the surface area of a 0.1 mg sample was $\sim$120 cm^2. Then using the weighted average lattice constant of a 3/2 ratio of Ni and Mo, we determined that the total number of surface atoms in the same 0.1 mg sample was $\sim 2.3 \times 10^{17}$ atoms. Finally, using the known current densities at η =100 and 200 mV, we calculated TOF values of $\sim$0.05 and $\sim$0.36 s^{-1} per surface atom, respectively. All of the aformentioned approximations were taken as conservative estimates so that the calculated values likely underestimated the actual TOF.

To verify the approximation of TOF for Ni–Mo nanopowders, we procured bulk metallurgical samples of Ni–Mo alloys with compositions ranging from 0 to 12 mol% Mo. We then carefully diced, polished, and etched these samples so as to produce damage-free surfaces with a low degree of roughness. A scanning electron micrograph of one such metallurgical sample is shown in Figure 2.20, along with HER j–E results

for the full range of compositions.

Whereas previous researchers observed only a weak relationship between Mo content and catalytic activity for metallurgical Ni–Mo samples,[82,83,85] we observed a clear monotonic increase in activity with increased Mo content. The increase in activity between 4% and 12% Mo was much greater than that between 1% and 4% Mo. This is consistent with our results for nanopowders, shown in Figure 2.16, where the majority of the increase in catalytic activity for Ni–Mo occured between 0% and 10% Mo.

Using similar approximations as in the nanopowder case, along with an assumed roughness factor $\gamma = 1$, we calculated TOFs of $\sim$0.19 and $\sim$0.73 s^{-1} for the 12% Mo metallurgical Ni–Mo sample at $\eta = 100$ and 200 mV, respectively. These results are of the same order of magnitude as those calculated for nanopowders. It is also likely that the γ value for the metallurgical samples was somewhat higher than 1, further suggesting that the measurements agree. Thus some of the enhanced activity of Ni–Mo compared to pure Ni nanopowders can be attributed to increased fundamental catalytic activity obtained by atomic or nanoscale mixing of Ni with Mo.

To summarize, the high observed activity of Ni–Mo is largely due to increased surface area for nanostructured Ni–Mo materials. However, a portion of the increased activity is also due to an inherently higher activity for Ni–Mo on a per-atom basis compared to pure Ni. Additionally, there exists a wide range of compositions over which Ni–Mo HER activity is essentially maximized, suggesting that the catalyst surface composition, which is the relevant parameter for catalysis, may not resemble the composition of the bulk. Finally, the activity of high surface area Ni–Mo nanopowders does not fit well to the Tafel law at low overpontials, suggesting that a more complex mechanism, perhaps involving Mo redox cycling, might be operative under conditions that are relevant for PEC hydrogen evolution.

Looking forward, we believe that the catalytic activities of Ni–Mo nanopowders can be further improved by tuning the synthetic procedure to give smaller or more porous catalysts, resulting in higher surface areas per mass. Additionally, increased activity might be possible with addition of a third elemental component, as has been

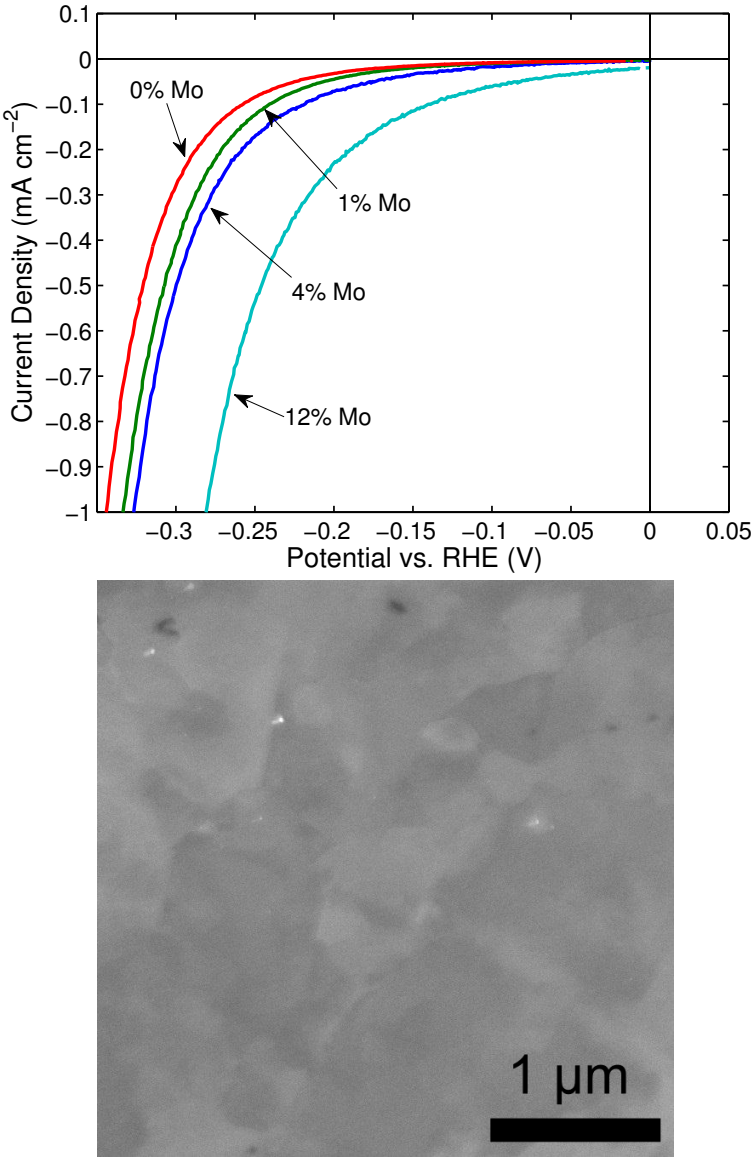

Figure 2.20. Top: HER j–E data for polished and etched metallurgical Ni–Mo samples under the same conditions as noted in Figure 2.14. Bottom: scanning electron micrograph of a metallurgical Ni–Mo sample containing 4 mol% Mo after polishing and etching. From McKone et al.[51] Copyright 2013 the American Chemical Society; used with permission.

demonstrated previously with Cd.[69] The fundamental mechanism of Ni–Mo HER electrocatalysis could also be probed using various in situ or in operando spectroscopic probes, such as Raman spectroscopy and photoelectron spectroscopy. Elucidation of the fundamental mechanistic behavior of Ni–Mo catalysts is a worthwhile goal, in that it may allow for generation of significantly more active HER catalysts in the future. Ni–Mo nanopowders as well as metallurgical samples are particularly useful candidates for further study.

2.6 Ni_2P Nanoparticles

Early in 2012, Raymond (Ray) Schaak joined the CCI Solar effort as a new principal investigator. Soon thereafter we initiated a collaboration intended to leverage the nanomaterials synthesis capabilities of the Schaak group with the electrochemistry experience of the Lewis and Gray groups. In less than a year, this collaboration resulted in fruitful results regarding a promising new HER catalyst, Ni_2P.

Early in 2012, Ray sent two graduate students, Eric Popczun and Matthew Buck, to Caltech to work with me on electrochemical characterization of several types of nanoparticles that the Schaak group had already been synthesizing.[100] We collected HER activity data under alkaline conditions for a series of transition metal sulfides and selenides deposited by drop-casting onto Ti substrates. Results for nanoparticle films that showed significant HER activity above the Ti foil background are shown in Figure 2.21.

Although several Co sulfides gave several orders of magnitude higher HER activity than the Ti substrate, this was still several orders lower in activity than Ni–Mo nanopowders with the same mass loading. We did not pursue these catalyst materials any further. Nevertheless, the collaboration demonstrated that materials synthesized by methods used in the Schaak group could be active electrocatalysts.

Out of our initial efforts grew a hypothesis that nickel phosphides might be promising HER electrocatalysts. Based on previous literature precedent for MoS_2,[64,101–105] Nate and Ray suggested that the hydrogen evolution and hydrodesulfurization (HDS)

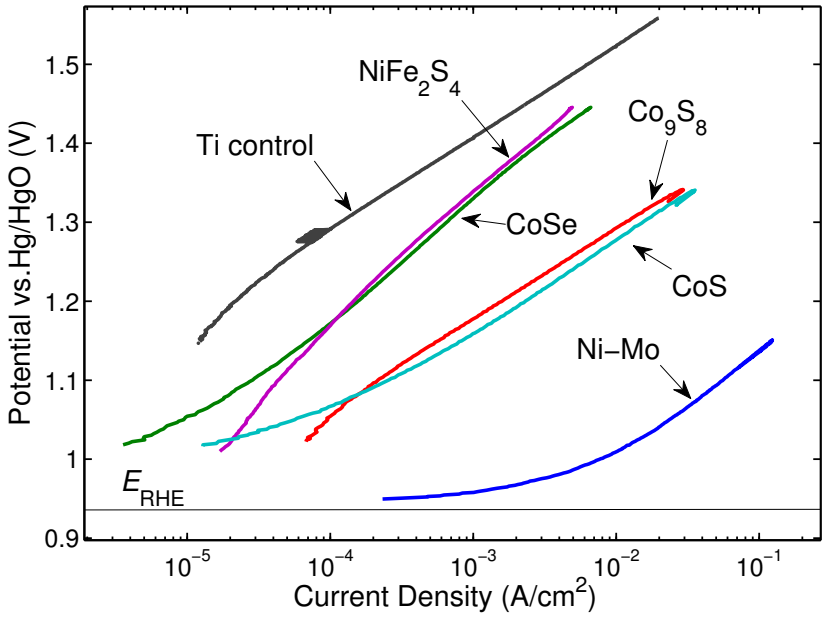

Figure 2.21. Tafel plot showing the HER activity of several transition metal sulfide and selenide particles from the library of materials available from the Schaak group. Experiments were carried out in 1 M KOH solution under the same conditions as in Figure 2.14, and catalyst mass loadings were 0.6 mg cm^{-2}.

processes generally share common hydride intermediates. As such, essentially all materials that are known to be active HDS catalysts might also be active HER catalysts.

The Ni_2P phase of nickel phosphide is a known active HDS catalyst.[106,107] Amorphous mixtures of nickel and phosphorus have been shown to give enhanced HER activity compared to pure Ni under alkaline conditions.[108,109] Additionally, Liu and Rodriguez predicted on the basis of DFT calculations that crystalline Ni_2P should be an active HER electrocatalyst,[110] but this prediction had not yet been addressed experimentally.

Eric Popczun adopted a previously reported synthesis of monodisperse nanoparticles of Ni_2P by a homogeneous solution phase route.[111,112] Results of various analyses confirming the monodispersity, crystallinity, and phase purity of the product particles are shown in Figure 2.22. Samples of these particles were purified, dried, and sent to me for HER experimentation.

I prepared electrodes consisting of Ni_2P on Ti substrates by resuspending the

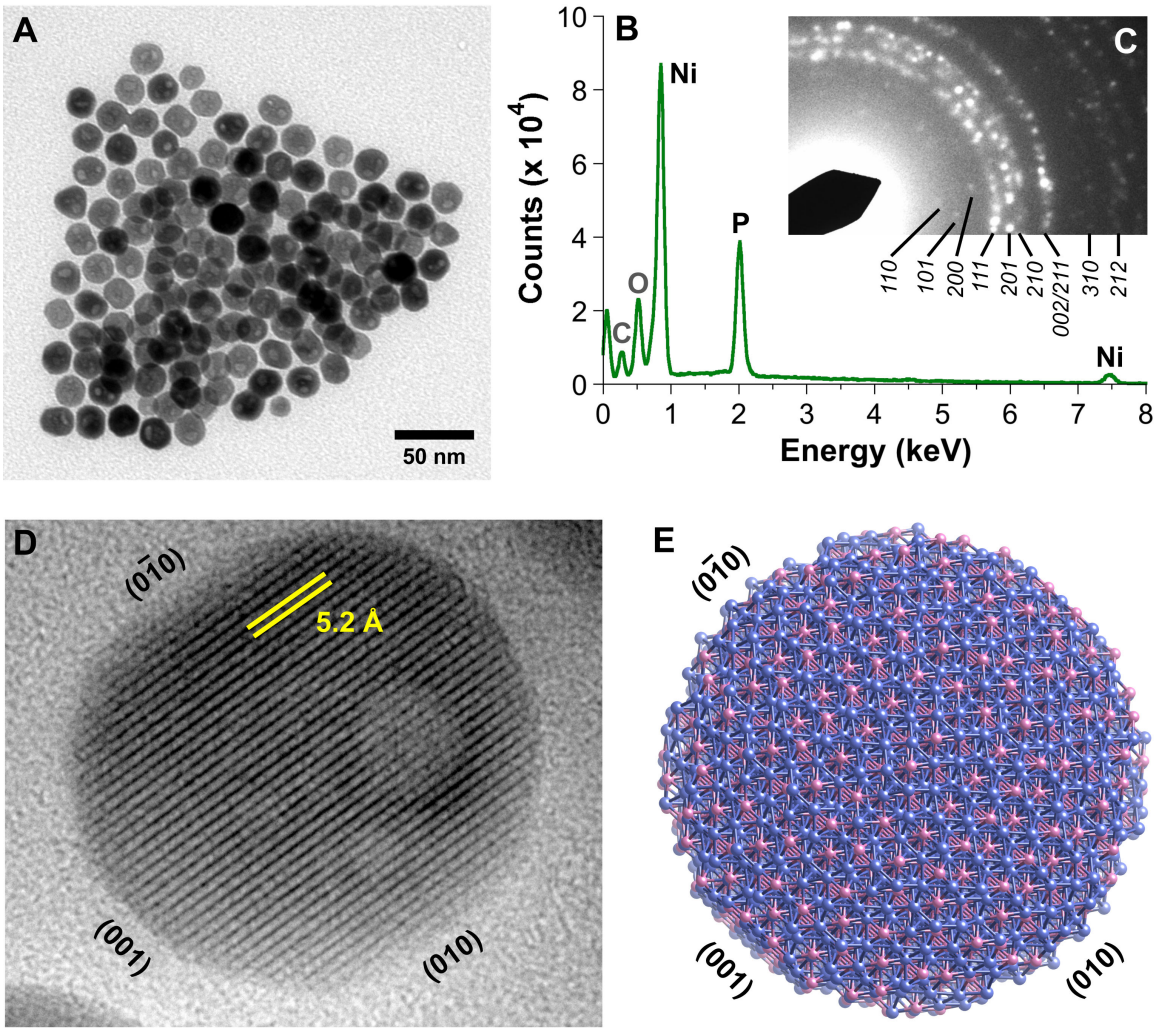

Figure 2.22. Collected synthetic data for Ni_2P nanoparticles, from the Schaak lab: (A) transmission electron micrograph of the as-synthesized particles; (B–C) EDS and electron diffraction data confirming formation of crystalline Ni_2P; (D) high-resolution TEM image of a single Ni_2P particle, showing preferential exposure of the (001) and (010) planes; (E) atomic model of the lattice structured implied from (D). From Popczun et al.[52] Used with permission.

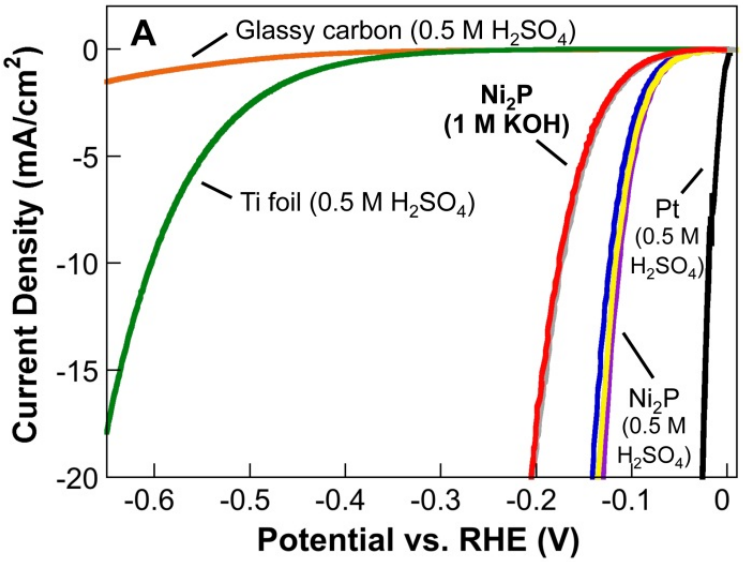

Figure 2.23. Pseudo-steady state HER j–E data for Ni_2P nanoparticle films deposited at $\sim$1 mg cm^{-2} mass loadings on Ti foils, along with the relevant controls. Acid data were collected in a two-compartment cell using a Ru/Ir oxide counter electrode separated by a Nafion membrane and a Ag/AgCl reference electrode in the working compartment. Alkaline data were collected in a single-compartment cell using a Ni mesh counter electrode and a Hg/HgO reference. All solutions were saturated with H_2. Contact and solution resistances were compensated using the current-interrupt technique. From Popczun et al.[52] Used with permission.

particles in hexanes and drop-casting onto Ti foils. After annealing for 1 hour at 450 °C under forming gas, the resulting catalyst films exhibited high activity and good stability toward the HER under both acidic and alkaline conditions. Representative data for Ni_2P HER activity in acid and base are shown in Figure 2.23. Eric also showed, using infrared spectroscopy, that the annealing step removes the organic solubilizing agent from the particle surfaces, as demonstrated in Figure 2.24, allowing for direct access of reactants to the clean catalyst surface.

The most notable property of the Ni_2P particles, however, is their high stability toward corrosion in aqueous acidic solution. Figure 2.25 shows a set of accelerated degradations studies, consisting of consecutive CV sweeps ranging from approximately +0.2 to −0.2 V vs. RHE in 0.5 M H_2SO_4 solution. Remarkably, the catalyst films retained very high HER activity even after 500 CV sweeps. Under similar conditions, Ni–Mo catalysts are rapidly oxidized and stripped from an electrode surface, as shown

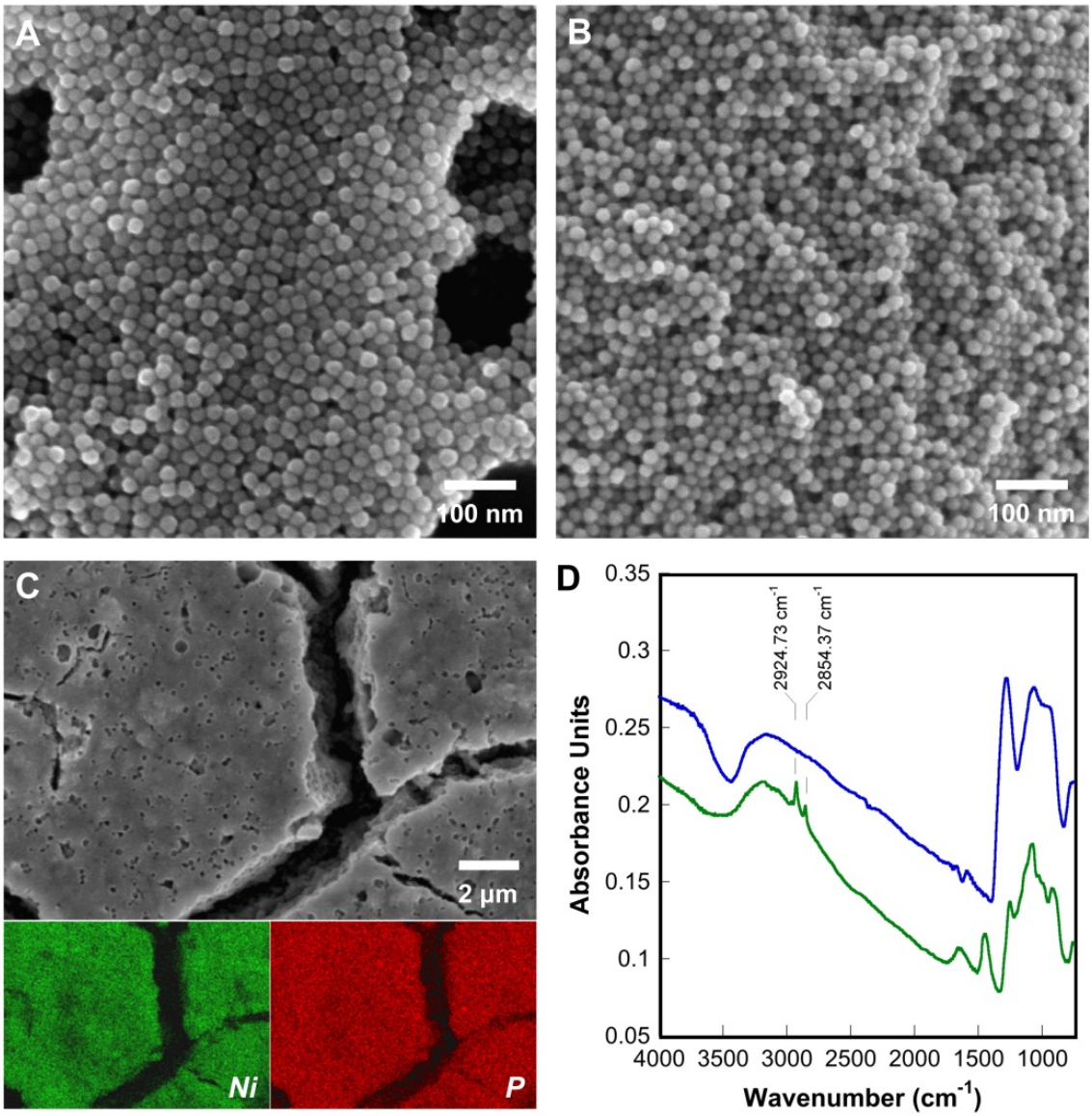

Figure 2.24. Collected data from Ni_2P annealing and spectroscopy studies: (A–B) scanning electron micrographs of Ni_2P films before and after annealing at 450 °C under forming gas, respectively; (C) large-area scanning electron micrograph of a Ni_2P film along with an EDS elemental map of Ni and P; (D) diffuse reflectance infrared Fourier transform spectroscopy (DRIFTS) data from Ni_2P films before (green, below) and after (blue, above) annealing. From Popczun et al.[52] Used with permission.

in Figure 2.5.

Undoubtedly, Ni_2P is a very promising new earth-abundant HER electrocatalyst, and illustrates that non-noble transition metal catalysts can be stable under acidic conditions. MoS_2 and Ni–Mo nitrides have also been shown to exhibit high stability under acidic conditions,[113,114] attesting perhaps to the generality of stabilizing non-noble HER catalysts by incorporation of heteroatoms such as C, N, P, or S. Both of these material sets, and other related nanoparticulate compounds, certainly deserve to be explored further with respect to their activity and stability, as well as for potential incorporation into HER photocathodes.

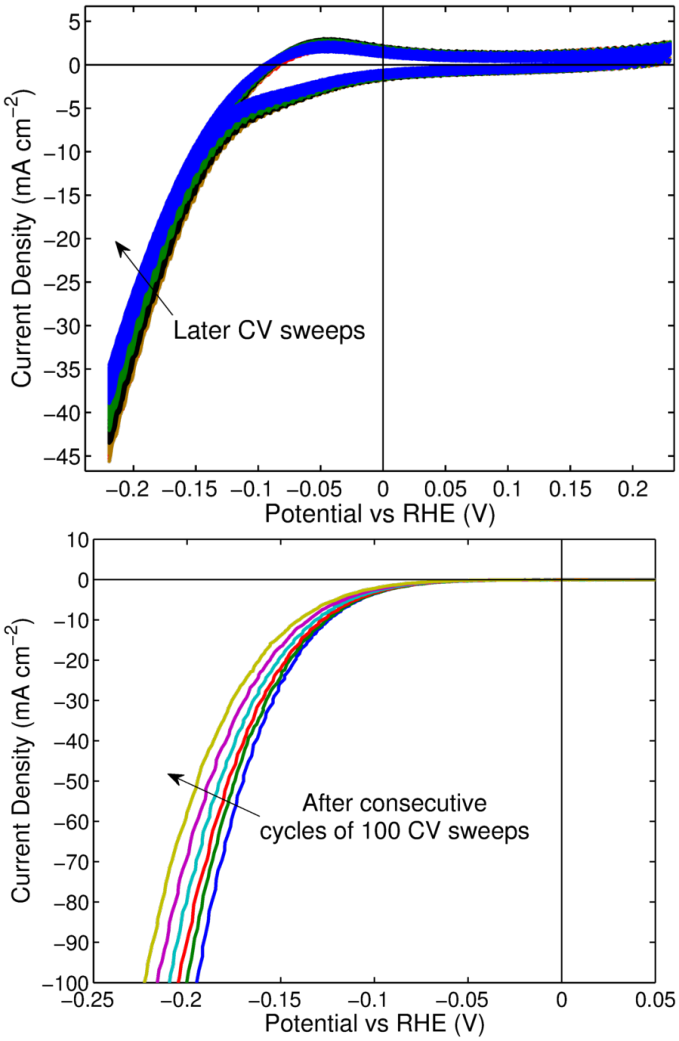

Figure 2.25. Electrochemical stability data for a Ni_2P film on a Ti substrate in 0.5 M H_2SO_4 solution. Top: 500 consecutive CV cycles at 100 mV sec^{-1}, colored in 100-sweep intervals, of the film from +0.22 to -0.23 V vs. RHE. Bottom: Pseudo-steady state HER j–E data for the same film between each set of 100 CV cycles. Data were collected under the same conditions as the acid data in Figure 2.23.

Chapter 3

Silicon Hydrogen-Evolving Photocathodes

3.1 Introduction and Background

This chapter describes work on characterising Si composite photocathodes with Ni, Ni–Mo, and Pt electrocatalysts. Most of the work herein was accomplished close collaboartion with Emily Warren. Emily was broadly responsible for development of Si microwire light absorbers. Details on synthesis and characterization of microwires are available in the published literature and in Emily's dissertation.[36,115,116] I was responsible for development of the catalyst components of Si hydrogen evolving photocathodes; therefore the emphasis of this chapter is on work involving catalysts.

Emily and I extensively characterized the behavior of electrodeposited Ni and Ni–Mo on p-Si substrates in both planar and microwire geometries. We also compared the resulting hydrogen evolution behavior to the performance obtainable by depositing Pt onto p-Si by a wet chemical (electroless) method as well as by e-beam evaporation. We further optimized depositions of Ni–Mo and Pt onto Si microwires that had been processed into n^+p homojunctions in attempts to demonstrate high energy conversion efficiencies for PEC hydrogen evolution.

Over the course of our experiments of catalysts on Si, we identified several important limitations for use of both non-noble and Pt catalysts on p-Si, which are described herein. I also describe a method to circumvent some of these limitations

through a new device design that takes advantage of the deposition flexibility afforded by Ni–Mo nanopowder.

The vast majority of previous work on semiconductor-metal composite photocathodes for driving the HER under illumination incorporated noble metals as the cocatalyst. The Wrighton group used Pt catalysts to generate hydrogen-evolving photocathodes based on WS_2 and p-Si.[117–119] The Texas Instruments company also used Pt catalysts for the hydrogen evolution half reaction in their solar energy storage system that accomplished net HBr splitting instead of water splitting.[25,120] More recently, earth-abundant MoS_2 catalysts have also been applied to p-Si light absorbers for photoelectrochemical hydrogen generation,[102,121] but conversion efficiencies for these systems remain low.

The most well-known example of PEC hydrogen evolution using a p-type semiconductor is the work by Heller and coworkers on InP photocathodes.[122,123] They reported in a series of papers that very high energy conversion efficiencies could be obtained when p-InP was coated with a thin layer of discontinuous, nanoparticulate noble metal catalysts such as Pt, Pd, Ru, and Rh. Furthermore, Heller et al. found that their semiconductor-catalyst composite electrodes exhibited high light absorption in spite of the high fractional coverage of metal films on their surfaces.[124–126]

Shannon Boettcher, a Lewis group postdoc, benchmarked the performance of Si n^+p-junctions deposited with Pt cocatalysts for the HER under illumination. He was able to generate both planar and microwire array composite photocathodes, and both gave large photovoltages and fast kinetics for the HER under solar-simulated conditions, as shown in Figure 3.1.[46] Emily and I expanded significantly on this initial work by undertaking a more elaborate study on the PEC hydrogen evolution properties of several catalysts on Si electrodes of various types.[49,50]

3.2 Deposition and Characterization

We found that the same electrodeposition of Ni and Ni–Mo sulfamate electrodeposition solutions as were used for degenerate Si and other substrates were also amenable

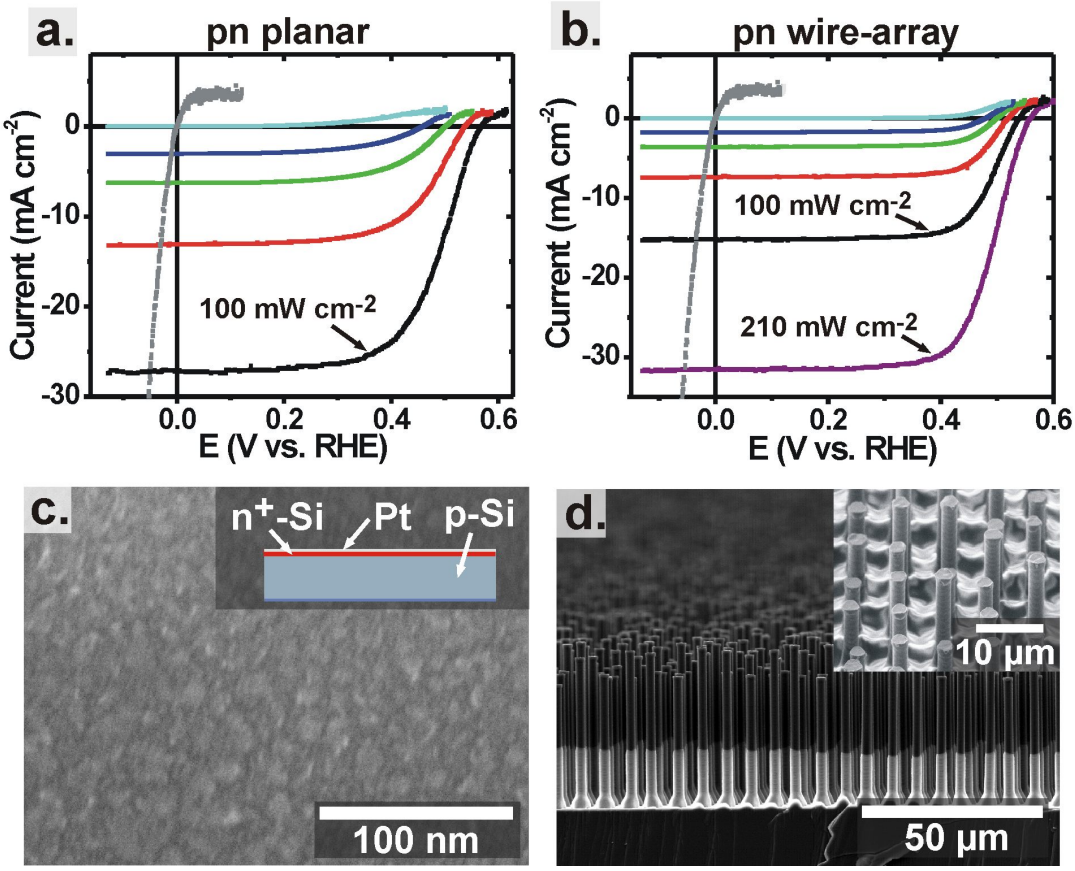

Figure 3.1. Photoelectrochemical HER performance (a–b) and micrographs (c–d) for planar and microwire Si n^+p-junction photocathodes coated with Pt catalyst in 0.5 M H_2SO_4 solution. From Boettcher et al.[46] Copyright 2011 the American Chemical Society; used with permission.

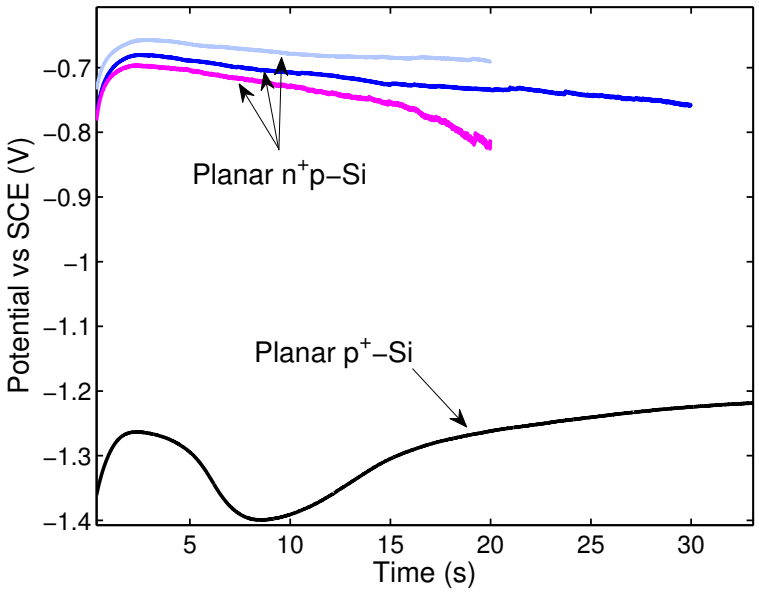

Figure 3.2. Potential vs. time data for galvanostatic electrodeposition at −20 mA cm^{-2} of Ni–Mo alloy from sulfamate solution onto the noted substrates. Depositions used a nickel foil counter electrode, and the n^+p-Si electrodes were intensely illuminated with a tungsten-halogen light source.

for deposition on photoactive Si electrodes. However, since cathodic current represents transfer of minority carriers across the interface of a p-type semiconductor, both p-Si and n^+p-Si photoelectrodes needed to be illuminated in order to allow for photoexcited minority carriers to faciliate deposition. Since the deposition solution was deep green in color, we illuminated the Si surface as intensely as possible by placing a tungsten halogen light source immediately adjacent to the deposition cell.

Figure 3.2 illustrates a deposition of Ni–Mo onto a planar p^+-Si substrate compared to several n^+p-Si homojunction substrates, where the latter were placed under intense illumination. Under galvanostatic deposition conditions, the voltage required to pass mA cm^{-2} across the semiconductor-electrolyte interface was shifted by >500 mV in the positive direction on planar n^+p-junction electrodes compared to p^+-Si electrodes. This shift represents the photovoltage of the diode formed by the homojunction.

On planar p-Si electrodes, we found that galvanostatic depositions of Ni and Ni–Mo from sulfamate solution at −20 mA cm^{-2}, exactly as with the "dark" electrode

depositions, was the best approach. For microwires, Ni–Mo depositions required significantly higher current densities to obtain active catalysts. We found the best method for Ni–Mo deposition on p-Si microwire substrates was to deposit under galvanostatic conditions at -50 mA cm^{-2}, or under potentiostatic conditions at a potential sufficiently negative to result in cathodic current densities of 50–100 mA cm^{-2}.

Platinum deposition was carried out by an electroless method from H_2PtCl_6/HF solution or using e-beam evaporation. Electroless Pt proceeds as in Equations 3.1 and 3.2:

$$H_2PtCl_6 + Si_0 + 2\,H_2O \longrightarrow Pt_0 + SiO_2 + 6\,HCl \tag{3.1}$$

$$SiO_2 + 6\,HF \longrightarrow H_2SiF_6 + 2\,H_2O \tag{3.2}$$

where Pt(IV) reacts with Si to generate Pt metal and Si oxide. The Si oxide is subsequently etched by HF to give a clean Si surface so that the Pt deposition may continue.[127]

Deposition of catalysts onto Si photoelectrodes always resulted in dimished photocurrents as a result of blocking incoming photons with the catalyst overlayer. In extreme cases light blocking by the catalyst during deposition resulted in such a large attenution of the incoming light flux that the semiconductor could no longer support sufficient current flow to sustain further catalyst deposition. Under potentiostatic conditions, this resulted in halting of the deposition; but under galvanostatic conditions, light attenuation eventually caused the potentiostat to apply a very negative potential in order to "break down" the diode to supply the required current. In such cases we generally found that the photoelectrode energy conversion properties were badly degraded.

Due to light blocking by the catalyst layer, depositions on Si electrodes had to be optimized so as to give substantially improved catalytic onset of hydrogen evolution but minimize the attentuation of light absorption. Figure 3.3 depicts optimized j–

E profiles for planar and microwire p-Si photoelectrodes deposited with the various catalysts. Generally nickel depositions required only on the order of 1 second or less of deposition time at -20 mA cm^{-2}, whereas optimized Ni–Mo films required tens of seconds. The electroless Pt deposition gave the best results of all the catalysts on p-Si, and performance was optimized after 4–5 minutes total of electroless deposition time, usually carried out in 1-minute increments.

Several characteristics of the optimized j–E behavior of p-Si composite photoelectrodes were immediately apparent. First, the photovoltages of all the photoelectrodes were quite low—on the order of 100–300 mV compared to 500–600 mV photovoltages that can be obtained with Si p-n homojunctions or p-Si in contact with a highly reducing redox couple such as methyl viologen. These low photovoltages were likely due to poor band alignment between Si and its contacts. The formal potential of the HER lies approximately in the center of the Si bandgap, resulting in a relatively small built-in potential ϕ_{bi} (i.e., a weak field in the space-charge region) and low photovoltages. The contacts between Si and Ni, Ni–Mo, or Pt also give very small ϕ_{bi} values due to poor band alignment with the work functions of the constituent metals.

Another key feature of the optimized j–E behavior of p-Si photoelectrodes was the relatively low observed photocurrents, especially in the case of the microwire electrodes. Planar Si devices can generate j_{ph} as high as 30–35 mA cm^{-2} without the use of an antireflection coating, whereas our devices only gave up to $\sim$25 mA cm^{-2} for Pt cocatalysts and $\sim$20 mA cm^{-2} for Ni and Ni–Mo catalysts. These diminished photocurrents resulted directly from light blocking by the catalyst layer. The microwires gave lower photocurrents than the planar samples, which is generally true for microwire arrays due to the significant amount of void space that exists between the sparsely packed wires.[43,44]

The rates of catalytic onset of the HER for the various photoelectrodes varied significantly between catalysts and the substrate morphologies. The cathodic current onsets of all the catalysts were faster on microwires than on planar substrates. This was likely due to the increased active catalyst surface area exposed on the high aspect-ratio wire arrays, as discussed in Chapter 2. Unsurprisingly, Ni–Mo gave a more

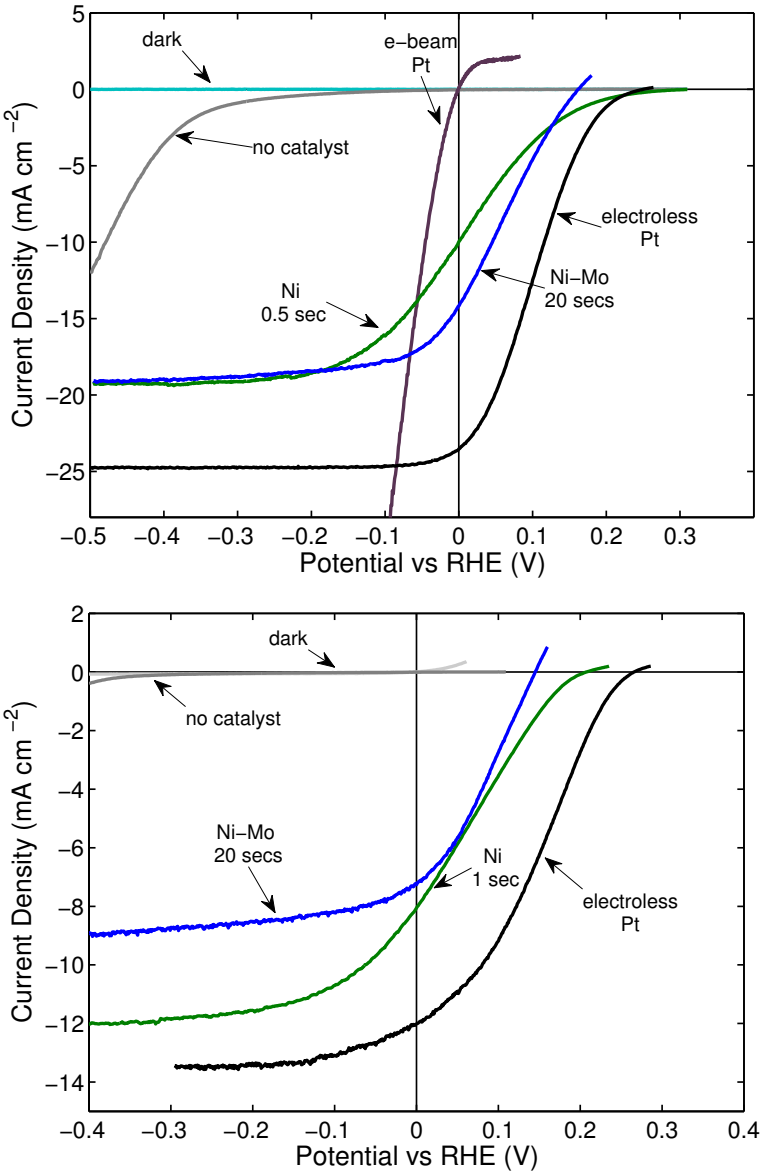

Figure 3.3. PEC hydrogen evolution j–E data for planar (above) and microwire (below) p-Si photocathodes deposited with the noted catalyst films. Ni and Ni–Mo electrodepositions were carried out galvanostatically at -20 and -50 mA cm^{-2} for the noted time intervals. Data were collected in a two-compartment cell using aqueous, H_2-saturated 0.5 M K_2SO_4 solution with 0.2 M KHP buffered to pH 4.5. Counter and reference electrodes were a Pt mesh in a separate fritted compartment, and SCE, respectively. All curves except those labeled "dark" were illuminated using a tungsten-halogen light source at 100 mW cm^{-2} intensity as an approximation of the AM1.5G solar spectrum. From McKone et al.[49] Copyright 2011 the Royal Society of Chemistry; used with permission.

rapid onset of cathodic current density than Ni; but unexpectedly, the onset for the optimized Ni–Mo catalysts also exceeded that of electroless Pt. The optimized Ni–Mo catalyst on p-Si wire arrays, in particular, reached their photocurrent maxima within 150 mV negative of E_{oc}. This rapid onset would have resulted in relatively high fill factors if the photovoltages of the electrodes were increased toward the 500–600 mV that could be obtained in principle from Si photoelectrodes.

The behavior of Pt catalysts deposited onto p-Si photoelectrodes exhibited widely varying behavior depending on the method of deposition and the nature of the Si substrate. Figure 3.4 depicts the range of j–E properties obtained for both electroless and evaporated Pt films on p-Si planar and microwire substrates with degenerate and moderate p-type doping. Notably, evaporated platinum films always resulted in ohmic contact (i.e., no photovoltage), even when deposited onto "photoactive" p-type Si substrates. Electroless depositions gave ∼200 mV photovoltages on p-type Si, but also gave slow catalytic onset behavior compared to evaporated Pt films. Electroless Pt depositions onto p^+-Si planar and microwire substrates also gave markedly slower catalytic onsets compared with evaporated Pt films.

We proposed that the reason for the strange behavior from Pt on Si photoelectrodes was related to inherent electronic properties as well as the interfacial chemistry resulting from different Pt depositions. This hypothesis was strongly supported by X-ray Photoelectron Spectroscopy (XPS) results obtained for the various deposition methods, as shown in Figure 3.5. Evaporated Pt films on freshly etched Si surfaces exhibited interfaces that were completely free of Si oxide. As a result, the deposited Pt formed an ohmic contact to the p-Si either through a direct Si/Pt junction or through formation of a thin interfacial conductive Pt silicide. As a result, the charge transport across this interface was facile and fast catalysis could proceed, but no rectifying barrier was formed.

In the case of electroless Pt deposition, however, the Pt(IV) starting material oxidized the Si surface as it was deposited, resulting in formation of an interfacial Si oxide. The result was attenuated charge transfer across the interface, resulting in diminished apparent catalytic activity. This explains the anomolously low apparent

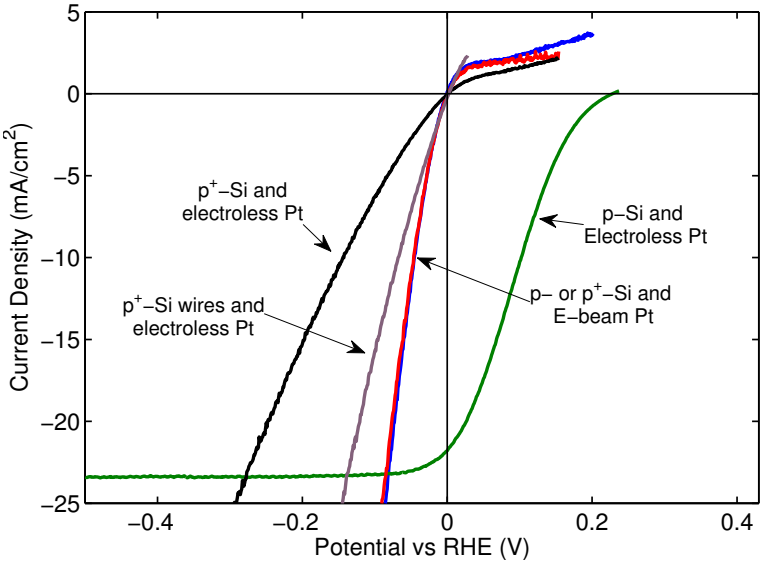

Figure 3.4. Compiled j–E data for hydrogen evolution from Pt films deposited on various types of Si electrodes. All data were collected in aqueous hydrogen-saturated K_2SO_4/KHP solution as in Figure 3.3. Unless otherwise noted, the substrates were planar. The curve labeled "p-Si and Electroless Pt" was collected while the electrode was illuminated with a tungsten-halogen light source at 100 mW cm^{-2}. The others were collected without illumination.

catalytic activity from electroless Pt compared to Ni–Mo on p-Si. However, the same interfacial oxide also allowed for the formation of a rectifying barrier at the Si surface, perhaps due to equilibration of the partially exposed Si surface with the hydrogen couple. Therefore an interfacial oxide is, in fact, deleterious for catatytic activity, but necessary in order to ensure that p-Si electrodes generate photovoltage.

We conclude from these studies of p-Si photoelectrodes with various catalysts that Ni–Mo remains quite promising as a catalyst for use in efficient hydrogen evolution photocathodes, due to its relatively high catalytic activity and, unlike with Pt films, absence of deleterious interfacial behavior. We also conclude that the primary challenges for Si microwire plus Ni–Mo photoelectrodes are the low photovoltages and photocurrents obtained from electrodeposited samples. Therefore we undertook further efforts to increase the photovoltages and photocurrents of Si microwire devices.

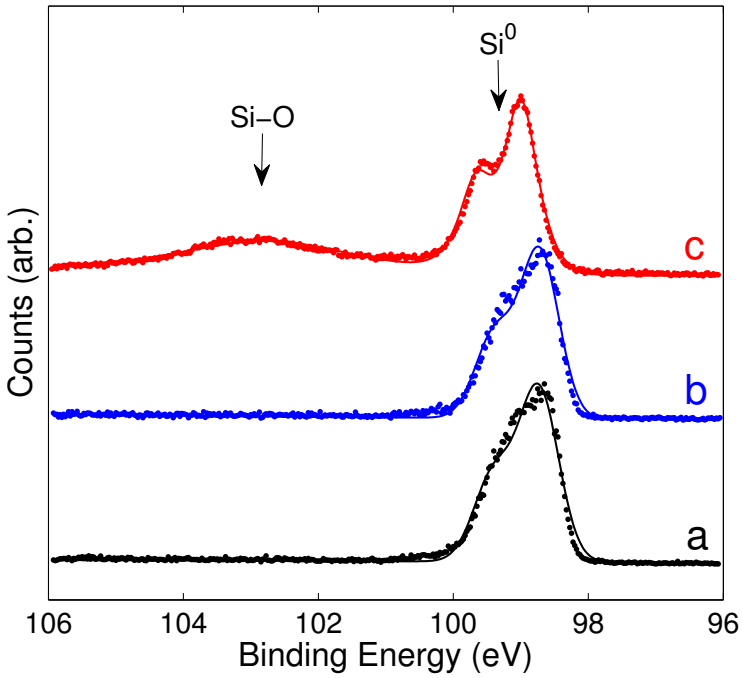

Figure 3.5. X-ray photoelectron spectra of p^+-Si samples deposited with Pt by different methods: (a) control with no Pt deposition; (b) Pt deposited by e-beam evporation; (c) Pt deposited by the electroless method from Pt(IV). All samples were etched with buffered HF immediately before placing them in the vacuum chamber. Only sample (c) exhibited significant Si oxidation in the binding energy range 102–104 eV. From McKone et al.[49] Copyright 2011 the Royal Society of Chemistry; used with permission.

3.3 Si Homojunctions

To ameliorate problem of low photovoltages, we diffused n^+-Si emitters into the outer layers of p-Si microwire arrays using vapor-phase phosphorus precurors, thereby generating n^+p-Si homojunctions.[128] Shannon Boettcher reported that microwire array homojunctions could generate photovoltages in excess of 500 mV for the HER under illumination.[46] We had difficulty producing microwire substrates and doping results that matched Shannon's initial results, but we were able to produce n^+p-microwire arrays with photovoltages of >400 mV.

Additionally, we addressed the challenge of low photocurrents from p-Si microwire arrays by incorporating TiO_2 nanoparticles into a silicone polymer matrix deposited at the bases of the microwires prior to catalyst deposition. This TiO_2 layer was intended to improve photocurrents by latterally scattering photons that passed between the wires, resulting in increased absorption.[43] We also optimized Ni–Mo electrodeposition and Pt evaporation on these composite photocathodes. The best results for Si microwire homojunctions, along with the optimized previous results from p-Si microwires with Ni–Mo and Pt catalysts, are shown in Figure 3.6. The thermodynamically based energy conversion efficiencies (η) for these n^+p-Si electrodes were 2.2% and 3.5% for the Ni–Mo- and Pt-coated samples, respectively.[50]

There were several notable features from Si microwire n^+p-homojunction devices deposited with Ni–Mo catalyst. First, the fill factors remained rather low due to relatively sluggish onset of HER current. Second, the photocurrents also remained rather low, even after incorporation of light scattering elements. Both of these factors stemmed from the same root cause, which was that catalyst deposition still resulted in inevitable loss of absorbed light flux due to blocking.

As a result of parasitic light blocking, the Ni–Mo catalyst could not be deposited with a mass loading sufficiently high to give fast HER onset without also severely diminishing the photocurrent. The effect was smaller in the case of Pt catalyst, because a very small catalyst loading could be used (on the order of a few nm equivalent planar thickness) so that light blocking by the Pt layer was comparatively small

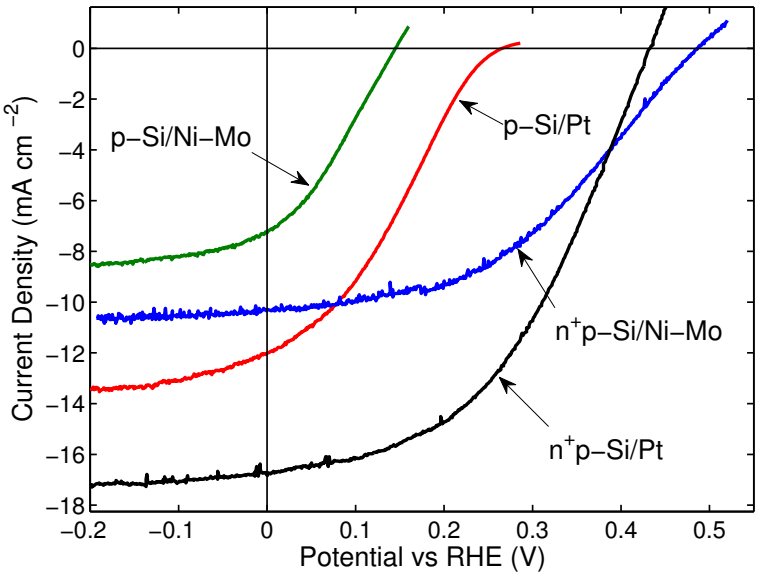

Figure 3.6. Photoelectrochemical hydrogen evolution j–E data for p-Si and n$^+$p-Si microwire arrays deposited with Pt and Ni–Mo under optimized conditions. Cell, electrolyte, and illumination conditions were as in Figure 3.3.

while still retaining high HER activity. Nevertheless, the energy conversion efficiencies for the homojunction microwire devices were significantly improved compared to pure p-Si microwires due to markedly increased photovoltages and slightly increased photocurrents.

We believe that the results depicted in Figure 3.6 represent nearly the best possible compromise between light absorption and activity for Ni–Mo catalysts on Si microwire arrays. The tradeoff between parasitic light absorption and catalytic activity is illustrated even more clearly in Figure 3.7, which shows data for Ni–Mo catalysts deposited at a constant current density (-50 mA cm^{-2}) over two different time periods on a p-Si microwire array. The longer Ni–Mo deposition gave a markedly improved catalytic onset at the expense of attenuating the photocurrent by >50% It is possible that continued development of microwire synthesis and doping strategies could yield increased photovoltages and somewhat higher photocurrents, but it is unlikely that electrodeposited Si/Ni–Mo photocathodes could give η values significantly greater than 5%.

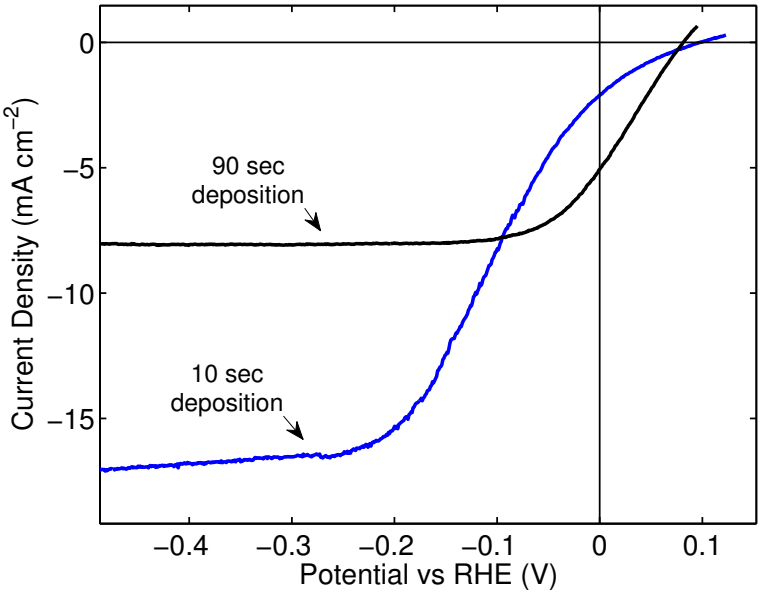

Figure 3.7. HER j–E data for two illuminated p-Si microwire electrodes illustrating of the tradeoff between high catalyst activity and high photoelectrode light absorption. Each was deposited with Ni–Mo from sulfamate solution for the noted time period at -50 mA cm^{-2}. Cell, electrolyte, and illumination conditions were as in Figure 3.3.

3.4 Alternative Design

Excessive parasitic light absorption will be a ubiquitous problem for catalysts deposited uniformly onto a semiconductor photocathode. Optical transparency for a uniform catalyst layer can only be obtained by either using a very low mass loading of optically dense catalyst material, or by using a material with fundamentally high optical transparency.[126,129] Heller showed that noble metals can be deposited with low densities and porous morphologies to allow for optical transparency,[124,125] but non-noble materials are not likely to achieve fundamental (e.g., per-atom) activities comparable to noble metals. Therefore relatively large masses or nominal planar thicknesses (several mg cm^{-2} or μm, respectively) of non-noble catalysts will be needed in order to achieve sufficient catalytic activity to give high energy conversion efficiencies. Also, it is unlikely that HER catalysts with high optical transparency can be generated that allow for significant light penetration when deposited at the required mass loadings.

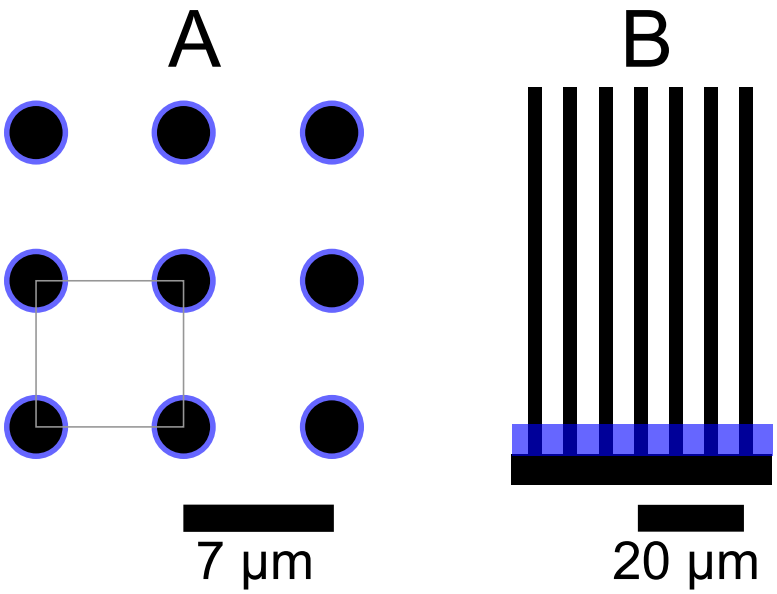

Figure 3.8. Schematic illustrations of two different modes of catalyst deposition onto Si microwires. (A) Top-down view of a square-packed microwire array, with 2.5 μm wire diameters and 7 μm pitch, conformally coated with a 250 nm-thick catalyst layer. One unit cell is contained in the gray square. (B) Side-on view of a microwire array with the same dimensions deposited with 6 μm of catalyst conformally at the base. Assuming the catalyst in (B) is more porous and therefore half as dense as in (A) the total catalyst mass loading per projected area in both cases is equivalent.

The microwire geometry, however, allows for a different approach to photocathode design that is not plausible for a planar geometry, and may allow for the use of high catalyst loadings while still retaining high light absorption in the light absorber component. This approach is outlined schematically in Figure 3.8, and involves selective deposition of a relatively high mass of catalyst at the bases of high aspect ratio structures such as Si microwire arrays. Because of the relatively sparse nature of Si microwire arrays, a conformal catalyst film several hundred nm in thickness around each microwire, which was shown in Chapter 2 to be comparable in HER activity to a planar Pt film, occupies only ∼10% of the total volume of a microwire array. Using this design, it should be possible to achieve Pt-like activity from a relatively high mass of a non-noble catalyst while still retaining optical accessibility of the vast majority of the light absorber component.

Even if placed only at the base of a microwire array, a porous catalyst layer will still absorb essentially all the light that passes through the sparse microwire array.

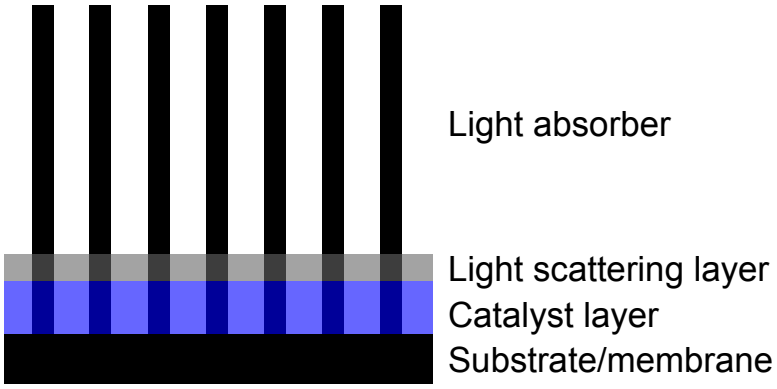

Figure 3.9. Schematic representation of a hydrogen evolving photocathode with the "MEA" device architecture. The base of a high aspect-ratio wire array is deposited with an underlayer of active catalyst material, analogous to an MEA active layer, and an overlayer of light scattering material anlogous to an MEA gas diffusion layer (GDL).

Therefore I proposed the full device structure shown in Figure 3.9, which I call the "MEA" architecture due to its resemblance to a fuel cell or electrolyzer membrane electrode assembly (MEA). It is characterized by a microwire array on the order of 100 μm in height, where the base of the array is deposited with two layers of material. The first layer is a relatively thick (5–10 μm) catalyst layer, consisting of a porous non-noble HER catalyst such as Ni–Mo. The second layer is a relatively thin (1–3 μm) layer of a light scattering material such as particulate TiO_2.

If both layers are made sufficiently porous, reactant species (e.g., water or H_3O^+) can diffuse through and hydrogen gas diffuse out. Photons, however, when incident on the scattering layer, would be reflected laterally and never "see" the highly absorbing catalyst layer. A similar light scattering approach was proposed for Si microwire photovoltaics, and optical models suggested that very high photocurrents were obtainable with such a design.[43] In principle, the MEA approach allows for simultaneously maximizing catalytic activity and light absorption, even when using a relatively large catalyst mass loading.

Working with Lewis group graduate student Matt Shaner, I have attempted to demonstrate functional models of the MEA device structure using Si microwires with Ni–Mo catalyst and a TiO_2 light scattering layer. Figure 3.10 is a set of scanning

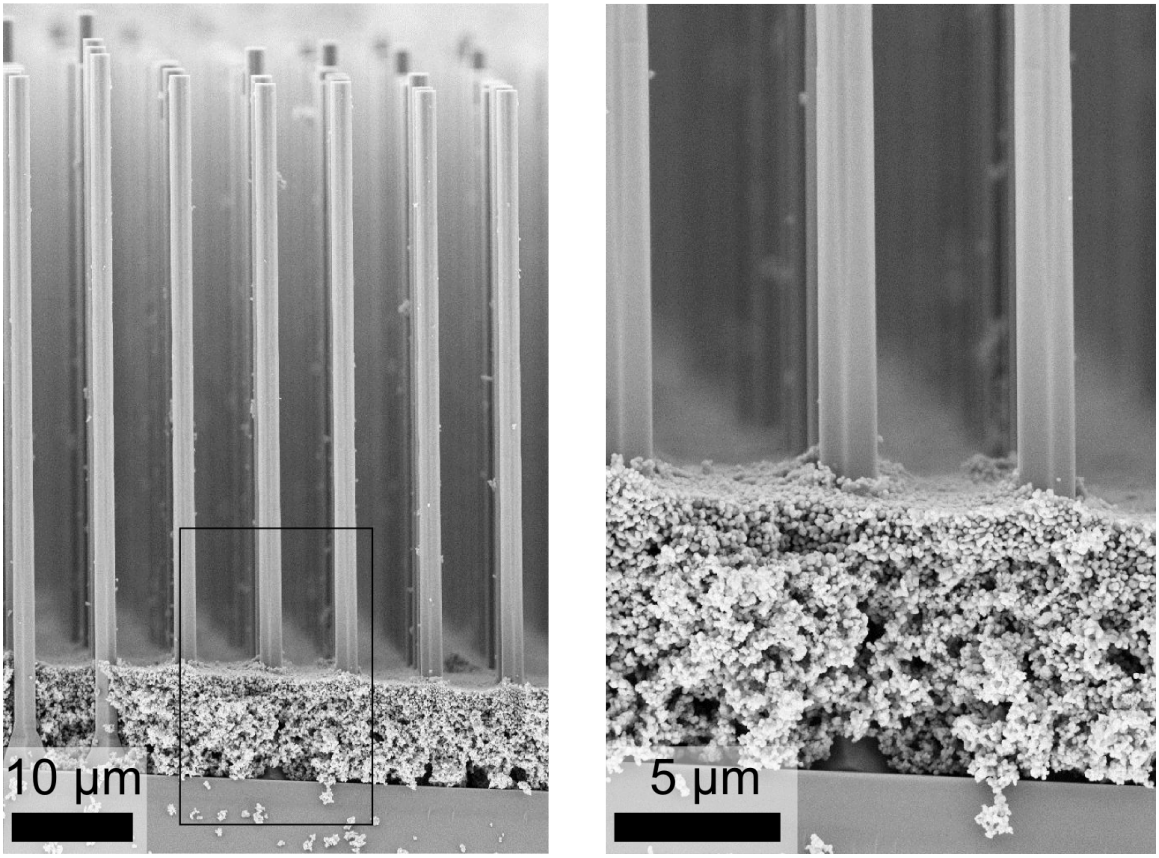

Figure 3.10. Scanning electron micrographs of a microwire array deposited with layers of Ni–Mo and TiO_2 nanoparticles at the base using a centrifugation method. The detail on the right is of the boxed area on the left. The boundary between the Ni–Mo (bottom) and TiO_2 (top) layers is discernible due to the smoother appearance and more regular size dispersity of the TiO_2 particles.

electron micrographs depicting sucessful selective deposition of these materials at the bases of microwire arrays. We accomplished this deposition by generating seperate isopropanol suspensions of Ni–Mo nanopowders, as described in Chapter 2, and TiO_2 pigment particles obtained commercially from DuPont (Ti-Pure R105). These suspensions were then sequentially flocculated to the bases of the microwire arrays by centrifugation at 3000 rpm in a standard swing-out benchtop centrifuge. To improve adhesion and proton permeability, respectively, we incorporated ∼2 wt% polytetrafluoroethylene (PTFE) to the Ni–Mo and ∼2% Nafion to the TiO_2 particle suspensions.

We evaluated the HER catalytic activities of Ni–Mo and Ni–Mo/TiO_2 films deposited at the bases of metallized Si microwire arrays in 1 M H_2SO_4. The results are

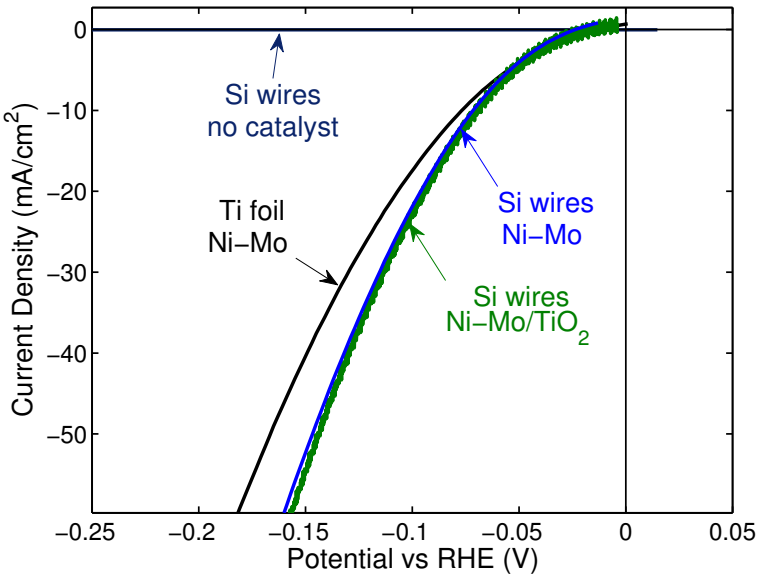

Figure 3.11. HER j–E data for Ni-Mo nanopowder and/or TiO_2 films deposited onto the noted substrates using centrifuge flocculation. The Si microwires were metallized with Al/Ag in order to ensure ohmic contact to the Ni–Mo. Data were collected in H_2-purged 1 M H_2SO_4 solution using a two-compartment cell. The counter electrode was Ru/Ir oxide deposited on a Ti mesh substrate and separated from the main compartment using a Nafion membrane. The reference electrode was acidic $Hg/HgSO_4$ located in the working compartment.

shown in Figure 3.11 compared to the HER activities of Ni–Mo on a planar Ti substrate and metallized Si microwires without catalyst. Amazingly, the HER behavior of the flocculated films matched or slightly exceeded that of same loading of pure Ni–Mo nanopowder on planar Ti. These results suggest that mass transport of reactants and products is not significantly attenuated by the presence of wire arrays or the porous scattering layer. The data also illustrate that Ni–Mo/TiO_2 MEA composite electrodes can be characterized in strong acid solution, due to the high activity and relatively stable initial performance of Ni–Mo nanopowders under these conditions, as discussed in Chapter 2.

Work is still underway to demonstrate that the Si MEA structure can give highly efficient PEC hydrogen evolution using Si microwire and non-noble catalysts. We have demonstrated thus far that the MEA approach is clearly not amenable for use in a planar geometry, as shown in Figure 3.12. The thick, light-blocking catalyst and

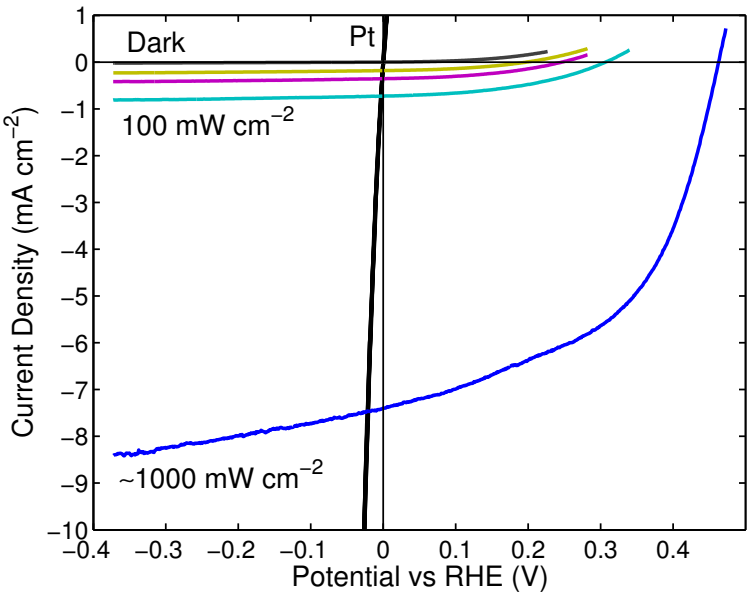

Figure 3.12. PEC hydrogen evolution j–E data for a planar Si n$^+$p-junction photoelectrode deposited with layers of Ni–Mo and TiO_2. Data were collected in H_2-purged 0.5 M H_2SO_4 aqueous solution using a Ru/Ir counter electrode in a separate fritted compartment and a Ag/AgCl reference electrode in the working compartment. Illumination was provided by a tungsten-halogen light source whose intensity was varied using OD 0.3 neutral density filters (intensities $\leq$100 mW cm^{-2}) or by moving the light source closer to the cell (>100 mW cm^{-2}).

scattering films severely attenuated the light absorbed by a planar n$^+$p-Si homojunction electrode. However, increasing the light intensity to $\sim$10 suns demonstrated that the catalytic activity of the Ni–Mo film was quite high.

We have also carried out preliminary investigations of the MEA device structure on n$^+$p-Si microwire arrays, as shown in Figure 3.13. Photovoltages for these samples were quite low, due to poor microwire and emitter material quality. But the cathodic photocurrents obtained at 100 mW cm^{-2} for short microwires that were only approximately 50% exposed were on the order of 10 mA cm^{-2}, comparable to that of the champion electrodes with electrodeposited Ni–Mo. Further, at high light intensities the catalytic activities remain quite high, with photoelectrodes achieving cathodic photocurrents of 20 mA cm^{-2} at potentials only $\sim$150 mV negative of E_{oc}.

Subsequent efforts to generate Si n$^+$p homojunctions using spin-on dopant (SOD) precursors and rapid thermal annealing (RTA) processing methods yielded Si mi-

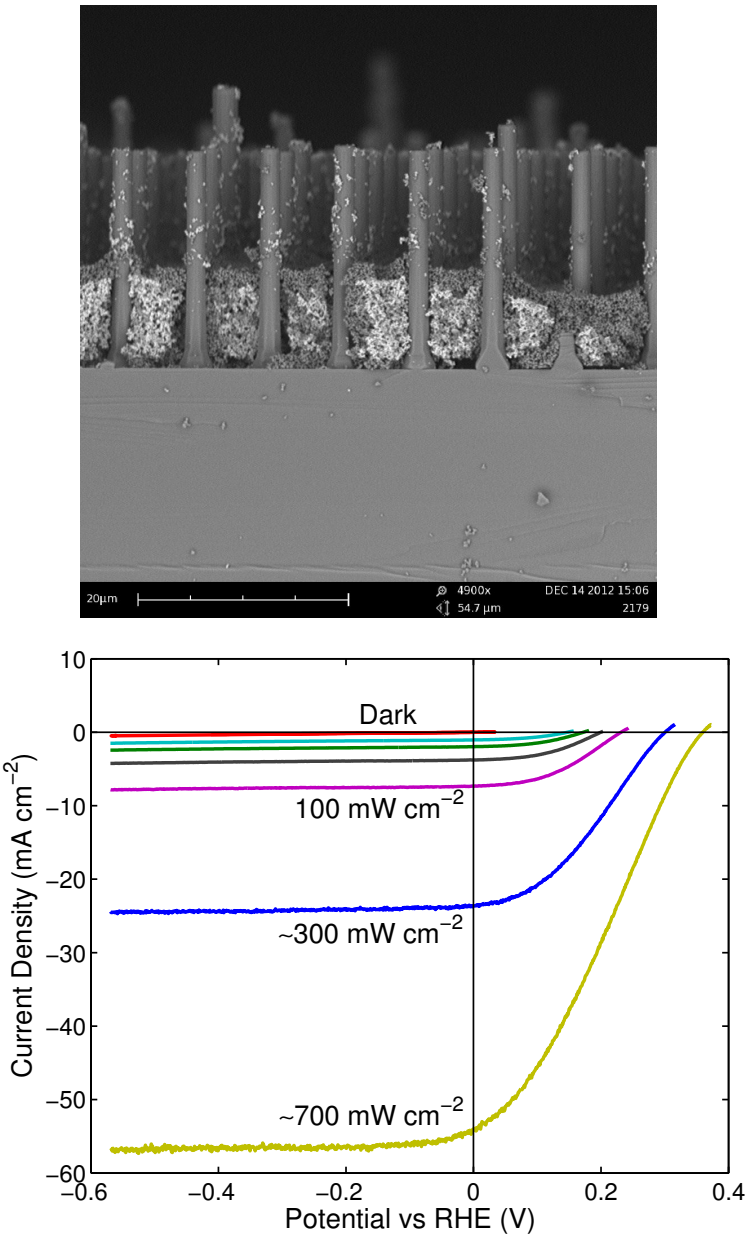

Figure 3.13. Scanning electron micrograph (top) and PEC hydrogen evolution j–E data (bottom) for a short Si microwire n^+p junction photoelectrode deposited with the Ni–Mo and TiO_2 in the MEA architecture. The HER data were collected under the same conditions as in Figure 3.12.

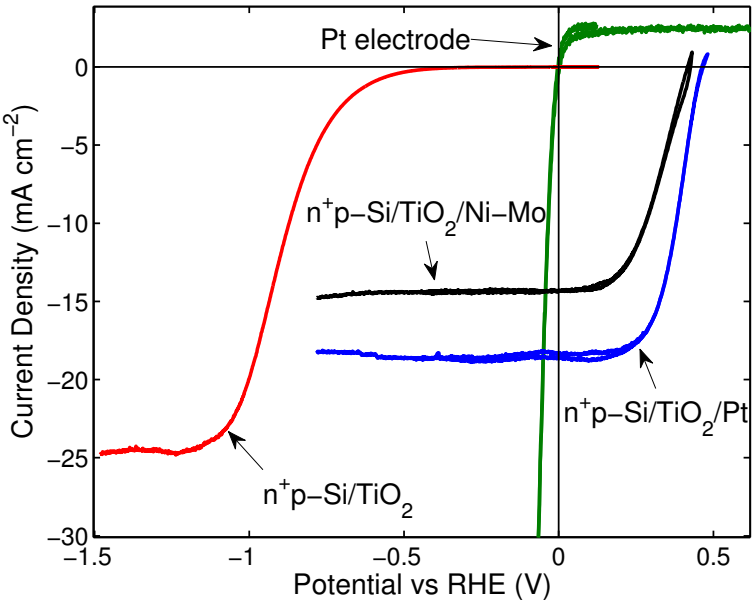

Figure 3.14. Photoelectrochemical HER j–E data for a Si microwire n^+p junction photoelectrode deposited with the noted scatterer (TiO_2) and/or catalyst (Pt, Ni–Mo) materials. The HER data were collected under the same conditions as in Figure 3.12. White light illumination at ∼100 mW cm^{-2} was provided by a tungsten-halogen light source.

crowire arrays with high photovoltages. Figure 3.14 shows the j–E behavior of several representative Si n^+p-junction photoelectrodes generated using SOD/RTA processing and then deposited with various components of the MEA device design. As expected, photoelectrodes deposited with TiO_2 particles but without a HER catalyst exhibited high photocurrents and very sluggish kinetics. Photoelectrodes deposited with Pt and Ni–Mo, respectively, gave high photovoltages, photocurrents, and improved catalysis when compared with previous attempts using electrodeposited Ni–Mo (see Figure 3.6). The Ni–Mo and Pt MEA electrodes in Figure 3.14 gave η values of 2.9% and 4.9%, respectively, demonstrating a clear improvement over previous efforts using electrodeposition.

We have made significant progress in addressing the key challenges of increasing photovoltages and mitigating parasitic light blocking from high mass loadings of non-noble catalysts. Further work on optimizing microwire growth and doping, along with catalyst and scatterer deposition, should yield Si MEA devices with η values

approaching 10% or higher using exclusively earth-abundant components. However, challenges remain in addressing the low long-term stability of Ni–Mo materials under acidic conditions. Using Ni_2P catalyst particles instead of Ni–Mo nanopowders is one promising route to improved Si MEA photocathode acid stability. Still another route involves replacing Si with another light absorber material that is stable under alkaline conditions. The next chapter presents p-type WSe_2 as a candidate semiconductor for this purpose.

Chapter 4

Tungsten Diselenide Photocathodes

4.1 Introduction and Background

This chapter details synthesis and electrochemical characterization of p-type WSe_2 photocathodes as an alternative to Si in a solar water splitting scheme. The work described herein was carried out in close collaboration with Lewis group graduate student Adam Pieterick. We synthesized highly crystalline p-type WSe_2 by a chemical vapor transport method, and characterized it as a photocathode using various redox couples, including the hydrogen couple.

Our crystalline p-WSe_2 photoelectrodes decorated with noble metal catalysts (Pt and/or Ru) exhibited strikingly high energy conversion efficiencies for hydrogen evolution. These photoelectrodes also showed good stability while carrying out reductions under simulated sunlight in aqueous solution at low and high pH. Using various electrochemical and photoelectrochemical techniques, we were able to explain both the strengths and limitations of p-WSe_2 as a candidate solar absorber in a solar water splitting scheme. The chapter concludes with some further discussion of these strengths and limitations as well as recommendations on paths forward for p-WSe_2.

As discussed in Chapters 2 and 3, Ni–Mo alloys and essentially all other non-noble catalysts consisting exclusively of transition metals suffer from low stability in acid solution, but exhibit good stability and often high activity under alkaline

Table 4.1. Optoelectronic properties for MX_2 compounds

compound	range of reported E_g (eV)	highest reported μ ($cm^2\,V^{-1}\,s^{-1}$)	highest reported L_D (μm)
MoS_2	1.2–1.4 (indirect)	90	1.4
	1.7–2.0 (direct)		
WS_2	1.29–1.34 (indirect)	290	200
	1.78–1.89 (direct)		(along basal plane)
$MoSe_2$	0.95–1.16 (indirect)	130	5
	1.35–1.47 (direct)		
WSe_2	1.16–1.55 (indirect)	330	3.85
	1.37–1.78 (direct)		

conditions. Non-noble OER catalysts such Ni, Co, and Fe oxides also are only stable under alkaline conditions. As a result, a base-stable photocathode material would be an extremely useful component for a water splitting system that incorporates only earth-abundant elements. In considering these concerns we became interested in the Mo and W chalcogenides as candidate light absorbers. Gerischer previously showed that p-type WSe_2 could be used for photoelectrochemical hydrogen evolution in strongly acidic solutions,[130] but we believed that the high stability exhibited by this class of materials might extend to neutral or alkaline conditions as well.

Materials of the type MX_2 (M=Mo, W; X=S, Se) have been thoroughly characterized with respect to their physical and electrical properties.[131] The entire class of compounds fall under the category of layered transition metal dichalcogenides. They share in comon a unique crystal structure featuring hexagonal layers of metal and chalcogens in the pattern X–M–X, as shown in Figure 4.1A and B. Each of these stoichiometric units is bonded to the next layer only by Van der Waals interactions, much as with the carbon layers in graphite. All of the layered MX_2 compounds exhibit very easy cleavage along the Van der Waals or basal plane. They also exhibit highly anisotropic electronic properties, which has significant implications for photoelectrochemical behavior. Several key optoelectronic properties for each of the four Mo and W sulfide and selenide compounds are collected in Table 4.1.[131]

The coordination environment around the metal in MX_2 compounds is trigonal prismatic, analogous to many of the homoleptic dithiolene complexes of Mo and

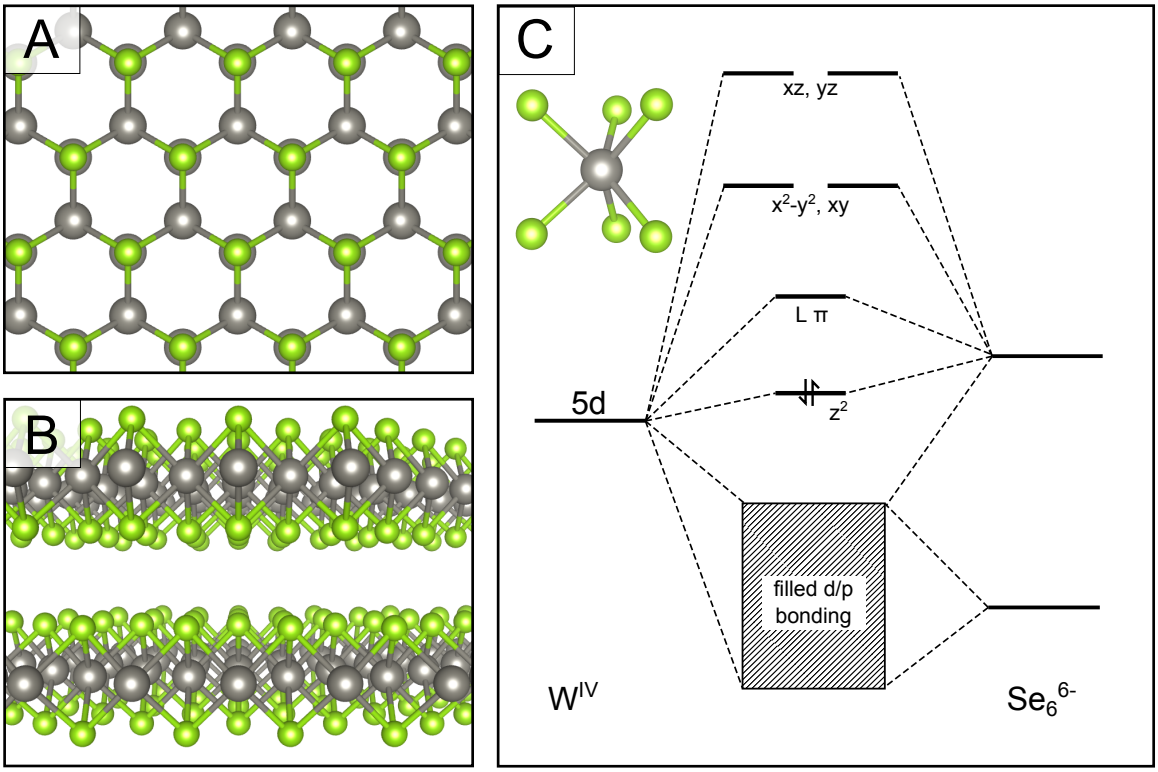

Figure 4.1. (A) Crystal structure of WSe_2 sighted along the c axis. (B) Crystal structure of WSe_2 sighted along the a* axis. (C) Molecular orbital diagram for a trigonal prismatic WSe_6 unit, adapted from the diagram proposed for Mo dithiolene complexes by Tenderholt, et al.[132]

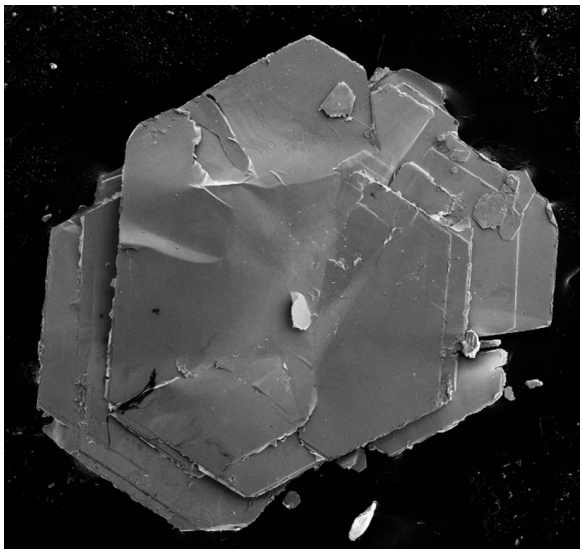

Figure 4.2. Scanning electron micrograph of an as-grown WS_2 crystal exhibiting the characteristic layered hexagonal crystal habit. Full scale of the image is approximately 2 mm.

W. The electronic structure of trigonal prismatic transition metal dithiolenes has been a matter of considerable debate,[133,134] but the most recent data suggest that Mo and W trigonal prismatic dithiolenes are best describes as d^2 systems with the highest occupied molecular orbital consisting of essentially nonbonding d_{z^2}.[132] This is largely in agreement with the consensus for electronic structure of layered MX_2 solids.[135,136] Figure 4.1C depicts a molecular orbital diagram for a putative WSe_6 fragment, illustrating its trigonal prismatic splitting and highly covalent interactions. Figure 4.2 also shows a scanning electron micrograph of a small WS_2 crystallite, clearly demonstrating its layered hexagonal crystal habit.

The fundamental optical transition in crystalline MX_2 exhibits considerably larger oscillator strength than the fundamental oxygen 2p to metal d band gap in metal oxide semiconductors, due to relaxed selection rules arising from highly covalent metal-chalcogen bonding. Also, the layered MX_2 compounds' absorption onsets are in the red or near-infrared spectrum, with fundamental band gaps ranging from $\sim$1 eV for $MoSe_2$ to $\sim$1.3 eV for WS_2 (Table 4.1). The selenides in particular have direct transitions fairly close in energy to the indirect edge. As a result, all of these semiconductors are very good visible light absorbers.

Table 4.2. Compiled figures of merit from previous examples of efficient MX_2 photoelectrodes in contact with aqueous redox couples

semiconductor	redox couple	reported η (%)	reference
n-WSe2	I^-/I_3^-	10.2	Kline 1981[141]
n-WSe_2	I^-/I_3^-	14.3	Tenne 1985[142]
n-WSe_2	I^-/I_3^-	17.1	Prasad 1988[139]
n-$MoSe_2$	I^-/I_3^-	9.4	Kline 1981[141]
n-WS_2	Br^-/Br_3^-	6.0	Kline 1982[140]
n-MoS_2	Br^-/Br_3^-	4.1	Kline 1982[140]
p-WS_2/Pt	H^+/H_2	12 (monochrom.)	Baglio 1983[117]

The layered Mo and W chalcogenides were studied heavily in the early years of semiconductor photoelectrochemistry.[131,137] Tributsch and Bennet postulated in 1977 that due to the unique geometric and electronic structure, a pristine MX_2 crystal surface would exhibit very high stability.[138] Researchers have grown single crystals by chemical vapor transport (CVT) that naturally exhibit n-type doping and long carrier lifetimes, allowing for efficient extraction of photocarriers.[131] Table 4.2 includes a set of collected figures of merit for various n-type MX_2 compounds in photoelectrochemical cells. Of particular interest is the fact that n-WSe_2 photoelectrodes have exhibited η values as high as 17.1%[139] and, in a separate report, did not degrade after passing an integrated charge of 400,000 C cm^{-2},[140] which is equivalent to >5,000 hours of continuous operation at 20 mA cm^{-2}. This material is one of the only examples of demonstrated PEC energy conversion efficiency and stability rivaling that of solid-state photovoltaics.

The particular high η values achieved using n-type W and Mo selenides in contact with the I^-/I_3^- couple were determined to stem from a specific interaction between the crystal surface and adsorbed iodide species. This adsorption shifted the band edges in the negative direction, which is favorable for generating large photovoltages, and also enabled facile catalysis of the inner-sphere electron transfer involved in iodide oxidation.[143,144] Unfortunately, work on polycrystalline samples of MX_2 never yielded efficiencies approaching that of the best single crystals.[145] Also, efficiencies only as high as 8% were obtained for solid-state heterojunctions of p-WSe_2 with ZnO.[146] As a result, compounds in this class were generally abandoned as candidates for

commercial solar cells in favor of, e.g., the cadmiun and copper-based chalcogenides that are used as thin-film PV materials today.[147,148] In any case, the success of this class of compounds in efficient, stable aqueous photoelectrochemical energy conversion remains remarkable to this day.

Curiously, in the course of all of the development of layered MX_2 materials for photoelectrochemistry, relatively little was done to assess the possibility of synthesis and use of p-type crystals as aqueous or nonaqueous photocathodes. As noted previously, Gerischer et al. briefly studied the HER properties of p-WSe_2 coated with thin Pt films under strongly acidic conditions, achieving high photovoltages but low net energy conversion efficiencies.[130] Cabrera and Abruña synthesized polycrystalline p-type MX_2 films and found that they exhibited reasonably large photovoltages but low photocurrents under monochromatic and white-light illumination.[145] The Wrighton group, in collaboration with crystal growers from GTE technologies, successfully synthesized p-WS_2 single crystals and found that they gave very large photovoltages for hydrogen evolution in strong acid when decorated with Pt cocatalysts.[117] This result in particular motivated our work on p-WSe_2 materials in attempts to achieve similarly high photovoltages and improved η values as compared with Gerischer's work.

4.2 Synthesis

We synthesized single crystals of WS_2 and WSe_2 with both n- and p-type doping types using CVT.[149] The CVT process is illustrated in Figure 4.3. A purified polycrystalline powder of the desired semiconductor can be either purchased or synthesized by reaction of the individual component at high temperatures ($\geq$1000 °C for Mo/W sulfides and $\geq$800 °C for selenides) in an evacuated, sealed quartz ampule. Then the transport reaction is carried out by loading the desired quantity of polycrystalline material into a fresh ampule along with a small quantity of a transport agent. The ampule is evacuated and sealed, and powder plus transport agent is heated in a small temperature gradient (generally 1–2 °C per linear cm for MX_2 compounds) at high temperatures ($\geq$1000 °C) over a span of tens to several hundred hours. After the

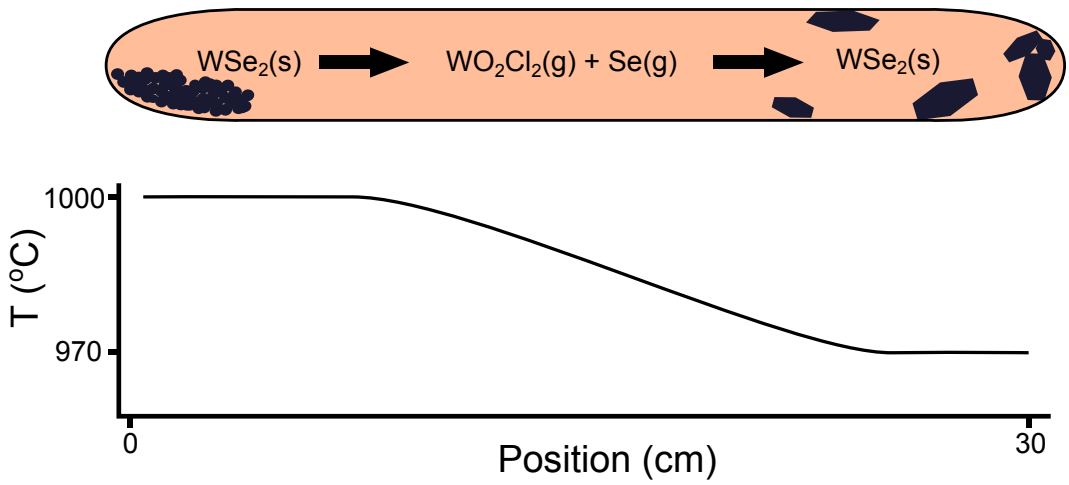

Figure 4.3. Reaction scheme (top) and temperature gradient required (bottom) for growth of crystalline MX_2 from polycrystalline starting materials in a sealed tube using the CVT method. The position scale on the gradient plot corresponds to the tube diagram above.

growth interval, the ampule is cooled and carefully broken to give access to one or more relatively large single crystals that nucleated and grew within the tube.

During CVT crystallization the transport agent reacts with the polycrystalline powder to generate a low steady state concentration of volatile species, which is in dynamic equilibrium with the solid phase. The temperature gradient provides both convective transport and a small thermodynamic driving force for transfer of the solid material from the "hot" zone toward the "cold" zone. If the kinetics and cleanliness of the system are appropriate, the transport reaction proceeds by spontaneous nucleation and slow growth of only one or a limited number of crystal nuclei, resulting in relatively large single crystals with high electronic quality.

CVT for growth of Mo and W chalcogenide crystals has been successfully implemented by several research groups,[150–155] but relatively little is understood about the dynamics of the process. Crystal growth is widely considered to be a "black art," requiring extensive trial and error before a working method is found. This quality is reflected for MX_2 crystal growth in that many groups have reported similar procedures with widely varying results in terms of crystal quality, size, and electronic properties (e.g., majority carrier type and concentration). However, generally the

best results for WSe_2 growth have involved the use of chlorine-containing transport agents and no explicit dopant, which results in n-type crystals.

Studies from Koval et al.,[154] Legma et al.,[155] and Baglio et al.[152] attempted to systematically address the dynamics and thereby optimize methods for growth of Mo and W selenides and sulfides. Koval et al. and Legma et al. found that Cl_2 derived from $SeCl_4$ was the best transport agent for n-type WSe_2. Koval and coworkers also found that pure I_2 was best for p-type samples. These authors noted, however, the inherent difficulty in reproducing previously reported results for MX_2 CVT growth.

Baglio and coworkers carried out computer simulations based on known thermodynamic parameters for all the species that they expected to be present in the growth ampule under conditions of WS_2 crystallization.[152] Interestingly, their simulations indicated that WO_2Cl_2 was the dominant transport species. This was in spite of the fact that WCl_4 is thermodynamically accessible and more volatile and that they did not explicitly include oxygen or water as components of simulation. Instead the simulation indicated that trace water and/or oxygen derived from the quartz ampule were sufficient to allow for dominant transport by WO_2Cl_2. They also found that addition of Nb to their growth simulation resulted in a small steady state concentration of $NbOCl_3$ vapor at the growth temperature, which would accounted for the observed incorporation of Nb as a p-type dopant in WS_2 crystal growth.

Based on the results from Baglio et al., we concluded that it might be sufficient to simply include WO_2Cl_2 directly as a transport species into WSe_2 crystal growths. The rationale was that addition of this reagent would automatically provide the proper proportion of Cl and O species for efficient transport. As an additional benefit, WO_2Cl_2 can be handled on the benchtop provided it is not excessively exposed to water or atmosphere. Using parameters otherwise matching those of Baglio, et al., we included a quantity of WO_2Cl_2 sufficient to produce 0.5 atm pressure of Cl_2 gas upon complete volatilization. We also included an excess quantity of pure Se to allow for stoichiometric conversion of the excess W from the WO_2Cl_2 to WSe_2. The results were successful growths of both Nb-doped p-type and undoped n-type WSe_2 crystals after several days of transport at temperatures between 900 and 1000 °C. Figure 4.4

Figure 4.4. Photograph of a large WSe_2 crystallite grown by CVT using WO_2Cl_2 transport agent without any extrinsic doping source. Numbered demarcations on the ruler are centimeters.

shows an optical image of one of the largest apparently single-crystalline specimens of undoped WSe_2 grown by this method. Addition of Nb to the transport reaction significantly decreased the yield and size of the crystallites grown over the same time period as an undoped growth. However, p-WSe_2 crystals gave remarkable efficient and stable photoreductions, as described in the following sections.

4.3 Initial HER Studies

Since many of the favorable properties of WSe_2 light absorbers were already understood from studies on n-type material, we decided to undertake studies of its hydrogen evolution properties immediately upon sucessfully synthesizing p-type crystals of sufficient size for mounting as electrodes. We found that both Ga/In eutectic as well as pure In were able to give ohmic contact to p-WSe_2 samples after being rubbed or soldered onto the crystal surface, respectively. However, the best quality electrodes were obtained by first generating the ohmic back contact with In solder and then carefully removing one or more layers from the front face of the electrode using adhesive tape, until a surface with minimal texture was revealed.

We found that the best performing electrodes had essentially no defects visible under an optical microscope at 1000× magnification, indicating surface features smaller than a few hundred nm. This was consistent with the results of many previous re-

searchers who generally found that exposed defects and/or edge sites (i.e., planes other than the basal plane) correlated with diminished photovoltage and photocurrent.[144,156,157] These defects were believed to act as recombination centers or to disrupt the formation of a space-charge region in the semiconductor.[130]

We tested p-WSe_2 electrodes for their hydrogen evlution properties in aqueous solutions without any catalyst and with electrodeposited noble metal catalysts. We deliberately eschewed the use of non-noble catalysts such as Ni–Mo with p-WSe_2 due to the fact that neither the catalytic nor stability properties of either were well-defined. On the other hand, the noble metals are known to be highly active toward hydrogen evolution, and to exhibit slightly attenuated activity under alkaline conditions. Also, they are indefinitely stable toward corrosion in both acidic and alkaline aqueous solution over the timescales relevant for assessing hydrogen evolution behavior.

In the absense of catalyst, p-WSe_2 photoelectodes exhibited little to no activity toward the HER in aqueous solution either in the dark or under illumination, as shown in Figure 4.5. The crystals were also impressively stable toward oxidation, showing no significant anodic current until cycled to the oxygen evolution potential ($\sim$1.25 V vs. RHE). We anticipated that the material might exhibit some HER catalytic activity, since MoS_2 and WS_2 materials were recently shown to be rather efficient HER electrocatalysts.[64,105,158,159] On the other hand, the HER activity of MoS_2 stems from exposed edge sites, rather than basal planes. Since our electrodes were highly crystalline and deliberately cleaved so as to expose a minimum of edge sites, the low observed catalytic activity is not at all incompatible with the possibility of similarly high catlytic activity for WSe_2 edge sites. In fact, the Cui group recently reported that $MoSe_2$ nanomaterials exhibit essentially identical high catalytic activity as MoS_2, which implies that WSe_2 edges are likely also active toward the HER.[160]

We carried out initial HER characterization of freshly synthesized and contacted p-WSe_2 in several different electrolytes, including 0.5 M K_2SO_4 with 0.2 M potassium hydrogen phthalate (KHP) buffer at pH 4.25, and in 2 M KOH solution. Immediately we observed promising results: j–E data for hydrogen evolution from one of the first p-WSe_2 electrodes deposited with Pt by dropcasting a 50 mM H_2PtCl_6 solution onto the

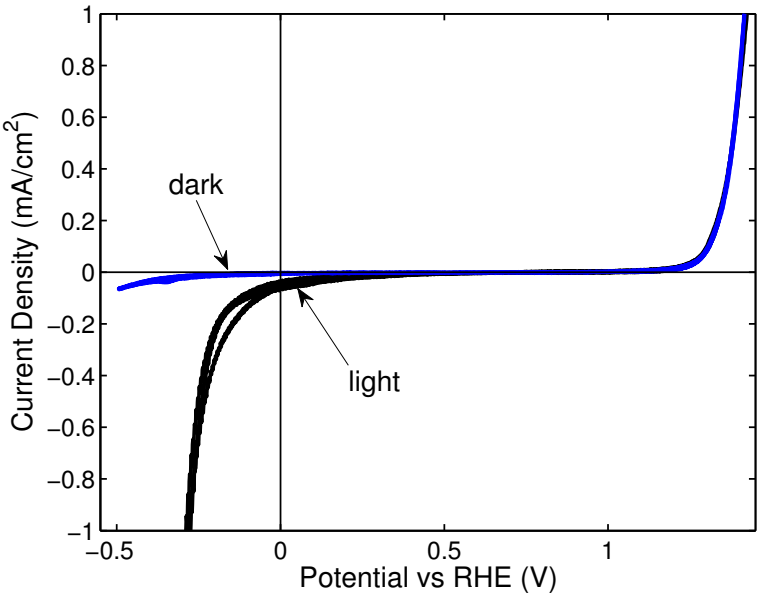

Figure 4.5. Electrochemical j–E data illustrating the low catalytic activity of pristine p-WSe_2toward the HER in the dark and under illumination. Data were collected in H_2-saturated 0.5 M K_2SO_4 solution with 0.2 M KHP buffer at pH 4.5. Counter and reference electrodes were a Pt mesh in a separate fritted compartment and SCE, respectively. The curve labeled "light" was taken under 100 mW cm^{-2} illumination from a tungsten-halogen light source.

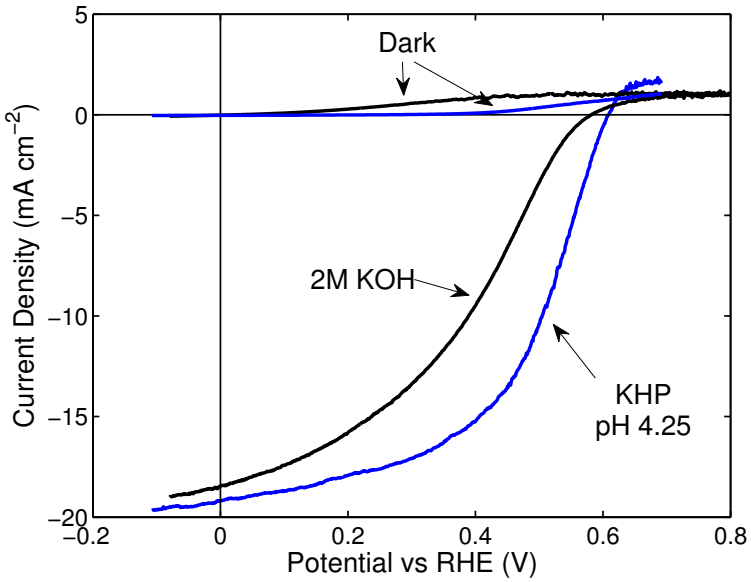

Figure 4.6. Initial photoelectrochemical HER j–E behavior of p-WSe_2 photoelectrodes deposited with Pt catalyst from H_2PtCl_6 solution in mildly acidic and strongly alkaline aqueous solutions. Data labeled "KHP pH 4.25" were taken under the same cell, electrolyte, and illumination conditions as noted in Figure 4.5, except the pH was adjusted to pH 4.25. Data labeled "2M KOH" were taken in a single-compartment cell using H_2-purged aqueous 2 M KOH solution with a nickel mesh counter electrode and an alkaline Hg/HgO reference, under an illumination intensity of 100 mW cm^{-2} from a tungsten-halogen source.

surface are shown in Figure 4.6. These electrodes exhibited photovoltages approaching 0.6 V and also large cathodic j_{sc} values approaching 20 mA cm^{-2}. Catalytic "turn-on" behavior under alkaline conditions were somewhat more sluggish than in acid solutions, which was unsurprising given the attenuated activity of Pt toward the HER under alkaline conditions. These results led us to develop optimized protocols for catalyst deposition and HER experimentation.

4.4 Optimized HER Studies

In order to further improve HER activity, we deposited Pt and Ru catalysts by the method reported by Heller et al. for deposition of these metals onto InP photocathodes.[123] This method involved illuminating the semiconductor in an acidic solution

with a low concentration of a metal chloride precursor and then depositing at a potential where the photovoltage of the semiconductor significantly contributed to the electrodeposition process. Figure 4.7 illustrates the electrochemical behavior of illuminated p-WSe_2 electrodes during deposition of Pt using chopped illumination and Ru using continuous illumination, respectively. Both curves in Figure 4.7 show induction periods of relatively low current, followed by a monotonic increase in current and eventual a saturation. We believe that the induction period corresponded to the time interval over which catalyst particles nucleated on the crystal surface. The current increase and saturation corresponded to the onset of vigorous hydrogen evolution in the acidic electrolyte due to continued deposition of catalyst. Current due to catalyst deposition itself was likely a minor contribution to the final total current, due to the relatively low concentration of metal salts ($\leq$1 mM) in solution.

Catalysts deposited onto WSe_2 surfaces exhibited a nanoparticular morphology, as shown in the micrograph in Figure 4.8. Although the entire surface of the semiconductor was deposited with discontinuous particles, there was preferential deposition of continuous "nanowires" of metal along the step edges of the WSe_2 surfaces. This is very similar to the behavior observed for metal electrodeposition onto freshly prepared highly-oriented pyrolytic graphite surfaces.[161]

HER j–E results from p-WSe_2 samples with optimized surface preparation and catalyst depositions in mildly acidic aqueous solution are shown in Figure 4.9. The highest η_{HER} values were obtained in KHP solution at pH 4.25, which was unexpected considering that this electrolyte had the lowest concentration of reactant HA species of all those tested. Importantly, we also consistently observed the largest V_{oc} values from photoelectrodes that had been first deposited with Ru by the method shown in Figure 4.7, then immediately dipped for several seconds into a 50 mM H_2PtCl_6 solution, rinsed, and finally tested for PEC hydrogen evolution. We believe in this case Pt was deposited by galvanic displacement of the outer layer(s) of Ru metal. Therefore the electrode surface exhibited favorable interfacial energetics due to direct contact with Ru metal; but the photoelectrode also exhibited catalytic activity consistent with catalysis by Pt.

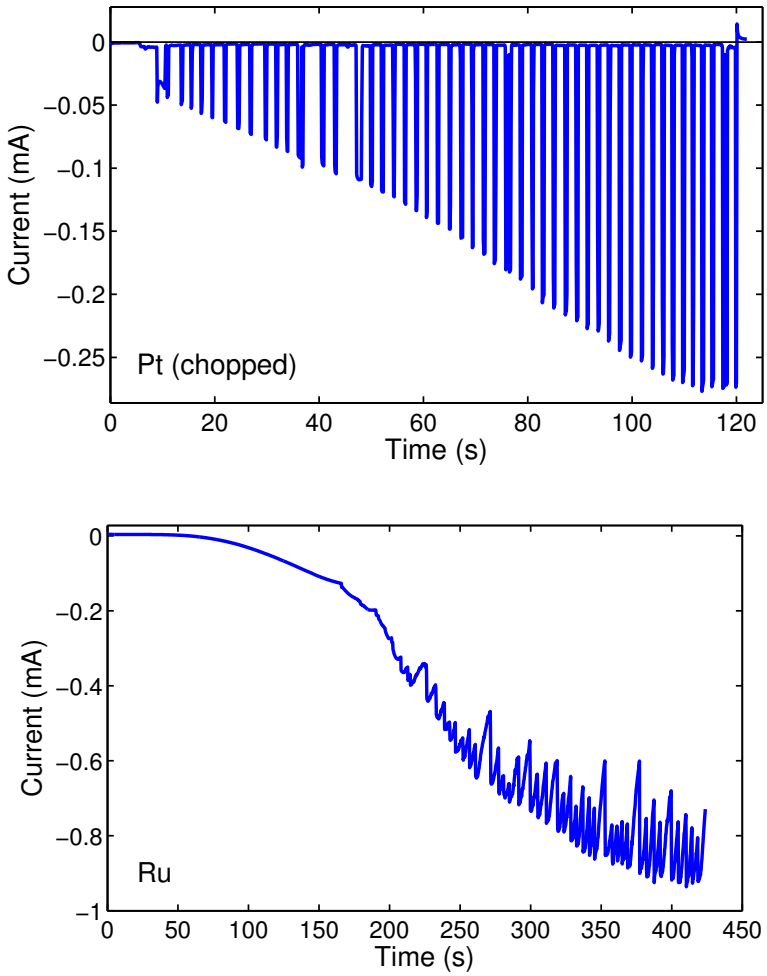

Figure 4.7. PEC j–E data for deposition of Pt (top) and Ru (bottom) catalysts on the surface of p-WSe_2 photoelectrodes. For Pt deposition, the solution contained 1 mM H_2PtCl_6, whereas for Ru the solution contained 0.1 mM $RuCl_3$. In both cases the supporting electrolyte was 0.1 M HCl, and the deposition was carried out at a potential of −0.1 V vs. SCE using a single-chamber cell with a Pt counter electrode. Electrodes were illuminated with white light from a tungsten-halogen bulb at ∼100 mW cm^{-2}. The Pt data reflect the fact that the illumination was manually "chopped" by intermittant blocking at the source with an opaque object at a frequency of ∼0.5 Hz. From McKone et al.[53]

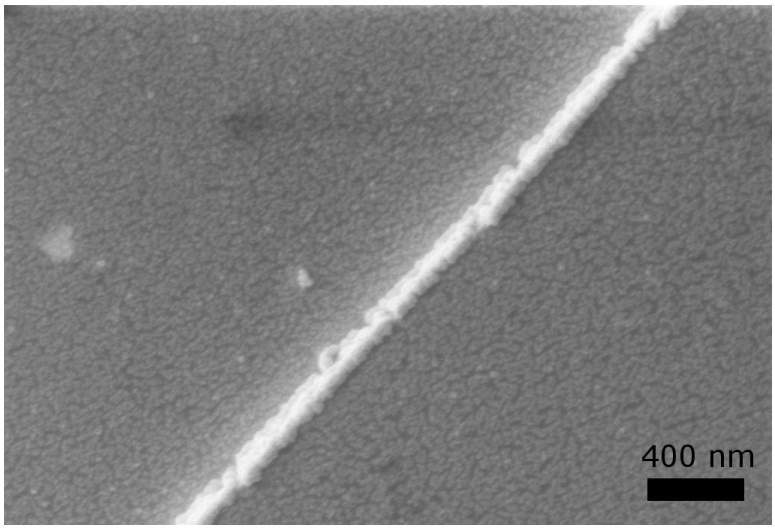

Figure 4.8. Scanning electron micrograph of a p-WSe_2 electrode after Pt deposition and photoelectrochemical HER testing. The Pt film exhibited a nanostructured morphology with preferential deposition of metal along crystal step edges.

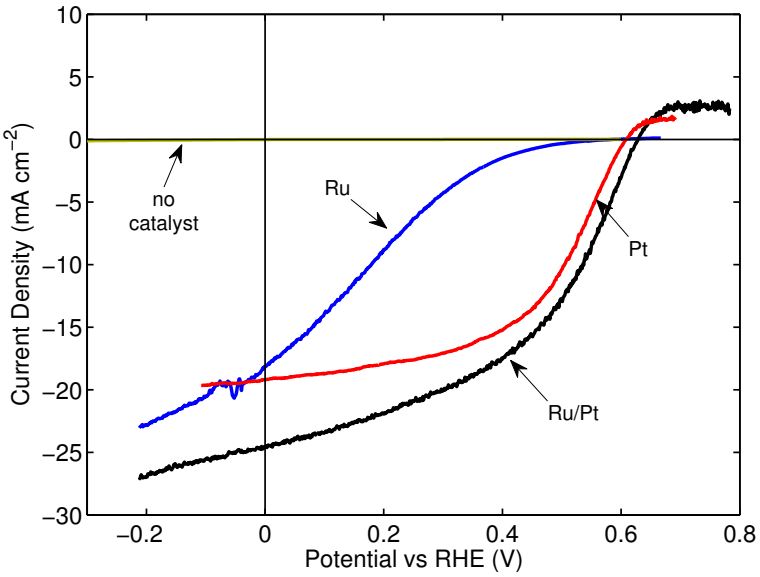

Figure 4.9. PEC hydrogen evolution j–E data for illuminated p-WSe_2 photoelectrodes deposited with the noted catalysts using optimized methods. Data were collected under 100 mW cm^{-2} illumination from a tungsten-halogen light source under the same cell and electrolyte conditions as the KHP data in Figure 4.6. From McKone et al.[53] Copyright 2013 the American Chemical Society; used with permission.

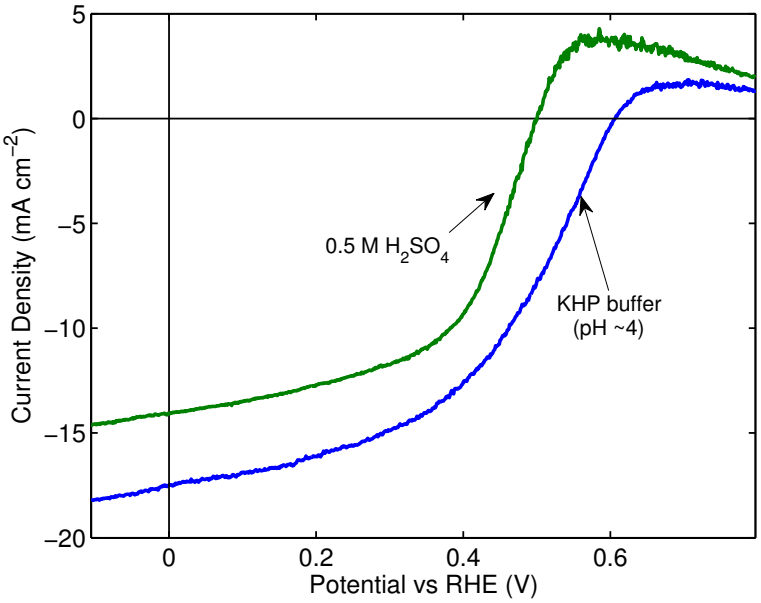

Figure 4.10. Comparison of PEC HER results for a single p-WSe_2/Pt in two different electrolytes. Cell, electrolyte, and illumination conditions were as in Figure 4.9 for the data labeled "KHP buffer," and otherwise identical except for the use of 0.5 M H_2SO_4 electrolyte and an acidic $Hg/HgSO_4$ reference electrode in the case of the data labeled "0.5 M H_2SO_4." From McKone et al.[53] Copyright 2013 the American Chemical Society; used with permission.

Figure 4.10 illustrates clearly the difference in j–E behavior for a single photoelectrode carrying out the HER under mildly acidic and strongly acidic conditions. In KHP solution at pH 4.25, the photoelectrode exhibited significantly increased V_{oc} and j_{sc}, resulting in a large increase in η from 3.9% to 5.1%. This increase was in spite of the higher HER activity for the Pt cocatalyst, as clearly indicated by the faster cathodic current onset and larger mass-transport limited hydrogen oxidation current at potentials just positive of E_{oc}.

Table 4.3 presents collected energy conversion figures of merit for p-WSe_2 photoelectrodes carrying out the HER under various conditions and with various catalysts. Overall, several salient features of these photoelectrochemical HER data on p-WSe_2/catalyst photoelectrodes stood out. First, the η_{HER} values were impressively large considering the minimal extent of synthesis and processing optimization. Second, the photoelectrodes appear to have benefited from direct contact to Ru metal

Table 4.3. Compiled figures of merit for PEC hydrogen evolution on p-WSe_2 photoelectrodes

electrode #	catalyst	electrolyte	V_{oc} (mV)	j_{sc} (mA cm^{-2})	ff	η_{HER} (%)
412	Ru	KHP (pH 4.25)	660	−16.3	0.31	3.3
400	Pt	KHP (pH 4.25)	610	−19.2	0.53	6.2
415	Pt	KHP (pH 4.25)	570	−20.3	0.44	5.1
400	Pt	2M KOH	580	−18.5	0.38	4.1
463	Ru/Pt	H_2SO_4	525	−20.5	0.53	5.6
464	Ru/Pt	H_2SO_4	610	−22.1	0.52	7.0
458	Ru/Pt	KHP (pH 4.25)	635	−21.7	0.45	6.1
459	Ru/Pt	KHP (pH 4.25)	630	−24.5	0.46	7.2

rather than Pt metal. However, Pt was required in order to obtain the best HER activity. Finally, as previously noted, the η_{HER} values of these photoelectrodes were maximized under mildly acidic conditions.

4.5 Further Characterization

The promising results we observed for PEC hydrogen evolution from p-WSe_2 decorated with noble metal catalysts prompted us to carry out further experiments for a more detailed understanding of its properties. We evaluated reductive stability under both acidic and alkaline conditions and we used spectral response measurements to evaluate the carrier dynamics of p-WSe_2 crystals. We also measured the energy-conversion behavior of p-WSe_2 in aqueous $Ru(NH_3)_6^{3+/2+}$ ($RuHex^{3+/2+}$) electrolyte in order to evaluate the energy conversion properties in the absence of catlayst. Finally, we used Mott-Schottky measurements to define the band-edge energetics for p-WSe_2 and better understand the observed differences in photovoltages in solutions of varying pH.

Stability experiments in aqueous methyl viologen ($MV^{2+/+}$) solution were used to assess the electrochemical stability of p-WSe_2 under reducing conditions. Electrodes without catalyst were used for this experiment, because the corrosion, poisoning, or detachment of catalyst species are all possible sources of degraded PEC performance in addition to semiconductor instability. Using a fast, one-electron redox couple

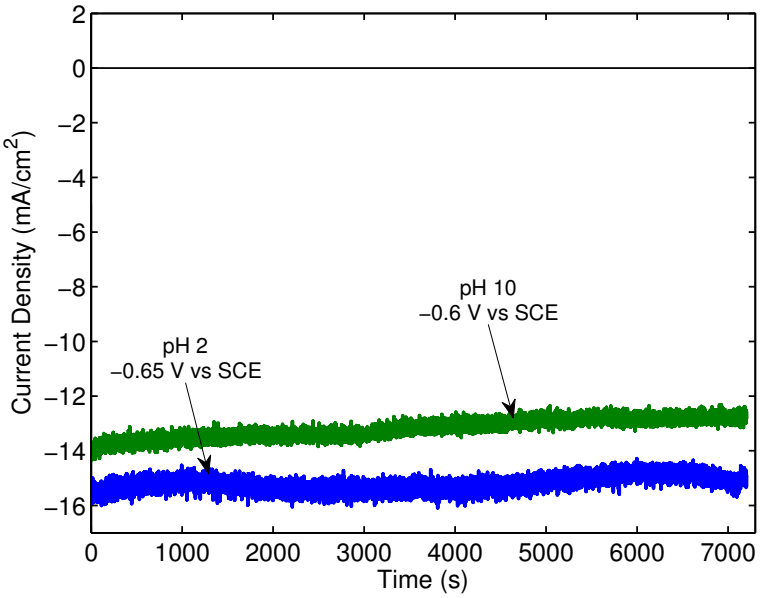

Figure 4.11. Potentiostatic i–t data for a p-WSe_2 photoelectrode undergoing stability testing in MV^{2+} solution. PEC data were collected in 50 mM MV^{2+} aqueous solution with 0.5 M KP_i supporting electrolyte buffered to the noted pH values. The data were collected consecutively, beginning with pH 2 and then at pH 10. The electrodes were poised at the noted potentials under illumination at ∼100 mW cm^{-2} intensity using a tungsten-halogen bulb. The counter electrode was a Pt mesh in the same compartment as the working electrode. From McKone et al.[53] Copyright 2013 the American Chemical Society; used with permission.

allowed for a direct probe of stability without the convoluting effects of catalysts. We chose $MV^{2+/+}$ due to its fast kinetics and good stability over a wide range of aqueous pH values.[45,162]

Figures 4.11 and 4.12 show representative results for stability studies of a p-WSe_2 photoelectrode in $MV^{2+/+}$. The electrode was first imaged in an optical microscope, then illuminated and poised potentiostatically in an optically clear 50 mM MV^{2+} solution at pH 2. The applied potential was sufficient to produce a photocurrent similar to that observed in the previously discussed HER experiments. After two hours the electrode was removed, rinsed, and imaged again before repeating the stability test in an otherwise identical MV^{2+} solution at pH 10. Then the electrode was imaged a final time.

As is clear from Figures 4.11 and 4.12, the p-WSe_2 electrode exhibited high stabil-

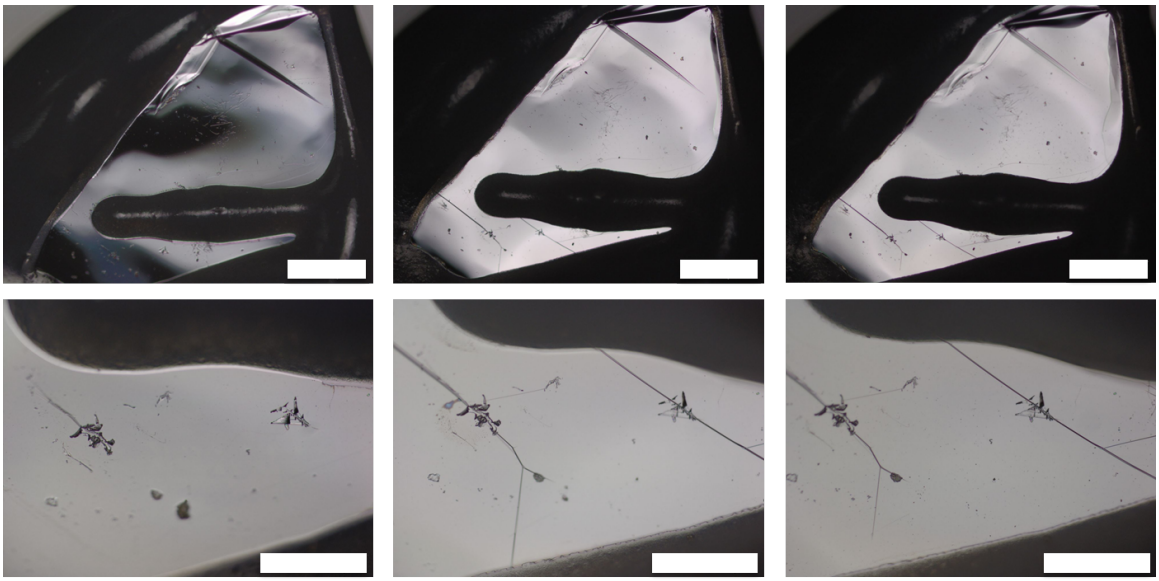

Figure 4.12. Optical micrographs at low (top) and high (bottom) magnification of the electrode used for PEC measurements in Figure 4.11 before stability testing (left), after testing at pH 2 (middle), and after testing at pH 10 (right). Scale bars are 500 μm (top) and 200 μm (bottom).

ity under both acidic and alkaline conditions. The cathodic photocurrent degraded by a very small amount during testing in acid, and then degraded from ∼14 to ∼12.5 mA cm^{-2} over the course of the experiment at pH 10. The associated micrographs show only the emergence of a few small cracks after the acid experiment, and then no further change after testing at pH 10. The cracks appeared to coincide with existing defects in the crystal surface, suggesting some corrosion associated with defects or surface step edges.

The total charge passed during each of the stability experiments was ∼25 μmol, which was nearly 10 times larger than the ∼3.5 μmol of WSe_2 contained in the active area of the photoelectrode (based on a electrode thickness of 50 μm estimated from SEM). Therefore if even 1% of the total current passed during the experiment contributed to corrosion, >10% of the electrode would have dissolved, and so the electrode surface would have been significantly degraded. We conclude, then, that p-WSe_2 is quite stable under reducing conditions, but perhaps suffers from slow corrosion primarily at defects and/or step edges. This is consistent with the corrosion behavior that was observed previously for WSe_2 photoelectrodes under oxidizing con-

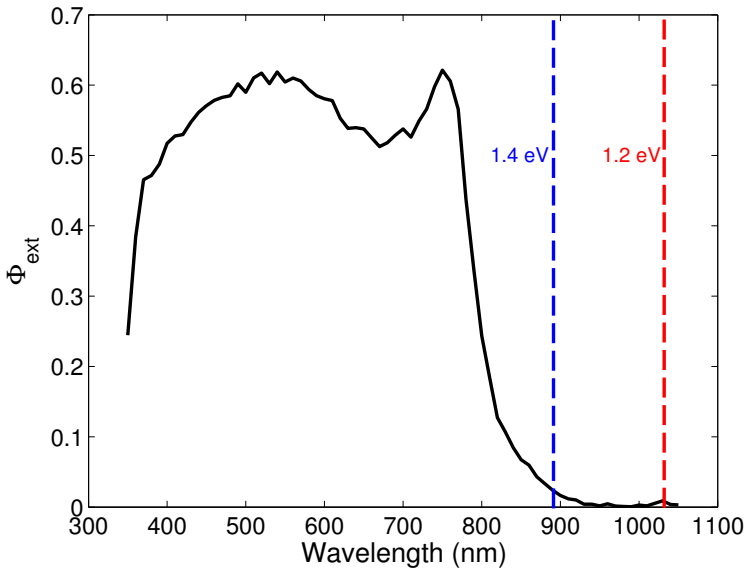

Figure 4.13. Spectral response data for a representative p-WSe_2 photoelectrode. Red and blue dotted lines correspond to the indirect and direct bandgaps of WSe_2, respectively. Data were collected in aqueous 50 mM MV^{2+} with 0.5 M K_2SO_4 supporting electrolyte and 0.2 M KHP buffer at pH 4.2. The electrode potential was poised potentiostatically at −0.4 V vs. SCE and illuminated with a Xenon lamp chopped at 13 Hz and swept from 1050 to 350 nm in 10 nm steps. From McKone et al.[53] Copyright 2013 the American Chemical Society; used with permission.

ditions in acid solution.[163] More extensive stability experiments would be helpful in determining the source of any corrosion, as well as the long-term stability of p-WSe_2 carrying out relevant reductions, such as hydrogen evolution.

We carried out spectral response measurements of p-WSe_2 also in contact with clear MV^{2+} solution. Photoelectrodes were poised at −0.4 V vs. SCE, which was sufficiently negative to generate the maximum observable photocurrent without significant contribution from dark currents. Full results for a representative photoelectrode are shown in Figure 4.13. The maximum observed Φ_{ext} values of ∼0.6 were obtained at wavelengths below 775 nm. Given the highly smooth and reflective surface of cleaved WSe_2 electrodes, surface reflection losses may have been as high as 30–40%, which suggests that the observed maximum Φ_{ext} values likely corresponded to values of Φ_{int} approaching unity.

The highest Φ_{ext} values were not obtained until the photon energy was well above

the direct bandgap of WSe_2 (around 890 nm). We concluded that the minority carrier diffusion lengths of these samples were low, such that a large proportion of the low energy photons penetrated too deeply into the semiconductor to be collected. Figure 4.14 shows a detail of the spectral response data at the spectral onset of quantum yield, along with a set of calculated values based on the Gärtner model of carrier diffusion (Equation 4.1):[164]

$$\Phi_{\text{int}} = 1 - \frac{e^{-\alpha W}}{1 + \alpha L_{\text{D}}} \tag{4.1}$$

where α is the semiconductor absorption coefficient, W is the depletion width, and L_{D} is the effective minority-carrier diffusion length. In this case, the normalized Φ_{ext} was used instead of Φ_{int} under the assumption that the maximum Φ_{ext} corresponded to near unity Φ_{int}.

Analysis according to the Gärtner model has been carried out previously on WSe_2 photoelectrodes, resulting in observed values of L_{D} as high as 4 μm.[157] Our model clearly indicated effective L_{D} values only on the order of 1 μm, suggesting that minority carrier lifetimes could be improved, resulting in significantly increased photocurrents.

We characterized the energy conversion properties of bare p-WSe_2 photoelectrodes in contact with $RuHex^{3+/2+}$ to determine whether or not the presence of HER catalyst significantly influenced the PEC behavior. $RuHex^{3+/2+}$ was a useful redox couple for this study due to its relatively negative formal potential, resulting in similar rectification to that of the hydrogen couple. Also $RuHex^{3+/2+}$ is quite stable under aqueous conditions, and it is highly transparent toward visible light in both its oxidized and reduced forms. Results for j–E measurements of p-WSe_2 in contact with $RuHex^{3+/2+}$ are shown in Figure 4.15. The j–E behavior in this redox couple was strikingly similar to that observed for hydrogen evolution, with observed V_{oc} values and photocurrents at 100 mW cm^{-2} only slightly smaller than that observed for hydrogen evolution in H_2SO_4 solution.

The lower V_{oc} values for p-WSe_2 in Ru hexammine can be attributed to the

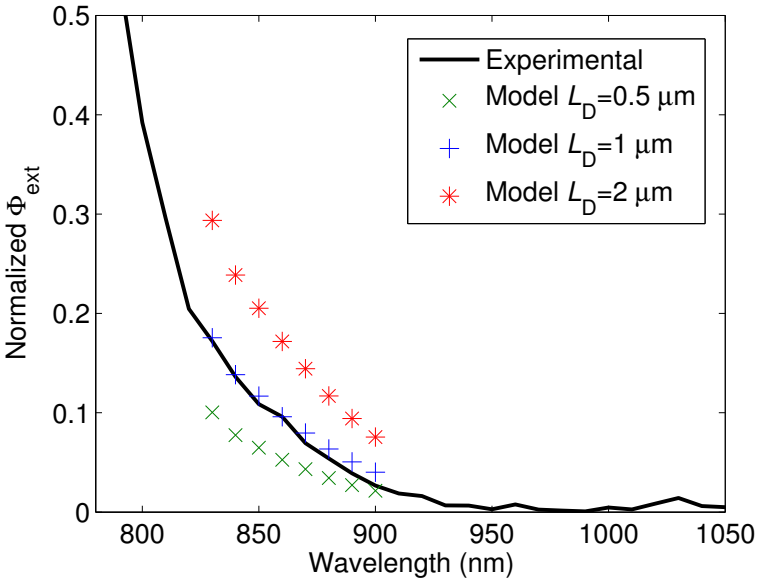

Figure 4.14. Detail of the spectral response data from Figure 4.13 normalized to the maximum Φ_{ext} value. Overlaid is a Gärtner model of the expected Φ_{int} values for a WSe_2 electrode with the noted L_D values over the spectral range from 825 to 900 nm. The model at $L_D = 1$ μm clearly shows the best fit to the experimental data. From McKone et al.[53] Copyright 2013 the American Chemical Society; used with permission.

slightly more positive $E^{0'}$ (-0.1 V vs. SCE) of the Ru couple compared with E_{RHE} in 0.5 M H_2SO_4 (-0.24 V vs. SCE), resulting in a slightly smaller barrier height and photovoltage. The lower photocurrent, however, was surprising, especially considering the fact that this p-WSe_2 electrode was not coated with a layer of catalyst. However, the light intensity dependence showed that the photocurrent increased by less than a factor of two with doubling the light intensity from 50 to 100 mW cm^{-2}, and again with a second doubling to 200 mW cm^{-2}. This result suggests that some of the dimished photocurrent was due to mass transport limitations or concentration overpotentials in the case of $RuHex^{3+/2+}$.

Finally, we carried out Mott-Schottky measurements to determine the p-WSe_2 band edge positions as a function of pH. Mott-Schottky data were collected using electrochemical impedance spectroscopy (EIS) in ferricyanide/ferrocyanide solutions at pH 2.5, 6.6, and 10.2. Representative results from two different photoelectrodes, each of which exhibited considerably different surface morphology, are shown in Figure

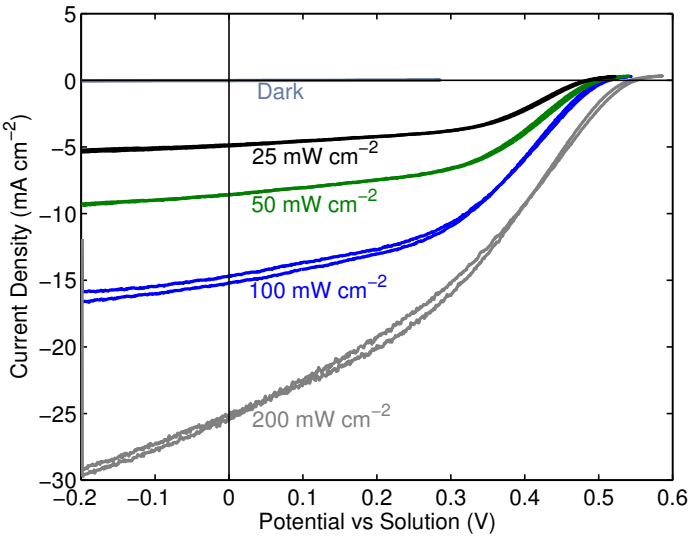

Figure 4.15. PEC j–E data for a representative p-WSe_2 crystal under illumination in $RuHex^{3+/2+}$ solution. The electrolyte was N_2-purged 50 mM $Ru(NH_3)_6Cl_3$ with 0.5 M KP_i supporting electrolyte buffered to pH 2.25 and electrolyzed between a porous carbon working electrode and fritted Pt counter electrode so as to produce $E_{oc} = -0.1$ V vs. SCE at a glassy carbon electrode. The counter electrode was a Pt mesh contained in a separate fritted compartment and the reference was a glassy carbon electrode poised at the solution potential. Illumination was provided by a tungsten-halogen lamp calibrated to 100 mW cm^{-2} and attenuated by adding or removing OD 0.3 neutral density filters. From McKone et al.[53]

4.16. For electrodes exhibiting highly pristine surface morphologies, the flat band potential did not significantly shift with pH. For electrodes with considerable density of surface defects and step edges, however, the band edges remained largely fixed from acidic to neutral pH values, but shifted in the negative direction from neutral to alkaline pH.

Statistical data for Mott-Schottky results from 9 different p-WSe_2 electrodes are shown in Figure 4.17. The electrodes fell into two distributions, corresponding to whether or not the flat band potentials shifted significantly from neutral to alkaline conditions. These two populations were highly correlated with surface morphology, where electrodes with smoother surfaces uniformly corresponded to the population exhibiting low pH-dependence.

Most classical semiconductors, such as Si and TiO_2, exhibit negative shifts in their flat-band potential with increasing pH.[162,165] This effect is due to changing the state of protonation or hydroxylation of the semiconductor surfaces in aqueous solution, resulting in static dipoles that shift the band edges in the same direction as the HER and OER (i.e., negative on the electrochemical scale with decreased H^+ activity). We intepret the absense of such a shift in p-WSe_2 to its a highly inert exposed Van der Waals surface resulting in only weak interactions with solution species such as H^+ and OH^-. This also explains why p-WSe_2 electrodes with stepped or defective surfaces exhibited some band edge shift, as the steps and defects are much more reactive toward solution species. Our observations are quite similar to those of Lewerenz et al., who also observed essentially no flat-band potential shift for WSe_2 electrodes with pristine surfaces, but large shifts for electrodes with stepped surfaces.[143]

4.6 Complete Picture of p-WSe_2

All of the previously described characterization allows us to develop a complete picture of the bulk and interfacial behavior of p-WSe_2 photoelectrodes. First, p-WSe_2 crystals grown by the CVT method with Nb dopant are high quality semiconductors. That is, the inherent properties of the semiconductor (e.g., band gap, carrier lifetime, mobility,

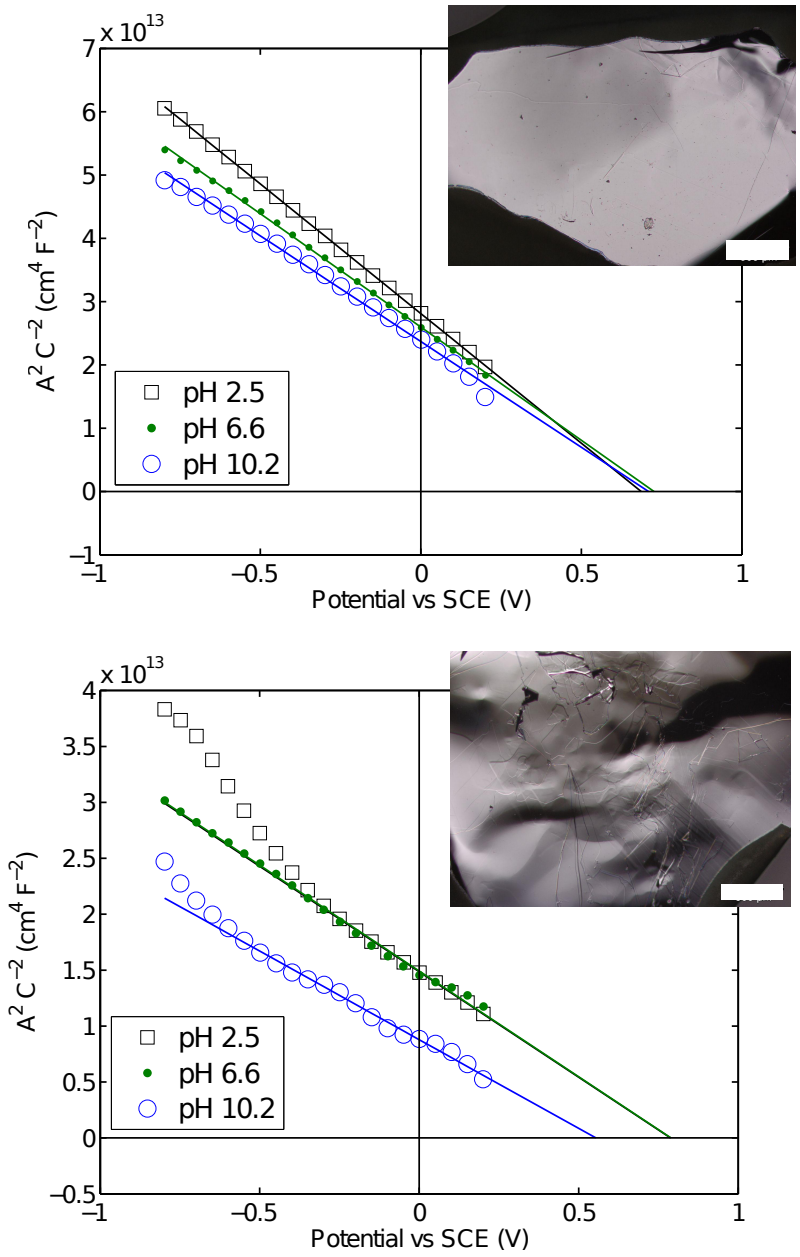

Figure 4.16. Mott-Schottky data and optical micrographs (insets; scale bars 0.5 mm) for two p-WSe_2 photoelectrodes representative of results obtained for pristine (top) and highly stepped (bottom) surfaces. Data were collected in 0.2 M $Fe(CN)_6^{3-/4-}$ solution with equal concentrations of the oxidized and reduced forms. Potassium phosphate was used as the supporting electrolyte and buffered to the noted pH values. Potentials were poised potentiostatically over a range from −0.8 to +0.2 V vs. SCE with a 10 mV RMS amplitude AC voltage overlaid at a frequency of 100 kHz. From McKone et al.[53] Copyright 2013 the American Chemical Society; used with permission.

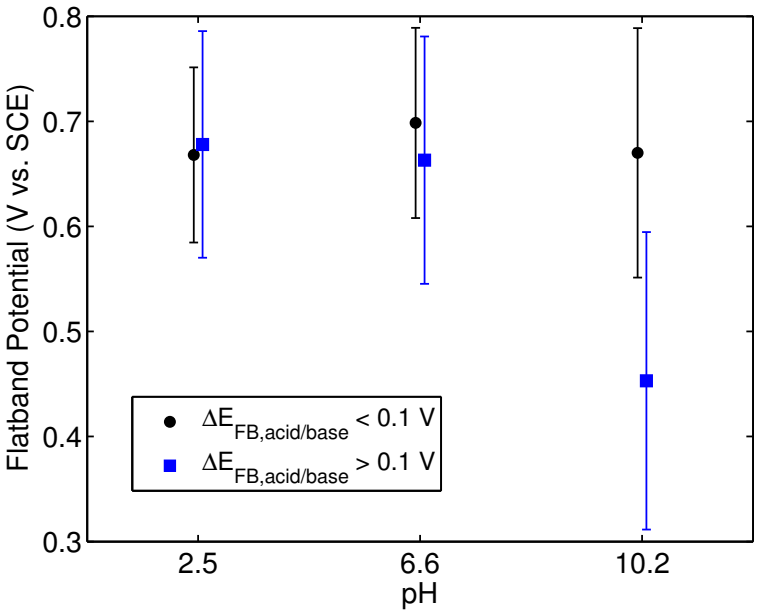

Figure 4.17. Flatband potentials calculated for a set of 9 p-WSe_2 photoelectrodes from Mott-Schottky measurements in $Fe(CN)_6^{3-/4-}$ solution. The data show two populations corresponding respectively to small and large negative shifts in flatband potential at high pH values. From McKone et al.[53] Copyright 2013, the American Chemical Society; used with permission.

etc.) allow for efficient solar energy conversion, and crystals synthesized by CVT can be sufficiently low in defects and impurities to exhibit these favorable properties. Second, the energetic relationships between the band edges of p-WSe_2 and E_{RHE} in aqueous solutions at all pH values are such that a large rectifying barrier is formed, which allows for generation of a large photovoltage for the HER. Notably, this large photovoltage is obtained without using only a liquid junction, compared to p-Si that requires a metallurgical n^+ emitter layer to obtain a high photovoltage.

Figure 4.18 shows a proposed representation of the relationship between the band edge positions of a pristine (free of surface defects) p-WSe_2 crystal and the hydrogen redox couple, alongside that of a hypothetical semiconductor exhibiting the same band gap and doping as p-WSe_2, but with surface properties like that of TiO_2. As the solution is made more alkaline, the "TiO_2" band edges shift along with E_{RHE}, resulting in the same value of ϕ_{bi}, and thus the same obtainable V_{oc} regardless of pH. Alternatively, a pristine p-WSe_2 photoelectrode exhibitis negligible band edge

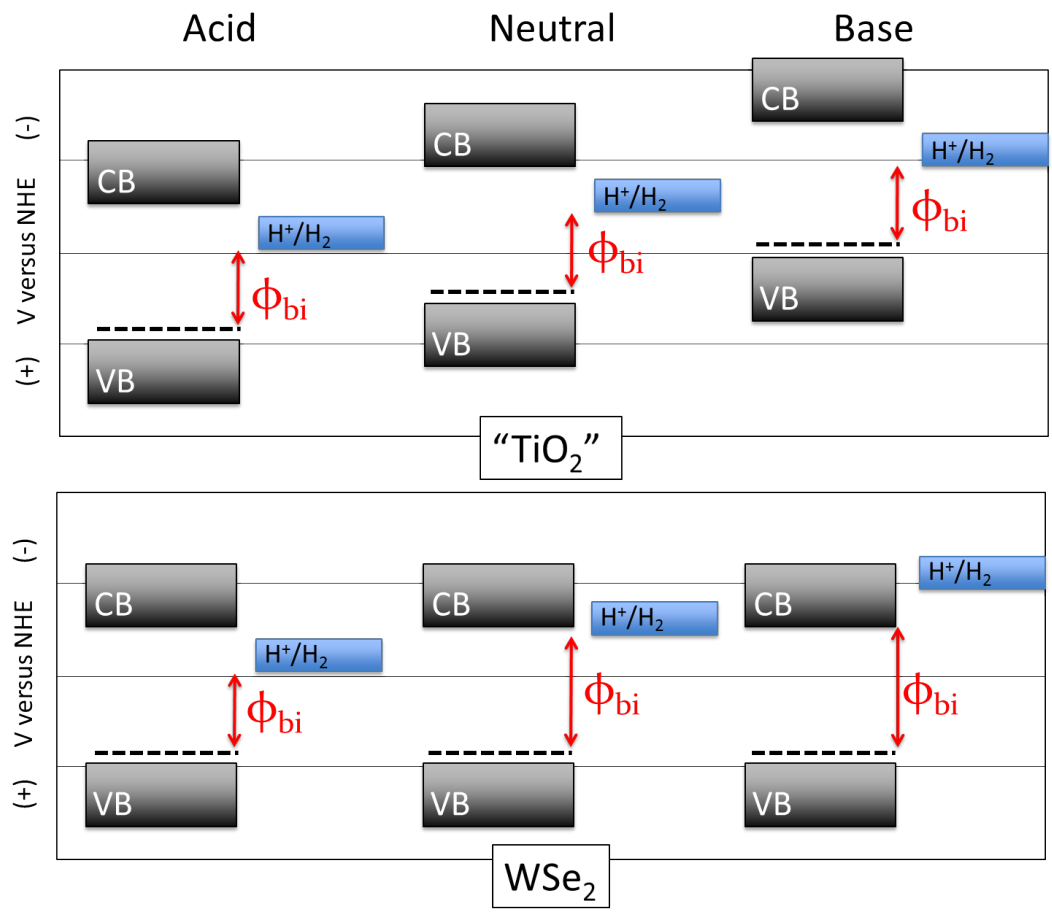

Figure 4.18. Schematic depiction of the pH-dependence of the band edge positions, on an electrochemical scale, for a hypothetical p-type semiconductor analogous to TiO_2 (top) and for a p-WSe_2 electrode with a pristine surface (bottom). In the case of p-WSe_2, unlike TiO_2, the band edges do not shift with pH, resulting in progressively increased built-in potentials (red double-headed arrows) with increasing pH.

shifts with pH, even as E_{RHE} moves more negative. Thus with increased pH, the ϕ_{bi} and the obtainable V_{oc} for the p-WSe_2 electrode increases to a maximum along with formation of a strong inversion layer. Alternatively, it is possible that the maximum obtainable V_{oc} for p-WSe_2 is pinned by surface states that are somewhat positive (on the electrochemical scale) of the conduction band edge. However, we observed photovoltages for p-WSe_2 photoelectrodes toward the HER of ~650 mV at pH 4.25. When compared with a bandgap of ~1.2 eV, these large photovoltages imply that the maximum ϕ_{bi} is limited either by the band edge or surface states very close to the band edge.

An important implication from the band edge analysis is that neutral or alkaline pH values are more favorable than acidic ones for efficient hydrogen evolution from p-WSe_2. In fact, the maximum attainable photovoltage for this semiconductor in contact with any redox couple or a solid contact results from simply placing it in contact with neutral or alkaline water. Additionally, the strong inversion layer formed on contact with even mildly acidic solution apparently results in increased photocurrent yields (as in Figures 4.9 and 4.10), perhaps due to diminished recombination as has been reported previously for Si electrodes.[166–168] As a result, I argue that this semiconductor is an ideal photocathode for alkaline or neutral water electrolysis.

Consistent with the results of previous researchers, a significant quantity of defects or step edges on the crystal surface significantly diminished the energy conversion efficiency of our p-WSe_2 photoelectrodes. We conclude, as other have, that these defects and edge sites facilitate recombination and/or disrupt the formation of a space-charge region.[130] Also, the presence of even a relatively small quantity of step edges, insufficient to completely diminish the activity of the photoelectrodes, significantly changes the pH-dependence of the band edge positions. Stepped crystal surfaces exhibit significant negative shifts of the band edges as the solution is made more alkaline, especially above neutral pH. However, this effect does not appear to negate the benefit of using neutral or alkaline aqueous solution rather than strongly acidic solution for the HER.

Pristine crystals of p-WSe_2 were rather stable toward corrosion under cathodic conditions in aqueous solutions over at least the timescale of hours. Nevertheless, during stability measurements in MV^{2+} solution, the photoelectrodes exhibited a small amount of diminished photocurrent along with the appearance of some cracks or line defects on the crystal surface. Slow etching of the crystal surface cannot be ruled out as a degradation mechanism. We conclude that etching likely does occur at the crystal surface and proceeds predominantly or entirely at defects and step edges. In fact, the observed band edge shifts with increased pH in the case of stepped surfaces is indirect evidence of strong interactions between water and/or hydroxide and the non-basal planes of WSe_2. Based on data collected by Sourisseau et al. for WS_2

etching mechanisms,[163] slow etching of WSe_2 might proceed first by electrochemical reduction to W metal at edge sites, followed by chemical oxidation and eventual dissolution of the resulting tungsten oxides as tungstate. This hypothesis suggests that either very pristine WSe_2 surfaces must be obtained to allow for efficient and stable long-term operation, or that measures must be taken to stabilize the non-basal planes under operating conditions.

The prospects for moving forward on developing of p-WSe_2 for efficient solar hydrogen generation are clear and promising. Simply improving on our growth methods will likely result in purer materials, longer carrier lifetimes, and thus higher photocurrents, photovoltages, and better fill factors. Photovoltages for the HER are already quite high, and Figure 4.19 illustrates that there is significant "room to grow" in increased photocurrent yields. I have little doubt that these materials could obtain thermodynamically based energy conversion efficiencies toward the HER of 12–15%, comparable to the best that has been observed for InP photoelectrodes.[122,169]

In the context of long-term efforts to make p-WSe_2 viable as a photocathode for scalable solar water splitting devices, however, the path forward is less clear. The CVT growth methods that we used are expensive, wasteful, and time consuming. They likely cannot be scaled to provide a commercially viable supply of high quality p-WSe_2. Rather, scalable single crystal or thin-fim growth methods would need to be developed. Thin-film methods would almost certainly be more economical than single crystal growth, but the questionable stability of stepped WSe_2 surfaces toward corrosion may pose a signfiicant impediment toward use of polycrystalline material. Further studies on the fundamental limits of stability for p-WSe_2 under reducing conditions in aqueous acid and base are at least as important as improving lab-scale HER device efficiencies.

Perhaps the ideal strategy for generation of efficient, scalable chalcogenide HER photocathodes would involve thin-film synthetic methods analogous to the well-known VLS method for high-aspect ratio Si structures.[115] The key outcome of these growth strategies is that the resulting films consist of arrays of microscopic single crystals, as opposed to the continuous films of randomly-oriented polycrystals used in current-

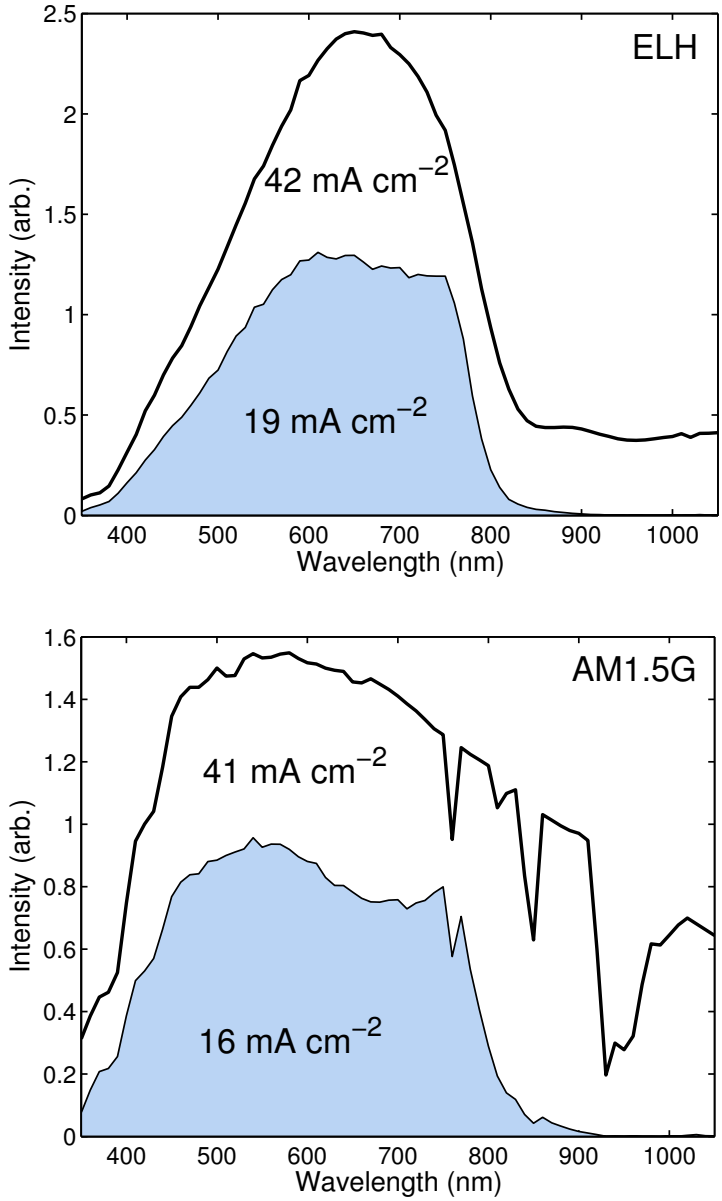

Figure 4.19. Comparison of photocurrents for p-WSe_2 using the ELH-type tungsten-halogen bulb spectrum (top) compared to the standard AM1.5G spectrum (bottom). The j_{ph} expected from p-WSe_2 photoelectrodes under each light source, based on the spectral response data in Figure 4.13, are shown in the shaded areas, and the theoretical maximum j_{ph} are shown outside the shaded areas. From McKone et al.[53] Copyright 2013, the American Chemical Society; used with permission.

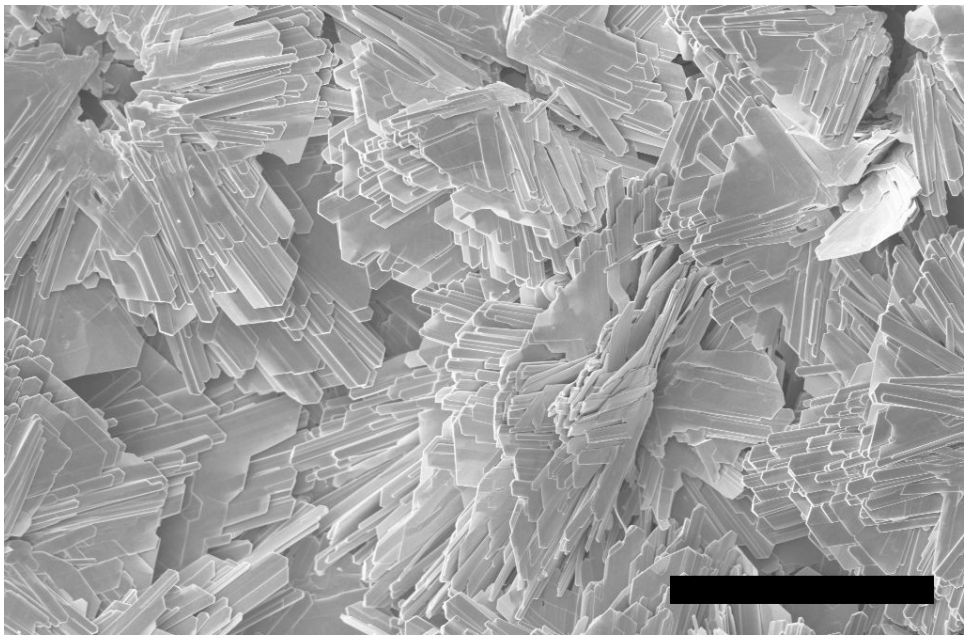

Figure 4.20. Scanning electron micrograph of the powder that results from heating together tungsten metal with Na_2S and pure S under inert gas. Scale bar is 20 μm.

generation thin film solar absorbers (CdTe and CIGS).[147,148] Access to arrays of microscopic chalcogenide single crystals might enable engineering of their morphology to allow for absorption and charge-carrier separation near basal planes and catalysis on edge sites. Alternatively, arrays of self-similar microcrystals would allow for development of systematic strategies to passivate recombination or corrosion at exposed edge sites.

Chalcogenide absorbers can, in fact, be synthesized as thin films using low temperature, atmospheric pressure methods. Figure 4.20 shows a scanning-electron micrograph of WS_2 microcrystals synthesized by a very simple flux-growth technique from W metal and Na-polysulfide at 800 °C and flowing Ar gas at atmospheric pressure, adapted from literature methods.[170–172] Notably, the individual crystallites in this sample apparently extended to well over 10 μm in length, which is comparable to the absorption depth for photons near the WS_2 band edge. There is every reason to continue work on single crystal characterization as well as novel polycrystal or thin-film growth methods for this promising class of materials.

Chapter 5

Summary and Conclusions

A decade ago it was not clear whether earth-abundant catalyst could be used for integrated PEC hydrogen evolution. In the last five years we have developed two candidate materials, Ni–Mo and Ni_2P, both of which are highly abundant and easily synthesized. We showed that Ni–Mo can be coupled successfully to Si light absorbers to drive the HER under illumination in acidic solutions. Although the acid stability of Ni–Mo is low, Ni_2P appears to be quite stable under strongly acidic conditions, and the similarity in synthesis and processing methods used for Ni_2P compared with Ni–Mo nanopowders suggests that Ni_2P will also be amenable for use in Si microwire hydrogen evolving photocathodes.

Researchers from Brookhaven National Lab recently reported a Ni–Mo catalyst that incorporates nitrogen to greatly improve the stability under acidic conditions.[114] Several of our colleagues and collaborators have also shown in the last 5–7 years that MoS_2 materials are efficient HER catalysts, and that they are quite stable in acid.[102,103] They similarly demonstrated photoelectrochemical hydrogen evolution under illumination when MoS_2 films were deposited onto Si electrodes.[121] In less than a decade this field has gone from no clear catalyst options to multiple promising material sets for earth-abundant PEC hydrogen evolution in acid and base.

Using Ni–Mo we demonstrated that non-noble HER catalysts, in spite of being lower in fundamental activity than their noble counterparts, are "good enough" to drive PEC hydrogen evolution with minimal wasted energy as overpotential. However, we identified several important general limiations for the use of non-noble catalysts

with semiconductor photocathodes. First, catalysts composed exclusively of non-noble metals are not likely to be stable in acid, and therefore they are only viable for use in alkaline electrolysis systems. In response to this limitation, we identified a promising semiconductor material, p-WSe_2, that exhibits very high HER energy conversion efficiencies and good aqueous stability over a wide range of solution pH. With further effort, this absorber could emerge as a leading candidate for use in water splitting devices.

A second limitation for use of non-noble HER catalysts in PEC hydrogen evolution is that a large mass of catalyst must be used in order to provide a sufficient turnover rate to keep up with the photocurrent provided by a light absorber. As a result, any sunlight incident directly on the catalyst layer is likely to be lost, due to the highly absorbing nature of essentially all HER catalysts. In reponse to this difficulty, we propose a new design for earth-abundant catalysts and semiconductor light absorbers, whereby the catalyst can be "hidden" under a layer of light scattering material at the base of an array of high aspect ratio absorber pillars. This approach in turn provides a unique rationale for the continued use of high aspect ratio strucutures, such as Si microwire arrays, as light absorbers in solar water splitting schemes.

To conclude, Figure 5.1 shows a widely touted time vs. efficiency plot from the National Renewable Energy Lab, illustrating the indellible progression of photovoltaics toward its modern maturity as a technology. Bearing in mind that the first photovoltaic cells were demonstrated in the 1950s, I believe that solar water splitting is only now where PV was in 1975—on the cusp of a renaissance that will eventually culminate in mature, viable technologies. I am very excited to see what emerges from this field in the coming years!

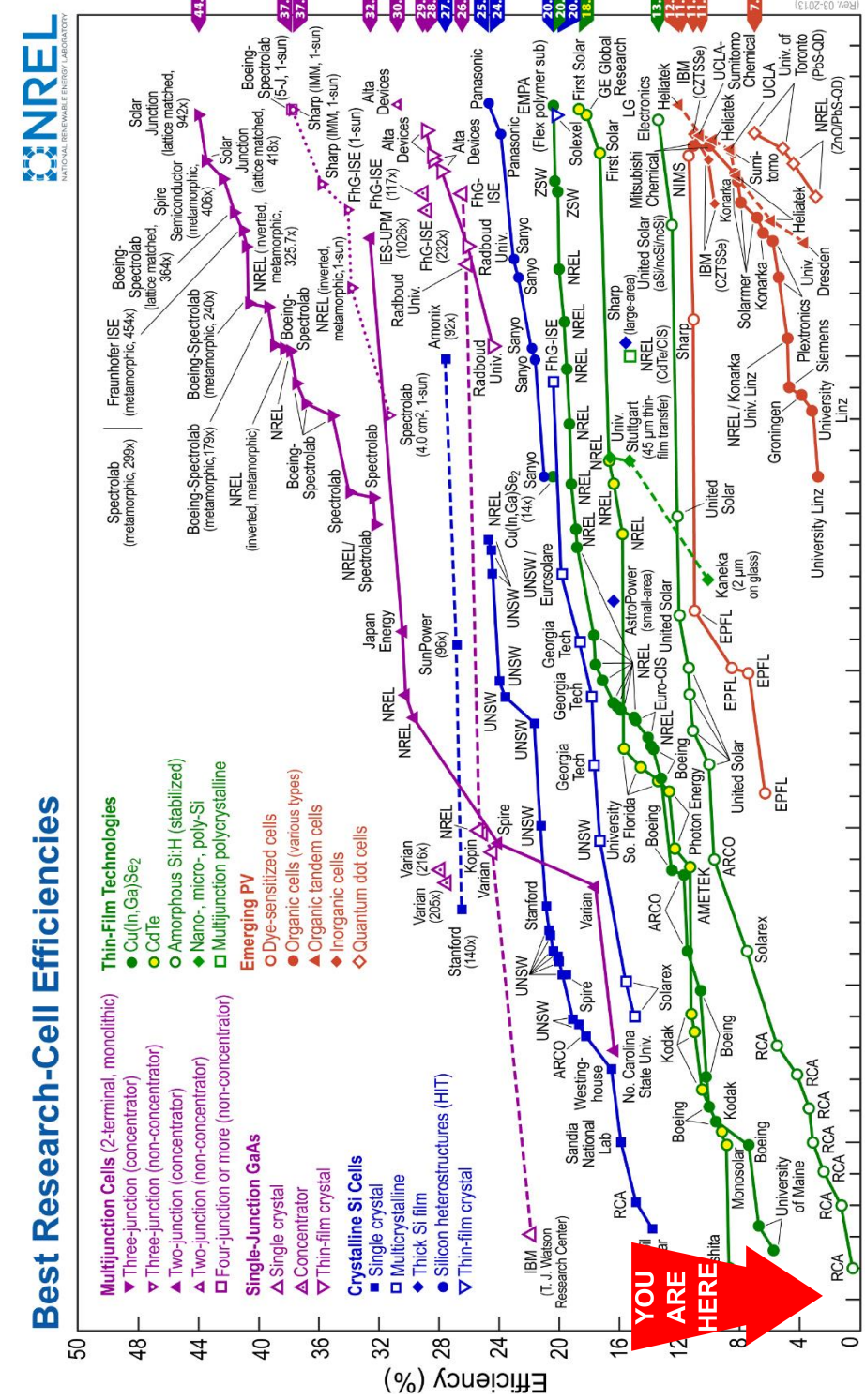

Figure 5.1. Plot of energy conversion efficiency vs. time for commercial and heavily researched solar photovoltaic technologies. From the National Renewable Energy Laboratory National Center for Photovoltaics.[173] The arrow labeled "you are here" is intended to imply that PEC water splitting is now reaching a maturity level similar to that of the PV industry around 1975.

Appendix A

List of Symbols, Abbreviations, and Their Meanings.

The following is a list of symbols and abbreviations used in this dissertation and their associated meanings.

[A]	concentration of species A
AM1.5G	global standardized air-mass 1.5 solar spectrum
b	Tafel slope
CV	cyclic voltammetry or cyclic voltammogram
CVT	chemical vapor transport
DCE	deposition current efficiency
DFT	density functional theory
E	potential (e.g., volts)
E^0	equilibrium (Nernst) potential under standard conditions
$E^{0'}$	equilibrium (Nernst) potential under non-standard conditions
e^-	electron
E_{cb}	conduction band edge energy
EDS	energy dispersive spectroscopy

E_f	Fermi energy
E_{fb}	flat band potential
E_g	band gap energy
EIS	electrochemical impedance spectroscopy
E_{mp}	electrochemical potential at the maximum power point
E_{oc}	open-circuit electrochemical potential
E_{RHE}	formal potential for the hydrogen evolution reaction
E_{vb}	valence band energy
f	F/RT
F	Faraday constant
ff	fill factor
FTO	fluorine-doped tin oxide
GDL	gas-diffusion layer
h^+	hole
HER	hydrogen evolution reaction
$h\nu$	photon
i	current (e.g., amperes)
i_0	exchange current
j	current density (e.g., A cm^{-2})
j_0	exchange current density
j_{mp}	current density at the maximum power point
j_{ph}	photocurrent density
j_{sc}	short-circuit current density
k_0	intrinsic rate constant
KHP	potassium hydrogen phthalate
KP_i	potassium phosphate
L_D	effective minority carrier diffusion length

MEA	membrane electrode assembly
MO	molecular orbital
MV	methyl viologen
NR	no reaction
OD	optical density
OER	oxygen evolution reaction
PEC	photoelectrochemistry or photoelectrochemical
P_{in}	incoming light intensity (power per area)
P_{max}	maximum power output
PTFE	polytetrafluoroethylene
PV	photovoltaic or photovoltaics
q	unsigned electronic charge
R	ideal gas constant
RHE	reversible hydrogen electrode
RTA	rapid thermal annealing
SEM	scanning electron microscope
SOD	spin-on dopant
T	temperature
TEM	transmission electron microscope
UV	ultraviolet
V	voltage
V_{mp}	voltage at the maximum power point
V_{oc}	open-circuit photovoltage
W	depletion width
XPS	X-ray photoelectron spectroscopy
α	absorption coefficient or electrochemical symmetry factor
γ	roughness factor
ΔE	electrochemical potential difference

ΔG	free energy change
η	solar energy conversion efficiency or overpotential
Φ	quantum yield
ϕ_{bi}	built-in potential

Appendix B

Tutorial on Characterization of HER Electrocatalysts and Photoelectrodes

B.1 Hydrogen Evolution Electrocatalysts

B.1.1 Theoretical Considerations

This section treats the relevant theory and equations governing heterogeneous electrochemical hydrogen evolution. The material has been split into sections on thermodynamics and kinetics. Much more detailed discussions of electrochemical thermodynamics, kinetics, and the HER in particular are available in several useful texts.[65,96,174,175]

Thermodynamics

Electrocatalytic hydrogen evolution is a two-electron process involving the net reduction of two proton equivalents to H_2(g). The equation can be expressed generally as in B.1

$$2\,HA + 2\,e^- \longrightarrow H_2 + 2\,A^- \tag{B.1}$$

where HA is a Brønsted acid and A^- is its conjugate base. In aqueous acidic solution, HA and A^- are predominantly H_3O^+ and H_2O, respectively. In aqueous alkaline solution, HA is H_2O and A^- is OH^-. The Nernst equilibrium behavior of reaction

B.1 can be expressed in terms of B.2

$$E = E^0 - \frac{RT}{2F} \ln \left(\frac{[\mathrm{H_2}]}{[\mathrm{H^+}]^2} \right) \tag{B.2}$$

where all of the symbols have their standard meanings in electrochemistry. It is clear from the Nernst equation that the equilibrium potential for hydrogen evolution is dependent both on the pH and the concentration of hydrogen gas dissolved in the electrolyte.

For any pH and $[\mathrm{H_2}]$ one can define a Nernst potential $E^{0'}$ for the hydrogen evolution equilibrium relative to an arbitrary electrochemical reference potential. The Nernst potential is also sometimes called the formal potential, the solution potential, or the equilibrium potential. It is, by definition, the potential at which the reaction is at equilibrium, and thus an electrode poised at the solution potential will not pass net current to the solution. It is important for later discussion of experimental considerations to note that without a well-defined $[\mathrm{H_2}]$, the $E^{0'}$ for hydrogen evolution is also not well defined. For the specific case where the solution is saturated with $\mathrm{H_2}$ at a pressure of 1 atm, the $E^{0'}$ at any pH can be expressed as the reversible hydrogen electrode potential E_{RHE}. A convenient rule of thumb is that E_{RHE} shifts by +59 mV per increased unit in aqueous solution pH.

Essentially all the key thermodynamic considerations for hydrogen evolution are contained in the balanced half reaction Equation B.1 and resulting Nernst equilibrium expression B.2. A full treatment of water splitting, however, requires consideration of the OER and the full redox reaction. The OER half reaction and full water splitting reactions are shown in Equations B.3 and B.4, respectively.

$$2\,\mathrm{H_2O} \longrightarrow \mathrm{O_2} + 4\,\mathrm{H^+} + 4\,\mathrm{e^-} \tag{B.3}$$

$$2\,\mathrm{H_2O} \longrightarrow 2\,\mathrm{H_2} + \mathrm{O_2} \tag{B.4}$$

The OER is also governed by a pH-dependent Nernst equilibrium which, at room temperature, also shifts at 59 mV per pH unit (ceteris paribus) in the same direc-

tion as the HER. The potential difference, ΔE, between the hydrogen evolution and oxygen evolution Nernst potentials remains fixed (again assuming constant product gas concentrations) at a given temperature. At room temperature, the ΔE for water splitting is 1.23 V, regardless of pH. This is a satisfying outcome, as the net chemical change for water splitting is the same, regardless of pH. In fact, the ΔE for water splitting also represents the total free energy change (i.e., 1.23 eV per electron, or 4.92 eV per mol O_2, at 298 K) for net conversion of two water molecules to one equivalent of oxygen and two equivalents of hydrogen.

Kinetics

Conveniently, the HER is one of the most heavily studied and simplest electrochemical reactions. The kinetics of the HER have been treated specifically in several seminal papers.[54,55,176–178] An overview of these treatments follows.

Homogeneous and heterogeneous electrocatalytic hydrogen evolution kinetics are rarely described simultaneously, but in fact they are remarkably similar. Key mechanistic steps for the HER are shown in B.5–B.7:

$$\mathrm{HA} + \mathrm{e}^- + \mathrm{cat} \longrightarrow \mathrm{cat{-}H} + \mathrm{A}^- \tag{B.5}$$

$$\mathrm{HA} + \mathrm{e}^- + \mathrm{cat{-}H} \longrightarrow \mathrm{H_2} + \mathrm{A}^- + \mathrm{cat} \tag{B.6}$$

$$\mathrm{cat{-}H} + \mathrm{cat{-}H} \longrightarrow \mathrm{H_2} + 2\,\mathrm{cat} \tag{B.7}$$

where *"*cat*"* represents the homogeneous or heterogeneous catalytic reaction center. Hydrogen evolution is generally considered to go through either of two routes: Equation B.5 followed by B.6 or Equation B.5 followed by B.7. The main difference between the two mechanisms involves whether the H–H coupling step takes place at a single catalytic site or through multiple sites.

There are two additional considerations required for understanding homogeneous HER electrocatalysts. First, homogeneous catalysts are solution species, and so their concentrations and mass transport properties need to be considered explicitly. Second, electron-transfer steps for homogeneous electrocatalysis essentially always in-

volve discrete redox transitions from one oxidation state to another (e.g., Co^{III} to Co^{II}). These two relatively straightforward considerations result in significantly increased complexity for measuring and understanding the dynamics of homogeneous hydrogen evolution electrocatalysis, and so they are not treated any further here.

The simplest expression of heterogeneous electrode kinetics was advanced first in 1905 by Julius Tafel from studies including the HER.[176,179] It is known as the Tafel equation or the Tafel law:

$$i = i_0 \cdot 10^{\eta/b} \tag{B.8}$$

The Tafel law states that the observed reaction rate (which is proportional to the observed current, i, in electrochemistry through Faraday's law) is equal to an intrinsic rate described by a prefactor, i_0, multiplied by an exponential function of the overpotential, η, normalized to another characteristic constant, b. The prefactor i_0 is known as the exchange current, and it is related directly to the intrinsic electrocatalytic rate constant, k_0, which has a similar meaning to that for all chemical reactions. Put another way, i_0 is a measure of the equivalent rates of the forward and reverse reactions under dynamic equilibrium.

The variable η in the exponent of Equation B.8 is the overpotential, the difference between the applied potential and the Nernst equilibrium potential of the system of interest. Finally, the factor b is called the Tafel slope; it is a measure of the sensitivity of electrocatalyst turnover to an increase or decrease in applied overpotential.

The Tafel slope depends on the specific mechanism of the reaction of interest as well as the symmetry factor, α, for the activation barrier of the electrochemical process. Generally the symmetry factor is considered to be $\sim$0.5 for most electrochemical reactions, which causes, e.g., the HER to take on a limited number of possible b values. For example, for materials that generate weakly bound hydrides, the rate-determining step of the HER is the discharge step (Equation B.5), the equilibrium surface hydride coverage is low, and the expected b value is $RT/\alpha F$ or $\sim$120 mV decade^{-1} at room temperature for $\alpha = 0.5$.[178] Using these kinetic relationships the Tafel slope may be

used as a cursory assessment of the rate-determining step of the HER.

Heterogeneous hydrogen evolution kinetics can usually be analyzed according to the Tafel equation by measuring current flow under steady state conditions over a range of overpotential values and constructing a Tafel plot to identify i_0 and b. An example of a Tafel plot is shown in Figure 2.21 on page 58. The traditional method of constructing a Tafel plot places $\log(i)$ on the absicca and η on the ordinate, which accounts for naming b the Tafel slope. This was the logical approach for plotting the i–η response in Tafel's era, since electrochemistry apparatus at that time controlled current as the independent variable and measured potential as the dependent variable.

The observed i_0 is dependent on the electrochemically active surface area of the material of interest. It is generally normalized to the macroscopic area of the electrode and expressed as an exchange current density, j_0. Even with this normalization, however, it is not appropriate to use exchange current density as a critical metric for HER kinetics unless all the materials under consideration have known absolute or relative electrochemically active surface areas. This is not a common condition, and so Tafel slope is arguably better as a single metric for whether one catalyst is "inherently" better at the HER than another. Even better, however, is the use of both j_0 and b along with some measure or estimate of electrochemically active surface area for all of the catalysts under consideration.

Under certain conditions, the Tafel law does not sufficiently describe the observed electrochemical kinetic behavior. This is true, for example, at very low η values ($\eta < 100$ mV or so). The reason for the discrepancy is that the Tafel law assumes the reverse reaction rate is small compared to the forward rate, and so the former can be ignored. As a result, the Tafel law breaks down at low η and must be replaced by the more complex Butler-Volmer kinetic expression:

$$j = j_0 \left[e^{-\alpha f \eta} - e^{(1-\alpha) f \eta} \right] \tag{B.9}$$

where $f = F/RT$. Each of the exponential factors in Equation B.9 is an expression of the Tafel Law in the forward and reverse directions, respectively. More detailed

discussons of Butler-Volmer kinetics are available elsewhere.[96,174] Importantly, electrode kinetics that follow the Butler-Volmer equation will exhibit non-linear behavior over some range of overpotentials when placed on a Tafel plot. Indeed, this is exactly what we observed for Ni–Mo nanopowder electrocatalysts with high mass loading, as discussed in Chapter 2.

B.1.2 Experimental Considerations

The best apparatus for electrochemical testing of hydrogen evolution electrocatalysts is a three-electrode cell, preferably with a separate compartment for the counter electrode. The operating principles of a potentiostat and three-electrode measurements are discussed in detail in Bard and Faulkner.[96] I have treated each of the electrodes, the cell/electrolyte composition, and instrument protocols separately in the following.

Working Electrode

The most important characteristics of the working electrode are that it is mechanically stable, chemically stable, electrically conductive, and that the substrate (if used) exhibits minimal background current. Electrode materials may range from metallurgical samples to pressed or sintered powders to thin films. In some cases, the active electrode material is deposited onto a substrate. Mechanical stability means, for example, that pressed or sintered powders do not lose mass due to disintegration. Chemical stability is also important, as materials that degrade or corrode quickly (e.g., in less than a few minutes) will not give reproducible behavior in an electrochemical cell.

With regard to conductivity, some electrocatalyst materials are not metallic conductors. These materials are best studied either deposited onto conductive substrates as very thin films or otherwise supported on a porous conducting network. Carbon black, for example, is used ubiquitously for PEM fuel cells and electrolyzers to support Pt catalysts and allow for high conductivity even at very low Pt catalyst loadings. It is important, however, to make some effort to quantify at least the mass, or ideally the active surface area, of any electrocatalyst material before and after testing.

Another key factor is ensuring that the working electrode substrate exhibits litle to no background catalysis. A good rule of thumb is that if electrocatalytic activity is not easily discernible without a "baseline correction" of the substrate response, something should be done to increase the relative activity of the catalyst above that of the substrate. Some strategies might include increasing the mass loading or changing the substrate material to one with lower intrinsic activity (glassy carbon and degenerately doped Si are good options). If the catalyst does not show significant activity above, e.g., a glassy carbon background at any loading, that catalyst is not likely of interest for hydrogen evolution.

Counter Electrode

The identity and placement of the counter electrode is a difficult but important consideration for testing hydrogen evolution electrocatalysis. The inherent assumption of a three-electrode experiment is that the counter electrode does not contribute materially to the observed behavior at the working electrode. Nevertheless, this condition can be difficult to realize, especially under conditions where large currents are flowing (which is itself a desirable case, as it corresponds to active electrocatalysis).

In general, the counter electrode must be composed of a material that will not degrade significantly under anodic bias. Unfortunately, it is not possible to completely supress anodic corrosion, especially in acidic solution. Even Pt electrodes are known to slowly corrode under anodic bias in acid. Figure B.1 demonstrates an example of what occurs when Pt ions that slough off of a Pt counter electrode over time encounter a working electrode undergoing continuous hydrogen evolution testing.

The observed improvement in electrocatalysis over time was initially ascribed to an activation process where dissolved molybdate and tungstate species deposit onto the working electrode.[47] However, as is clear from Figure B.1, the improvement in activity is significantly reduced by removal of the Pt counter electrode. This is a clear sign of Pt contamination, which actually causes the apparent electrocatalysis to improve over time. Any researchers interested in HER electrocatalysis should be wary of reports describing improvement in activity over time, especially if the counter

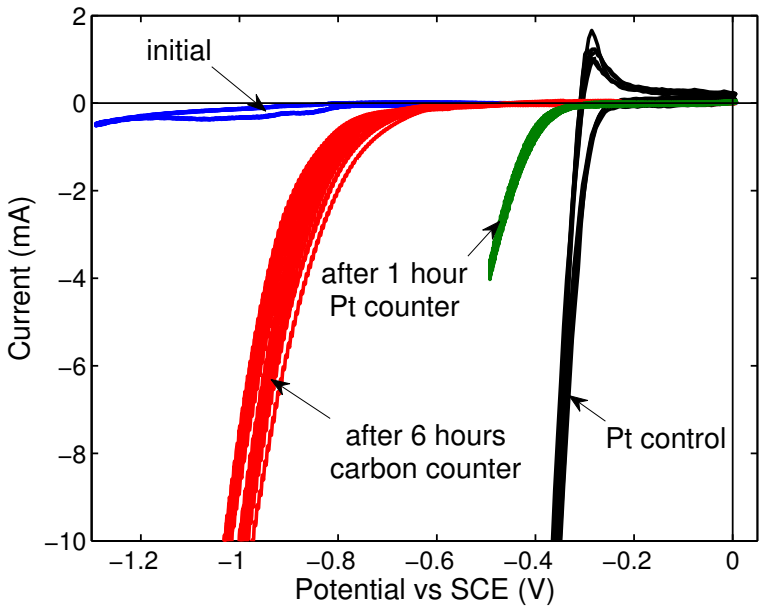

Figure B.1. Cyclic voltammograms of glassy carbon electrodes undergoing deposition with a heterogeneous polytungstate film. Films were formed by electrolyzing a solution of 0.5 mM phosphotungstic acid in 0.5 M H_2SO_4 in a single chamber electrochemical cell using either a carbon or Pt counter electrode over a given interval, as labeled.

electrode material is Pt or not reported.

The best conditions that we have found for testing HER activity in acid mimics the conditions of commercial PEM electrolysis systems. The working electrode compartment is separated from a counter electrode compartment by an o-ring joint containing a piece of ion-exchange membrane such as Nafion. This membrane is highly selective for transport of protons over larger cations. The counter electrode may then be composed of either a highly inert carbon material, such as metallurgical graphite or boron-doped diamond, or even noble metals such as Pt, Ir, or Ru. The ion-exchange membrane serves to prevent crossover of dissolved metal ions or oxygen gas, both of which will influence the observed kinetics of the working electrode.

If using noble metals or their oxides as counter electrode materials, it is important to regularly run control experiments demonstrating that the working compartment is not being contaminated by noble metal ions over the timescale of the experiment. The best way to run these controls is to prepare a clean working electrode with poor catalytic activity, such as glassy carbon or degenerately doped Si, and to poise the electrode at a potential where it produces a significant quantity of hydrogen for at least several minutes, if not hours. If the activity of this working electrode does not significantly increase over this timescale, the solution can be considered clean enough for testing the catalyst materials of interest.

Other helpful rules to follow with counter electrodes in acid solution are to ensure that they are physically large compred to the working and that they do no stay in solution for longer than necessary. Having a large surface area for the counter electrode ensures that the actual current densities passed are much lower than at the working electrode. This way the potential applied to the counter electrode will also not be overly oxidizing and anodic corrosion will be minimized. Similarly, leaving the counter electrode in solution for as short a time as possible ensures minimization of chemical (as opposed to electrochemical) corrosion. The counter electrode should be placed in solution immediately before the working electrode and removed immediately after testing is complete.

Under neutral or alkaline conditions, noble metal dissolution is less of an issue, due

to low solubility for the noble metals under these conditions. Under strongly alkaline conditions, even non-noble metals such as Ni can be used as counter electrodes, as they form insoluble Ni oxide and hydroxides and generate O_2 under anodic bias. Nevertheless, the best practice even under alkaline conditions is to use a suitable frit or membrane separator, which must be compatible with the electrolyte, in order to avoid crossover of metal ions or oxygen to the working compartment.

Reference Electrode

Thankfully, reference electrodes of every major type are readily available through commercial suppliers. For hydrogen evolution testing, the best protocol is to use a reference electrode whose filling solution matches that of the working compartment at least with respect to pH, if not also chemical composition. For example, for testing alkaline electrolysis at pH 14, a Hg/HgO electrode filled with 1M NaOH or KOH solution may be used. For testing acidic electrolysis in 1 M H_2SO_4, a $Hg/HgSO_4$ electrode filled with sulfuric acid solution may be used.

For testing at neutral or moderate pH (i.e., pH 2–12 or so), a saturated calomel electrode (SCE) or Ag/AgCl electrode maybe used. However, bear in mind that Hg and Cl^- can be sources of electrochemical contamination, so it is important that the fritted junction between the reference electrode and solution is sound and exhibits a negligibly low leak rate. I have found that the Dri-Ref line of Ag/AgCl reference electrodes from WPI, Inc. exhibit little to no contamination of the working compartment over rather long time periods.

Reference electrodes should not remain in the electrochemical cell once testing is complete. Rather they should be returned to their proper storage conditions. It is also important to ensure that the reference electrode potential is not drifting by standardizing it against a secondary reference electrode that is never used for experiments. If reference electrodes are found to drift more than a few mV over the course of some days, they should be refreshed or discarded.

A second consideration with reference electrodes is their physical separation from the working electrode. When the reference electrode junction is not very close to the

working electrode, the working electrode potential measurement is subject to an error that is proportional to the absolute current, called the uncompensated resistance. This effect has been described in more detail elsewhere.[96,180,181] Uncompensated resistance can be minimized by moving the counter electrode physically close to the working electrode, by using a Luggin capillary, or by decreasing the area of the working electrode.

My favored method, however, for HER studies is to account for the uncompensated resistance by use of the current-interrupt compensation technique. The details of current-interrupt compensation have been discussed elsewhere,[182,183] and the method has been incorporated as an selectable option in most modern digital potentiostats. The method can be easily verified by taking two consecutive Tafel measurements, one with and one without compensation. The two curves should overlay at low absolute currents, and then diverge by a value that is equal to the product of the instantaneous current and a constant factor, which is the uncompensated resistance.

Cell and Electrolyte

An appropriate electrochemical cell for HER experimentation is one that is as small as possible while still accommodating all of the necessary electrodes. Additionally, as previously mentioned, a cell incorporating a second compartment for the counter electrode separated by a fine porosity frit or o-ring joint with an ion-exchange membrane is generally important.

Regarding cell use for HER measurements under alkaline conditions, note that borosilicate glass is slowly etched in an alkaline environment. An acrylic or fluorocarbon polymer cell is preferable, especially for long-term testing. The same goes for materials in the working, counter, and reference electrode bodies. I found in testing Ni–Mo alloys that etching of a borosilicate glass cell and electrode bodies did not appear to perturb a longevity experiment lasting over 100 hours at room temperature in 2 M KOH. However, experiments carried out in glass over longer time periods, higher temperature, or more caustic conditions should be carried out cautiously. Shannon Boettcher has found significant Fe impurities in Ni oxide OER electrodes after long-

term testing under alkaline conditions in borosilicate glass.[184]

The most important characteristics of the electrolyte are that it is clean and maintains a stable composition over the course of the entire experiment. Strong acid or strong alkaline (>0.2 N acid or base equivalents) conditions are arguably the best for testing water electrolysis, due to the commercial usage of acid and alkaline electrolyzers, but some inorganic buffers (borate, phosphate, silicate) may be sufficiently inert and stable under milder pH conditions.

For any HER experimentation requiring reasonably exact measurements of overpotential the electrolyte must be continuously sparged with high purity H_2(g). This process ensures that the the solution remains saturated with H_2, even when additional gas is evolved at the working electrode; thus the Nernst potential for the HER remains well-defined throughout the measurement. Figure B.2 depicts the current-voltage behavior of clean Pt electrodes in sulfuric acid solution with and without H_2 saturation. In the case of the solution without H_2, the small quantities of H_2 initially produced by the Pt electrode increased the local concentration until it transiently reached the point of saturation. As a result, data collected without H_2 sparging gave large amounts of hysteresis near E_{RHE}. Conversely, the H_2-sparged solution gave no hysteresis and a very clear transition between the HER and hydrogen oxidation regions of the j–E response.

A clean Pt electrode can be used to measure explicitly E_{RHE} under the desired conditions. After sparging with H_2 for at least 10 minutes, a clean Pt electrode may be cycled over the potential region where its current transitions from cathodic to anodic. If the Pt electrode, solution, and H_2 sparge are clean and stable, the anodic-cathodic crossing point will be stable and exactly equal to E_{RHE} in the solution of interest, relative to the reference electrode. This is a particularly useful method for standardizing measurements across pH values. For Nernst potential measurement under neutral or alkaline conditions, a high surface-area platinized Pt electrode should be used in order to improve the otherwise slow equilibration kinetics. Also, in all cases the Nernst potential standardization should ideally occur after testing other catalysts in order to avoid potential contamination of the working electrode compartment with

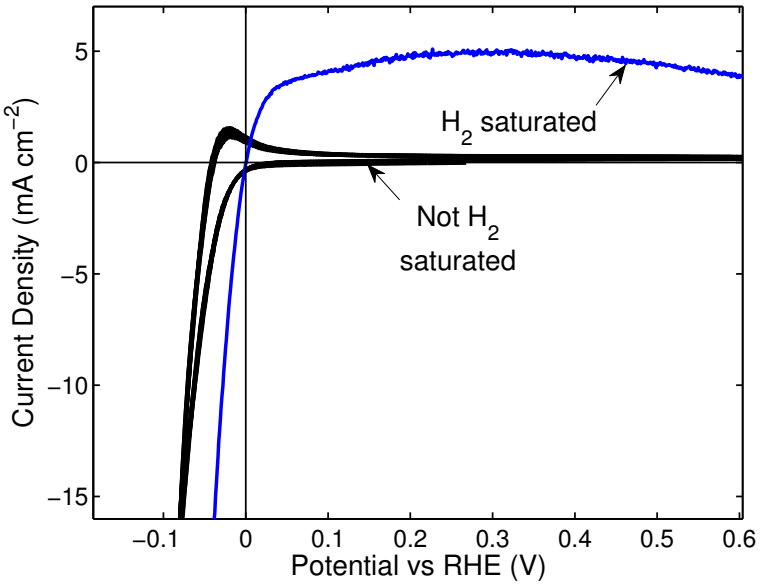

Figure B.2. Electrochemical j–E data for clean Pt electrodes around the RHE potential in 0.5 M H_2SO_4 solutions that have or have not been saturated with H_2(g).

trace Pt.

Another significant consideration for the solution is agitation. Generally heterogeneous HER measurements are easier to analyze in the absence of mass-transport effects. The solution should be agitated either through judicious use of a stir plate or stir motor, or even better by use of a rotating disk working electrode. Solution agitation also allows for dissolution of hydrogen from the sparging stream significantly faster.

Instrument Protocols

Tafel measurements should be carried out under steady state or pseudo-steady state conditions. The former involves holding the electrode at a set potential (potentiostatic) or current (galvanostatic) for as long as is required to observe a stable electrode potential. Pseudo-steady state measurements involve very slow potential sweeps (<5 mV sec^{-1}) so as to approximate the steady state condition. Pseudo-steady state measurements are, of course, significantly faster for a given potential range, but they should be standardized against true steady state measurements before they are relied

upon for quantitative analysis of kinetic phenomena.

Additionally, slow potential sweeps and steady state measurements should be carried out in ascending and descending directions with respective to overpotential. If the electrode kinetics are well behaved, the data collected in each direction should overlay. Cases where scans in both directions do not overlay may result from electrode instability or non-faradaic processes that interfere with the reaction of interest. In such cases the different results from each direction might be useful for understanding the dynamics of the catalyst.

As noted previously, the influence of uncompensated resistance should be considered, especially where non-linear Tafel behavior is observed at higher currents. Automatic or manual accounting for the uncompensated resistance might be attempted, or the distance between the working and reference electrode made be decreased in order to minimize the effect.

Special Considerations for Stability Measurements

Measurements of HER electrocatalyst stability can be particularly challenging, as small problems in electrode, electrolyte, or cell preparation can give rise to large changes over long times. First, it is extremely important that the electrolyte is rigorously free from adventitious contaminants. Acid electrolytes, in particular, tend to contain trace metal impurities due, e.g., to leachate from the reagent bottle or dissolution of airborn particles. One should take care to rely only the purest available reagents and/or undertake so-called "pre-electrolysis" efforts in order to ensure electrolyte cleanliness.[177]

Potentiostatic or galvanostatic measurements are both appropriate for long-term stability studies. Note that since current is an exponential function of applied overpotential, potentiostatic measurements will often give relatively larger variations in the measured quantity (current) over time compared to galvanostatic measurements. Put another way, a catalyst that appears to degrade by 50% in current over 100 hours at a constant potential may only degrade by 10% in overpotential over the same 100-hour interval at a constant current. Industrial electrolyzers also generally operate in a

galvanostatic fashion, so as to ensure a constant rate of production for H_2 gas. However, galvanostatic measurements are more dangerous for long-term measurements, as degradation of the electrode materials or mechanical degradation resulting in large cell resistances can cause the potentiostat to apply very large voltage biases between working and counter electrodes. Overnight galvanostatic experiments should not be carried out using instrumentation that does not have overload protection.

Another approach for testing longevity of HER electrocatalysts are accelerated degradation methods. These methods usually involve cycling the potential of candidate cathodes from negative to positive potentials so as to subject them to extreme reducing and oxidizing conditions. These studies have been correlated to true long-term stability in the case of Pt electrodes for electrolysis and fuel cells.[185] Accelerated degradation testing is particularly useful for an initial estimation of the ultimate stability of a cathode material. It can also be useful for eliminating the effects of electrochemical contaminants in stability testing, since cycling the potential tends to strip such contaminants from the surface. However, these studies should certainly be complemented by true longevity tests, especially for new materials for which the correlation between cycling stability and constant current/voltage stability is not well known.

B.2 Hydrogen Evolution Photocathodes

This section covers key aspects of measuring PEC hydrogen evolution using semiconductor light absorbers with or without surface-attached electrocatalysts. HER photoelectrodes can be approximated as a serial combination of a purely electrocatalytic material and an illuminated photodiode. The electrocatalyst component obeys essentially the same rules regarding thermodynamics and kinetics as described previously, but this behavior is convoluted with the properties of a photodiode. The following contains a short summary of the relevant physics and figures of merit for generic photoelectrodes, and then some discussion of the effect of convoluting electrode kinetics with photodiode behavior. For more information, detailed discussions

of the physics of solar cells are available in several highly regarded textbooks.[186,187] Also Roald Hoffman wrote a very accessible overview of solid-state physics from the perspective of a chemist.[188] Finally, a detailed review of semiconductor photoelectrochemistry, including some treatments of electrode kinetics, was written by several Lewis group researchers.[189]

B.2.1 Theoretical Considerations

A semiconductor photodiode operates on the basis of the formation of a rectifying barrier that inhibits charge transfer across the interface between a semiconductor material and another medium with which it has been brought into electrochemical equilibrium. This barrier forms as a result of differences in Fermi level, or electrochemical potential, of the two contacting phases and results in transient charge transfer and formation of a static electric field in the space-charge region of the semiconductor. If the orientation of the electric field is such that the majority carriers are repelled from the interface, the semiconductor is said to be depleted. Figure 2.1 on page 25 contains a band diagram depicting a semiconductor-electrolyte interface in the depleted state.

When a semiconductor in depletion is illuminated with photons of energy greater than E_g, excited electrons and holes are generated. As a result of the space-charge region, these charge carriers experience a net force causing minority carriers to move toward the interface and majority carriers move toward the semiconductor bulk. As a result, the steady state electrochemical potential of electrons and holes in the near-surface region of an illuminated semiconductor are not equivalent. This difference in electrochemical potential manifests as a difference in electrical potential at the front and back surfaces of the semiconductor, and this voltage difference can be used to drive current through a load for net conversion of solar energy to electrical energy. Alternatively, this photovoltage can be used to drive net chemistry at the semiconductor surface and at a counter electrode connected to the back contact. This mode of operation converts solar energy to chemical energy through electronic

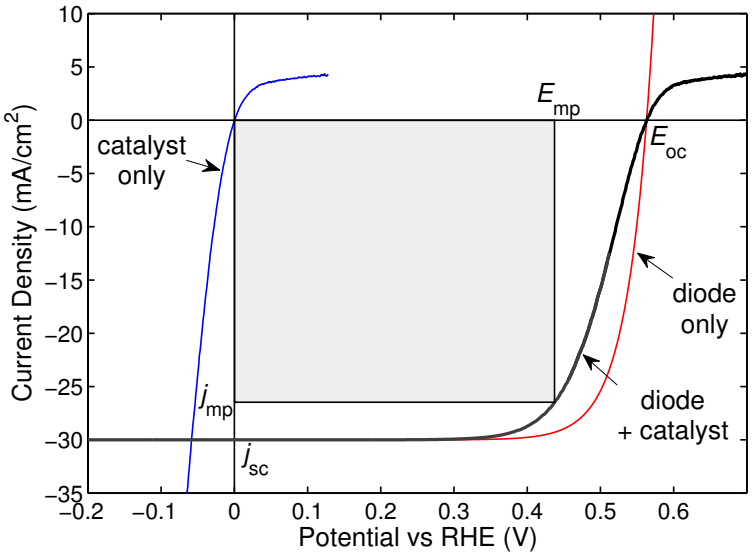

Figure B.3. Model of a high performing Si/Pt hydrogen evolving photocathode under 100 mW cm^{-2} solar illumination based on a serial combination of the Schockley diode equation for the light absorber and empirical j–E data for a Pt catalyst, which are both shown for reference. Several key energy parameters have been labeled. The η for this modeled photocathode is ∼12%.

excited states, and so it is called photoelectrochemistry.

The current-voltage properties of an illuminated diode are described by the Schockley diode equation modified by a constant factor, j_{ph}, the photocurrent density:

$$j = j_0 \left(e^{\frac{qE}{kT}} - 1 \right) - j_{\mathrm{ph}} \tag{B.10}$$

where q is the unsigned electronic charge and q/kT is ∼26 meV at room temperature. The value of j_{ph} is related to the incoming light flux and the proportion of absorbed photons leading to productive collection of excited-state charge carriers. The proportion of incident or absorbed photons that manifests as j_{ph} are called the external and internal quantum yield, Φ_{ext} and Φ_{int}, respectively. An ideal diode that drives net cathodic current from the semiconductor to the contacting phase (a photocathode) exhibits a rounded rectangular current-voltage profile in the fourth quadrant, as shown in Figure B.3.

For a PEC cell the electrochemical potentials E_{oc} and E_{mp} can be converted

to their respective voltages V_{oc} and V_{mp} by substracting them from the $E^{0'}$ of the electrolyte (e.g., E_{RHE} for hydrogen evolution) . In addition to these, two other parameters for evaluating the energy conversion behavior of a photocathode are the short-circuit current density (j_{sc}), the current density at maximum power (j_{mp}), which are also labeled in Figure B.3. From these parameters we can calculate the maximum energy conversion efficiency (η, Equation B.11), where P_{in} is the incident energy is the incident power flux (e.g., in mW cm^{-2}) and ff is the fill factor (Equation B.12).

$$\eta = \frac{V_{mp} \cdot j_{mp}}{P_{in}} \tag{B.11}$$

$$ff = \frac{V_{mp} \cdot j_{mp}}{V_{oc} \cdot j_{sc}} \tag{B.12}$$

It is important to note that the same key metrics apply for any photovoltaic device, regardless of the identity of the contacting phase or the process is driven by charge transfer. In the solid state, potentials are applied and measured between the front and back contacts of the diode. For photoelectrochemistry, it is convenient to carry out three-electrode measurements where potentials are measured and applied between the semiconductor back contact and the (arbitrary) reference electrode potential. The value of $E^{0'}$, however, can be defined relative to the reference electrode potential, so the applied voltage can be converted to a potential vs. $E^{0'}$. This way the energy-conversion efficiency of an individual photoelectrode carrying out an individual electrochemical half reaction can be determined on a thermodynamic basis. The resulting data are directly analogous to two-electrode solid state measurements, albeit convoluted with electrochemical factors such as solution resistance. Efficiencies calculated from such data are called themodynamically-based energy conversion efficiencies.

For driving PEC hydrogen evolution, it is extremely unlikely to observe j–E data closely resembling the ideal diode equation. This is because various aspects of the physical and electrochemical properties of the catalyst will act to attenuate both the photocurrent and photovoltage of a composite photocathode. First, and perhaps

most importantly, some portion of the photovoltage must be "spent" to overcome the inherent kinetic limitations of the HER. This results in a degradation of the photocathode fill factor and, in some cases, the short-circuit photocurrent. Second, light absorption/reflection by the catalyst layer decreases absorption in the semiconductor, resulting in decreased Φ_{ext}. Finally, various aspects of the mixed interface between semiconductor and catalyst vs. semiconductor and electrolyte can perturb the photovoltage. In principle, these mixed-contact interfaces can result in larger or smaller photovoltages, but in most cases for PEC hydrogen evolution, deposition of catalysts degrades the photovoltage somewhat.

The observed behavior of a HER photoelectrode can be attributed to a convoluion of the individual properties of the semiconductor-electrolyte and catalyst-electrolyte interfaces, as well as some aspects related to emergent interactions between the semiconductor, catalyst, and electrolyte. The goal of photoelectrode characterization is to discern what factors are primarily reponsible for energy conversion efficiencies lower than the maximum expected for a given semiconductor/redox couple pair.

B.2.2 Experimental Considerations

In order to obtain data for HER composite photocathodes (absorbers plus catalysts) that can be rationally interpreted, it is very important to independently establish the pure catalytic properties of the associated electrocatalyst and the pure solar energy conversion properties of the light absorber. For characterization of the electrocatalyst alone, the approach outlined in Section B.1 can be followed. Such experiments would preferably make use of substrates that match the surface and stability properties of the photoelectrode material of interest. For example, degenerately doped Si samples can be used to study the pure catalytic properties of associated HER electrocatalysts while also mimicking very closely the surface and stability behavior of Si photoelectrodes.

For independent characterization of the energy conversion properties of the photoelectrode material, PEC experiments with 1-electron redox couples should be used. For example, for p-type Si electrodes, the methyl viologen ($MV^{2+/+}$) aqueous redox

couple may be used. Detailed description of those experimental procedures can be found in recent Lewis group publications.[44,45]

Experimental procedures for testing composite photocathodes are very similar to those used for dark electrocatalysis experiments. Considerations regarding the identity and placement of the counter and reference electrodes, as well as the electrolyte purity and composition, are essentially the same. However, for photoelectrochemistry experiments the experimental apparatus must also accomodate illumination of the photoelectrode surfaces. The cell should incorporate an optically transparent, flat borosilicate or quartz glass window on the side or bottom. The light source used for illumination should be independently characterized with respect to its spectrum, and then a calibrated photodiode can be used inside the cell to set the incoming light flux at the position of the working electrode to the desired level. We have found that ELH-type tungsten halogen bulbs, such as those used in overhead projects or fiber optic light sources, match the AM1.5G solar spectrum very well when using Si or other materials with similar bandgaps.

The photoelectrode must be oriented toward the incoming illumination, which generally means that it will face away from the counter and reference electrodes. As a result the uncompensated resistance between the working and reference electrodes might be somewhat larger during such experiments. However, current-interrupt compensation must not be used with semiconductor photoelectrodes, as it relies on analysis of capacitive discharge processes at the working electrode that are modified by the presence of a depletion region. If uncompensated resistance must be accounted for, it is better to construct a secondary conductive electrode that closely matches the dimensions of the photoelectrode and use it to characterize the relevant resistance under the same conditions. Then the resistive component of the current-voltage behavior of the photoelectrode can be removed after the experiments are complete.

Effective solution agitation is also particularly important for measurements of composite HER photoelectrode properties. Since the HER gives a gaseous product at room temperature, even relatively small current densities (>5 mA cm^{-2} or so) will result in formation of bubbles, which can decrease the active surface area for

electrocatalysis as well as interfere with incoming light intensity. The problem is exacerbated by the fact that any agitation method (usually a stir bar) must not block or otherwise interfere with the incoming light flux. Rotating disk electrodes using semiconductor materials are not commercially available, but can be constructed in the laboratory in order to give optimum mass transport behavior and effectively sweep away bubbles.

Another significant consideration for studying composite HER photocathode behavior is defining appropriate scan limits. A j–E scan should extend from at least several hundred mV negative of E_{RHE} to a potential sufficiently positive to see a small amount of anodic current flow from the photocathode. Often some trial and error is required in order to define these optimal scan parameters. The E_{RHE} vs. the reference electrode can be estimated or measured prior to experimentation, and it should also be verified to a high degree of accuracy using the method outlined in Section B.1.2 after measurements are complete. Some semiconductor and catalyst materials (such as Si and Ni, respectively) are particularly sensitive to passing anodic current, and will rapidly degrade under these conditions. It is important with these materials to ensure that the scan limits are controlled so as to clearly observe E_{oc} but not to scan significantly positive of this potential.

Current-voltage behavior for composite HER photoelectrodes can be converted so that the potential is relative to E_{RHE} and then interpreted as with conventional photoelectrodes in terms of the key figures of merit, even across different pH values. The observed behavior can be analyzed in comparison to the known properties of the absorber material and the electrocatalyst. Thus factors that limit the energy conversion efficiency can be attributed to either the semiconductor, the electrocatalyst, or to some emergent behavior resulting from interfacing the two.

Long-term testing of composite HER photocathodes can be challenging due to the difficulty in collecting data with sufficient information to understand both the rate and the nature of photoelectrode degradation. For example, constant potential experiments might be started at E_{mp} or E_{oc} but after degradation may be closer to E_{oc}. Similarly, constant current measurements can result in badly damaged semiconductor

samples if j_{ph} degrades to below the current demanded from the galvanostat circuit. Considering these potential deficiencies, the most straightforward long-term testing method for HER composite photocathodes is an "accelerated degradation" method, as described in Section B.1.2. This method allows for characterization of the full j–E properties of a photocathode over long times.

Another, perhaps better method for testing the long-term stability behavior of photoelectrodes would involve dynamic iteration between constant potential and potential sweep methods. First a full j–E curve is measured, and the potential at the maximum power point is determined. Then the photoelectrode is poised at the E_{mp} for a set interval, after which the process is simply repeated for a desired number of cycles. This method allows for testing the photoelectrode under conditions more closely resembling the desired operating conditions, and also allows for semi-continuous measurement of the full j–E behavior in order to help discern the nature of the degradation process (e.g., primarily loss of photovoltage, photocurrent, and/or fill factor). The method can be carried out manually or using programmable software that is commonly provided with digital potentiostat instruments.

Bibliography

[1] U.S. Energy Information Administration, 2012 Annual Energy Review. 2012; Available online: http://www.eia.gov/totalenergy/data/annual.

[2] Lawrence Livermore National Laboratory, Energy Flow Diagrams. 2011; Available online: https://flowcharts.llnl.gov.

[3] Lewis, N. S. Powering the Planet. Presentation. Available online: http://nsl.caltech.edu/energy.

[4] Lewis, N. S. *MRS Bull.* **2007**, *32*, 808.

[5] Höök, M.; Tang, X. *Energy Policy* **2013**, *52*, 797.

[6] Berkeley Earth Surface Temperature, Summary of Results. Available online: http://berkeleyearth.org/results-summary.

[7] Barbose, G.; Darghouth, N.; Wiser, R. *Tracking the Sun V: An Historical Summary of the Installed Price of Photovoltaics in the United States from 1998 to 2011*; 2012; pp 1–61, Available online: http://emp.lbl.gov/sites/all/files/lbnl-5919e.pdf.

[8] U.S. Department of Energy Advanced Research Projects Agency-Energy, $1/W Photovoltaic Systems: White Paper to Explore a Grand Challenge for Electricity from Solar. 2010; Available online: http://www1.eere.energy.gov/solar/sunshot/pdfs/dpw_white_paper.pdf.

[9] Green, M. A.; Emery, K.; Hishikawa, Y.; Warta, W.; Dunlop, E. D. *Prog. Photovolt.: Res. Appl.* **2013**, *21*, 1.

[10] Kayes, B. M.; Nie, H.; Twist, R.; Spruytte, S. G.; Reinhardt, F.; Kizilyalli, I. C.; Higashi, G. S. 27.6 % Conversion efficiency, a new record for single-junction solar cells under 1 sun illumination. 37th IEEE PVSC. 2011; pp 4–8.

[11] National Renewable Energy Laboratory, NREL Solar Maps. Available online: http://www.nrel.gov/gis/solar.html.

[12] Solomon, A.; Faiman, D.; Meron, G. *Energy Policy* **2010**, *38*, 5469.

[13] Solomon, A.; Faiman, D.; Meron, G. *Energy Policy* **2010**, *38*, 5208.

[14] Solomon, A.; Faiman, D.; Meron, G. *Energy Policy* **2010**, *38*, 5457.

[15] Ibrahim, H.; Ilinca, A.; Perron, J. *Renewable Sustainable Energy Rev.* **2008**, *12*, 1221.

[16] Solomon, A.; Faiman, D.; Meron, G. *Energy Policy* **2012**, *40*, 335.

[17] Wadia, C.; Albertus, P.; Srinivasan, V. *J. Power Sources* **2011**, *196*, 1593.

[18] Kainthla, R. C.; Zelenay, B.; Bockris, J. O. M. *J. Electrochem. Soc.* **1985**, *134*, 841.

[19] Khaselev, O.; Turner, J. A. *Science* **1998**, *280*, 425.

[20] Licht, S.; Wang, B.; Mukerji, S.; Soga, T.; Umeno, M.; Tributsch, H. *J. Phys. Chem. B* **2000**, *104*, 8920.

[21] Khaselev, O.; Bansal, A.; Turner, J. A. *Int. J. Hydrogen Energy* **2001**, *26*, 127.

[22] Rocheleau, R. E.; Miller, E. L.; Misra, A. *Energy Fuels* **1998**, *12*, 3.

[23] Reece, S. Y.; Hamel, J. A.; Sung, K.; Jarvi, T. D.; Esswein, A. J.; Pijpers, J. J. H.; Nocera, D. G. *Science* **2011**, *334*, 645.

[24] Levy-Clement, C.; Heller, A.; Bonner, W. A.; Parkinson, B. A. *J. Electrochem. Soc.* **1982**, *129*, 1701.

[25] Luttmer, J.; Trachtenberg, I. *J. Electrochem. Soc.* **1985**, *132*, 1312.

[26] Gray, H. B. *Nat. Chem.* **2009**, *1*, 7.

[27] Santori, E. Si Microwire Array Photoanodes for Artificial Photosynthetic Devices. Ph.D. thesis, California Institute of Technology, 2013.

[28] Kanan, M. W.; Nocera, D. G. *Science* **2008**, *321*, 1072.

[29] Stubbert, B. D.; Peters, J. C.; Gray, H. B. *J. Am. Chem. Soc.* **2011**, *133*, 18070.

[30] Dempsey, J. L.; Brunschwig, B. S.; Winkler, J. R.; Gray, H. B. *Acc. Chem. Res.* **2009**, *42*, 1995.

[31] Chao, T.-H.; Espenson, J. *J. Am. Chem. Soc.* **1978**, *100*, 129.

[32] Hu, X.; Brunschwig, B. S.; Peters, J. C. *J. Am. Chem. Soc.* **2007**, *129*, 8988.

[33] O'Leary, L. E.; Johansson, E.; Brunschwig, B. S.; Lewis, N. S. *J. Phys. Chem. B* **2010**, *114*, 14298.

[34] Dempsey, J. L.; Winkler, J. R.; Gray, H. B. *J. Am. Chem. Soc.* **2010**, *132*, 16774.

[35] Maiolo, J. R.; Kayes, B. M.; Filler, M. A.; Putnam, M. C.; Kelzenberg, M. D.; Atwater, H. A.; Lewis, N. S. *J. Am. Chem. Soc.* **2007**, *129*, 12346.

[36] Kayes, B. M.; Filler, M. A.; Putnam, M. C.; Kelzenberg, M. D.; Lewis, N. S.; Atwater, H. A. *Appl. Phys. Lett.* **2007**, *91*, 103110.

[37] Maiolo, J.; Atwater, H.; Lewis, N. *J. Phys. Chem. C* **2008**, *112*, 6194.

[38] Kelzenberg, M. D.; Turner-Evans, D. B.; Kayes, B. M.; Filler, M. A.; Putnam, M. C.; Lewis, N. S.; Atwater, H. A. *Nano Lett.* **2008**, *8*, 710.

[39] Putnam, M. C.; Turner-Evans, D. B.; Kelzenberg, M. D.; Boettcher, S. W.; Lewis, N. S.; Atwater, H. A. *Appl. Phys. Lett.* **2009**, *95*, 163116–1.

[40] Plass, K. E.; Filler, M. A.; Spurgeon, J. M.; Kayes, B. M.; Maldonado, S.; Brunschwig, B. S.; Atwater, H. A.; Lewis, N. S. *Adv. Mater.* **2009**, *21*, 325.

[41] Spurgeon, J. M.; Boettcher, S. W.; Kelzenberg, M. D.; Brunschwig, B. S.; Atwater, H. A.; Lewis, N. S. *Adv. Mater.* **2010**, *91125*, 3277.

[42] Putnam, M. C.; Boettcher, S. W.; Kelzenberg, M. D.; Turner-Evans, D. B.; Spurgeon, J. M.; Warren, E. L.; Briggs, R. M.; Lewis, N. S.; Atwater, H. A. *Energy Environ. Sci.* **2010**, *3*, 1037.

[43] Kelzenberg, M. D.; Boettcher, S. W.; Petykiewicz, J. A.; Turner-Evans, D. B.; Putnam, M. C.; Warren, E. L.; Spurgeon, J. M.; Briggs, R. M.; Lewis, N. S.; Atwater, H. A. *Nat. Mater.* **2010**, *9*, 239.

[44] Boettcher, S. W.; Spurgeon, J. M.; Putnam, M. C.; Warren, E. L.; Turner-Evans, D. B.; Kelzenberg, M. D.; Maiolo, J. R.; Atwater, H. A.; Lewis, N. S. *Science* **2010**, *327*, 185.

[45] Warren, E.; Boettcher, S.; Walter, M.; Atwater, H. A.; Lewis, N. S. *J. Phys. Chem. C* **2011**, *115*, 594.

[46] Boettcher, S. W.; Warren, E. L.; Putnam, M. C.; Santori, E. L.; Turner-Evans, D.; Kelzenberg, M. D.; Walter, M. G.; McKone, J. R.; Brunschwig, B. S.; Atwater, H. A.; Lewis, N. S. *J. Am. Chem. Soc.* **2011**, *133*, 1216.

[47] Keita, B.; Nadjo, L. *J. Electroanal. Chem.* **1985**, *191*, 441.

[48] Walter, M.; Warren, E.; McKone, J.; Boettcher, S.; Qixi, M.; Santori, L.; Lewis, N. *Chem. Rev.* **2010**, *110*, 6446.

[49] McKone, J. R.; Warren, E. L.; Bierman, M. J.; Boettcher, S. W.; Brunschwig, B. S.; Lewis, N. S.; Gray, H. B. *Energy Environ. Sci.* **2011**, *4*, 3573.

[50] Warren, E. L.; McKone, J. R.; Atwater, H. A.; Gray, H. B.; Lewis, N. S. *Energy Environ. Sci.* **2012**, *5*, 9653.

[51] McKone, J.; Sadtler, B.; Werlang, C.; Lewis, N.; Gray, H. *ACS Catal.* **2013**, *3*, 166.

[52] Popczun, E.; McKone, J.; Read, C.; Biacchi, A.; Wiltrout, A. M.; Lewis, N.; Schaak, R. *Submitted for publication.*

[53] McKone, J.; Pieterick, A.; Gray, H.; Lewis, N. *J. Am. Chem. Soc.* **2013**, *135*, 223.

[54] Trasatti, S. *J. Electroanal. Chem.* **1972**, *39*, 163.

[55] Miles, M. *J. Electroanal. Chem.* **1975**, *60*, 89.

[56] Laursen, A.; Varela, A. *J. Chem. Educ.* **2012**, *89*, 1595.

[57] Gerischer, H., *Bull. Soc. Chim. Belg.* **1958**, *67*, 506.

[58] Parsons, R. *Trans. Faraday Soc.* **1958**, *54*, 1053.

[59] Nørskov, J. K.; Bligaard, T.; Logadottir, A.; Kitchin, J. R.; Chen, J. G.; Pandelov, S.; Stimming, U. *J. Electrochem. Soc.* **2005**, *152*, J23.

[60] Greeley, J.; Nørskov, J.; Kibler, L.; El-Aziz, A.; Kolb, D. *ChemPhysChem* **2006**, *7*, 1032.

[61] Kibler, L. *ChemPhysChem* **2006**, *7*, 985.

[62] Hinnemann, B.; Moses, P.; Bonde, J.; Jorgensen, K.; Nielsen, J.; Horch, S.; Chorkendorff, I.; Nørskov, J. *J. Am. Chem. Soc.* **2005**, *127*, 5308.

[63] Greeley, J.; Jaramillo, T. F.; Bonde, J.; Chorkendorff, I.; Nørskov, J. K. *Nat. Mater.* **2006**, *5*, 909.

[64] Jaramillo, T. F.; Jorgensen, K. P.; Bonde, J.; Nielsen, J. H.; Horch, S.; Chorkendorff, I. *Science* **2007**, *317*, 100.

[65] Trasatti, S. In *Advances in Electrochemical Science and Engineering*; Gerischer, H., Tobias, C., Eds.; VCH: Weinheim, Germany, 1992; Vol. 2; Chapter 1, pp 1–85.

[66] Brown, D.; Mahmood, M.; Turner, A.; Hall, S.; Fogarty, P. *Int. J. Hydrogen Energy* **1982**, *7*, 405.

[67] Brown, D.; Mahmood, M. Method of preparing active electrodes. 1982; U.S. Patent 4,358,475.

[68] Brown, D.; Mahmood, M.; Man, M.; Turner, A. *Electrochim. Acta* **1984**, *29*, 1551.

[69] Stachurski, J.; Pouli, D.; Ripa, J.; Pokrzyk, G. Low overvoltage hydrogen cathodes. 1982; U.S. Patent 4,354,915.

[70] Conway, B.; Angersteinkozlowska, H.; Sattar, M.; Tilak, B. *J. Electrochem. Soc.* **1983**, *130*, 1825.

[71] Conway, B.; Bai, L. *J. Chem. Soc., Faraday Trans. I* **1985**, *81*, 1841.

[72] Conway, B.; Bai, L. *Int. J. Hydrogen Energy* **1986**, *11*, 533.

[73] Raj, I.; Venkatesan, V. *Int. J. Hydrogen Energy* **1988**, *13*, 215.

[74] Raj, I.; Vasu, K. *J. Appl. Electrochem.* **1990**, *20*, 32.

[75] Raj, I. *Int. J. Hydrogen Energy* **1992**, *17*, 413.

[76] Raj, I.; Vasu, K. *J. Appl. Electrochem.* **1992**, *22*, 471.

[77] Raj, I. *J. Mater. Sci.* **1993**, *28*, 4375.

[78] Raj, I. *Bull. Electrochem.* **1999**, *15*, 519.

[79] Fan, C.; Piron, D.; Sleb, A.; Paradis, P. *J. Electrochem. Soc.* **1994**, *141*, 382.

[80] Hu, W.; Zhang, Y.; Song, D.; Zhou, Z.; Wang, Y. *Mater. Chem. Phys.* **1995**, *41*, 141.

[81] Kawashima, A.; Akiyama, E.; Habazaki, H.; Hashimoto, K. *Mat. Sci. Eng. A* **1997**, *226*, 905.

[82] de Chialvo, M.; Chialvo, A. *J. Electroanal. Chem.* **1998**, *448*, 87.

[83] Highfield, J. G.; Claude, E.; Oguro, K. *Electrochim. Acta* **1999**, *44*, 2805.

[84] Hu, C.; Weng, C. *J. Appl. Electrochem.* **2000**, *30*, 499.

[85] Jaksic, J.; Vojnovic, M.; Krstajic, N. *Electrochim. Acta* **2000**, *45*, 4151.

[86] Jayalakshmi, M.; Kim, W.; Jung, K.; Joo, O. *Int. J. Electrochem. Sci.* **2008**, *3*, 908.

[87] Krstajic, N.; Jovic, V.; Gajic-Krstajic, L.; Jovic, B.; Antozzi, A.; Martelli, G. *Int. J. Hydrogen Energy* **2008**, *33*, 3676.

[88] Ernst, D. W.; Holt, M. L. *J. Electrochem. Soc.* **1958**, *105*, 686.

[89] Hovey, N. W.; Krohn, A.; Hanneken, J. *J. Electrochem. Soc.* **1963**, *110*, 362.

[90] Chassaing, E.; Quang, K.; Wiart, R. *J. Appl. Electrochem.* **1989**, *19*, 839.

[91] Müller, A.; Serain, C. *Acc. Chem. Res.* **2000**, *33*, 2.

[92] Tsuru, Y.; Nomura, M.; Foulkes, F. *J. Appl. Electrochem.* **2002**, *32*, 629.

[93] Spurgeon, J.; Atwater, H.; Lewis, N. *J. Phys. Chem. C* **2008**, *112*, 6186.

[94] Levin, D.; Soled, S. L.; Ying, J. Y. *Inorg. Chem.* **1996**, *35*, 4191.

[95] Schmitt, P.; Brem, N.; Schunk, S.; Feldmann, C. *Adv. Funct. Mater.* **2011**, *21*, 3037.

[96] Bard, A. J.; Faulkner, L. R. *Electrochemical Methods: Fundamentals and Applications*, 2nd ed.; Wiley, 2000.

[97] Saji, V. S.; Lee, C.-W. *J. Electrochem. Soc.* **2013**, *160*, H54.

[98] Farsi, H.; Gobal, F.; Raissi, H.; Moghiminia, S. *J. Solid State. Electrochem.* **2009**, *14*, 643.

[99] Conway, B.; Tilak, B. *Electrochim. Acta* **2002**, *47*, 3571.

[100] Sines, I. T.; Schaak, R. E. *J. Am. Chem. Soc.* **2011**, *133*, 1294.

[101] Nørskov, J. K.; Scheffler, M.; Toulhoat, H. *MRS Bull.* **2006**, *31*, 669.

[102] Laursen, A. B.; Kegnæs, S.; Dahl, S.; Chorkendorff, I. *Energy Environ. Sci.* **2012**, *5*, 5577.

[103] Merki, D.; Hu, X. *Energy Environ. Sci.* **2011**, *4*, 3878.

[104] Merki, D.; Vrubel, H.; Rovelli, L.; Fierro, S.; Hu, X. *Chem. Sci.* **2012**, *3*, 2515.

[105] Kibsgaard, J.; Chen, Z.; Reinecke, B. N.; Jaramillo, T. F. *Nat. Mater.* **2012**, *11*, 1.

[106] Liu, P.; Rodriguez, J. A.; Asakura, T.; Gomes, J.; Nakamura, K. *J. Phys. Chem. B* **2005**, *109*, 4575.

[107] Prins, R.; Bussell, M. E. *Catalysis Lett.* **2012**, *142*, 1413.

[108] Paseka, I. *Electrochim. Acta* **1995**, *40*, 1633.

[109] Burchardt, T. *Int. J. Hydrogen Energy* **2001**, *26*, 1193.

[110] Liu, P.; Rodriguez, J. A. *J. Am. Chem. Soc.* **2005**, *127*, 14871.

[111] Wang, J.; Johnston-Peck, A. C.; Tracy, J. B. *Chem. Mater.* **2009**, *21*, 4462.

[112] Muthuswamy, E.; Savithra, G. H. L.; Brock, S. L. *ACS Nano* **2011**, *5*, 2402.

[113] Chen, Z.; Cummins, D.; Reinecke, B.; Clark, E.; Mahendra, S.; Jaramillo, T. F. *Nano Lett.* **2011**, *11*, 4168.

[114] Chen, W.-F.; Sasaki, K.; Ma, C.; Frenkel, A. I.; Marinkovic, N.; Muckerman, J. T.; Zhu, Y.; Adzic, R. R. *Angew. Chem., Int. Ed.* **2012**, *51*, 6131.

[115] Wagner, R. S.; Ellis, W. C. *Appl. Phys. Lett.* **1964**, *4*, 89.

[116] Warren, E. Silicon microwire arrays for photoelectrochemical and photovoltaic applications. Ph.D. thesis, California Institute of Technology, 2013.

[117] Baglio, J.; Calabrese, G.; Harrison, D.; Kamieniecki, E.; Ricco, A.; Wrighton, M.; Zoski, G. *J. Am. Chem. Soc.* **1983**, *105*, 2246.

[118] Bookbinder, D. C.; Lewis, N. S.; Bradley, M. G.; Bocarsly, A. B.; Wrighton, M. S. *J. Am. Chem. Soc.* **1979**, *101*, 7721.

[119] Dominey, R. N.; Lewis, N. S.; Bruce, J. A.; Bookbinder, D. C.; Wrighton, M. S. *J. Am. Chem. Soc.* **1982**, *104*, 467.

[120] Luttmer, J. D. *J. Electrochem. Soc.* **1985**, *132*, 1054.

[121] Seger, B.; Laursen, A. B.; Vesborg, P. C. K.; Pedersen, T.; Hansen, O.; Dahl, S.; Chorkendorff, I. *Angew. Chem., Int. Ed.* **2012**, *51*, 9128.

[122] Heller, A.; Vadimsky, R. G. *Phys. Rev. Lett.* **1981**, *46*, 1153.

[123] Heller, A.; Aharon-Shalom, E.; Bonner, W. A.; Miller, B. *J. Am. Chem. Soc.* **1982**, *104*, 6942.

[124] Heller, A.; Aspnes, D. E.; Porter, J. D.; Sheng, T. T.; Vadimsky, R. G. *J. Phys. Chem.* **1985**, *89*, 4444.

[125] Heller, A. *Pure Appl. Chem.* **1986**, *58*, 1189.

[126] Degani, Y.; Sheng, T.; Heller, A.; Aspnes, D. *J. Electroanal. Chem.* **1987**, *228*, 167.

[127] Lombardi, I.; Marchionna, S.; Zangari, G.; Pizzini, S. *Langmuir* **2007**, *23*, 12413.

[128] Fahrenbruch, A.; Bube, R. *Fundamentals of Solar Cells*; Academic Press, 1983.

[129] Trotochaud, L.; Mills, T. J.; Boettcher, S. W. *J. Phys. Chem. Lett.* **2013**, *4*, 931.

[130] Kautek, W.; Gobrecht, J.; Gerischer, H. *Ber. Bunsenges. Phys. Chem.* **1980**, *84*, 1034.

[131] Aruchamy, A. *Photoelectrochemistry and Photovoltaics of Layered Semiconductors*, 1st ed.; Springer, 1992.

[132] Tenderholt, A. L.; Szilagyi, R. K.; Holm, R. H.; Hodgson, K. O.; Hedman, B.; Solomon, E. I. *Inorg. Chem.* **2008**, *47*, 6382.

[133] Eisenberg, R.; Gray, H. B. *Inorg. Chem.* **2011**, *50*, 9741.

[134] Eisenberg, R. *Coord. Chem. Rev.* **2011**, *255*, 825.

[135] Wilson, J.; Yoffe, A. *Adv. Phys.* **1969**, *18*, 193.

[136] Mattheiss, L. *Phys. Rev. B.* **1973**, *8*, 3719.

[137] Srivastava, S.; Avasthi, B. *J. Mater. Sci.* **1985**, *20*, 3801.

[138] Tributsch, H.; Bennett, J. *J. Electroanal. Chem.* **1977**, *81*, 97.

[139] Prasad, G.; Srivastava, O. *J. Phys. D: Appl. Phys.* **1988**, *21*, 1028.

[140] Kline, G.; Kam, K.; Ziegler, R.; Parkinson, B. *Sol. Energy Mater.* **1982**, *6*, 337.

[141] Kline, G.; Kam, K.; Canfield, D.; Parkinson, B. *Sol. Energy Mater.* **1981**, *4*, 301.

[142] Tenne, R.; Wold, A. *Appl. Phys. Lett.* **1985**, *47*, 707.

[143] Lewerenz, H. J.; Heller, A.; Disalvo, F. J. *J. Am. Chem. Soc.* **1980**, *102*, 1877.

[144] Lewerenz, H.; Gerischer, H.; Lubke, M. *J. Electrochem. Soc.* **1984**, 100.

[145] Cabrera, C.; Abruña, H. *J. Electrochem. Soc.* **1988**, *135*, 1436.

[146] Vogt, M.; Lux-Steiner, M.; Dolatzoglou, P.; Reetz, W.; Bumüller, B.; Bucher, E. *Proc. IEEE, PVSC 21* **1990**, *1*, 519.

[147] Chopra, K. L.; Paulson, P. D.; Dutta, V. *Prog. Photovolt.: Res. Appl.* **2004**, *12*, 69.

[148] Romeo, A.; Terheggen, M.; Abou-Ras, D.; Bätzner, D. L.; Haug, F.-J.; Kälin, M.; Rudmann, D.; Tiwari, A. N. *Prog. Photovolt.: Res. Appl.* **2004**, *12*, 93.

[149] Binnewies, M.; Glaum, R.; Schmidt, M.; Schmidt, P. *Chemical Vapor Transport Reactions*; Walter de Gruyter: Munich, 2012.

[150] Kershaw, R.; Vlasse, M.; Wold, A. *Inorg. Chem.* **1967**, *6*, 1599.

[151] Parkinson, B. A.; Furtak, T. E.; Canfield, D.; Kam, K.-K.; Kline, G. *Faraday Discuss. Chem. Soc.* **1980**, *70*, 233.

[152] Baglio, J.; Kamieniecki, E.; Decola, N.; Struck, C.; Marzik, J.; Dwight, K.; Wold, A. *J. Solid State Chem.* **1983**, *49*, 166.

[153] Douay, V.; Gorochov, O. *J. Chim. Phys.* **1986**, *83*, 247.

[154] Koval, C. A.; Olson, J. B. *J. Electroanal. Chem.* **1987**, *234*, 133.

[155] Legma, J.; Vacquier, G.; Casalot, A. *J. Cryst. Growth* **1993**, *130*, 253.

[156] Mahalu, D.; Jakubowicz, A.; Wold, A.; Tenne, R. *Phys. Rev. B* **1988**, *38*, 1533.

[157] Jakubowicz, A.; Mahalu, D.; Wolf, M.; Wold, A.; Tenne, R. *Phys. Rev. B* **1989**, *40*, 2992.

[158] Bonde, J.; Moses, P. G.; Jaramillo, T. F.; Nørskov, J. K.; Chorkendorff, I. *Faraday Discuss.* **2008**, *140*, 219.

[159] Li, Y.; Wang, H.; Xie, L.; Liang, Y.; Hong, G.; Dai, H. *J. Am. Chem. Soc.* **2011**, *133*, 7296.

[160] Kong, D.; Wang, H.; Cha, J.; Pasta, M.; Koski, K.; Yao, J.; Cui, Y. *Nano Lett.* **2013**, *13*, 1341.

[161] Penner, R. M. *J. Phys. Chem. B* **2002**, *106*, 3339.

[162] Johansson, E.; Boettcher, S. W.; O'Leary, L. E.; Poletayev, A. D.; Maldonado, S.; Brunschwig, B. S.; Lewis, N. S. *J. Phys. Chem. C* **2011**, *115*, 8594.

[163] Sourisseau, C.; Cruege, F.; Gorochov, O. *J. Electroanal. Chem.* **1991**, *308*, 239.

[164] Kam, K. K.; Parkinson, B. A. *J. Phys. Chem.* **1982**, *86*, 463.

[165] Lyon, L. A.; Hupp, J. T. *J. Phys. Chem. B* **1999**, *103*, 4623.

[166] Royea, W. J.; Michalak, D. J.; Lewis, N. S. *Appl. Phys. Lett.* **2000**, *77*, 2566.

[167] Michalak, D. J.; Lewis, N. S. *Appl. Phys. Lett.* **2002**, *80*, 4458.

[168] Gstrein, F.; Michalak, D. J.; Royea, W. J.; Lewis, N. S. *J. Phys. Chem. B* **2002**, *106*, 2950.

[169] Aharon-Shalom, E.; Heller, A. *J. Electrochem. Soc.* **1982**, *129*, 2865.

[170] Scheel, H. *J. Cryst. Growth* **1974**, *24/25*, 669.

[171] Ellmer, K. *Phys. Stat. Sol. B* **2008**, *245*, 1745.

[172] Brunken, S.; Mientus, R.; Seeger, S.; Ellmer, K. *J. Appl. Phys.* **2008**, *103*, 063501.

[173] National Renewable Energy Laboratory, Hompage: NREL National Center for Photovoltaics. http://www.nrel.gov/ncpv.

[174] Sawyer, D.; Sobkowiak, A.; Roberts, J. *Electrochemistry for Chemists*, 2nd ed.; Wiley: New York, 1995.

[175] Zoski, C. In *Handbook of Electrochemistry*, 1st ed.; Zoski, C., Ed.; Elsevier: Amsterdam, 2007.

[176] Tafel, J. *Z. Phys. Chem-Stoch. Ve.* **1905**, *50*, 641.

[177] Azzam, A. M.; Bockris, J. O.; Conway, B. E.; Rosenberg, H. *Trans. Faraday Soc.* **1950**, *46*, 918.

[178] Conway, B. *Electrochim. Acta* **1964**, *9*, 1599.

[179] Tafel, J.; Naumann, K. *Z. Phys. Chem-Stoch. Ve.* **1905**, *50*, 713.

[180] Myland, J. C.; Oldham, K. B. *Anal. Chem.* **2000**, *72*, 3972.

[181] Oldham, K. B.; Stevens, N. P. C. *Anal. Chem.* **2000**, *72*, 3981.

[182] Oelßner, W.; Berthold, F.; Guth, U. *Mater. Corros.* **2006**, *57*, 455.

[183] Newman, J. *J. Electrochem. Soc.* **1970**, *117*, 507.

[184] Boettcher, S. Personal Communication, February 2013.

[185] Wu, J.; Yuan, X. Z.; Martin, J. J.; Wang, H.; Zhang, J.; Shen, J.; Wu, S.; Merida, W. *J. Power Sources* **2008**, *184*, 104.

[186] Sze, S.; Ng, K. *Physics of Semiconductor Devices*, 3rd ed.; Wiley: Hoboken, NJ, 2007.

[187] Schroder, D. *Semiconductor Material and Device Characterization*, 3rd ed.; Wiley: Hoboken, NJ, 2006.

[188] Hoffmann, R. *Angew. Chem., Int. Ed.* **1987**, *26*, 846.

[189] Tan, M.; Laibinis, P.; Nguyen, S.; Kesselman, J.; Stanton, C.; Lewis, N. In *Prog. Inorg. Chem. 41*; Karlin, K. D., Ed.; Wiley: Hoboken, NJ, 1994; Chapter Principles, pp 21–144.